University of Southampton

Faculty of Engineering, Science and Mathematics

Optoelectronics Research Centre

Domain Engineering Techniques and Devices in Lithium Niobate

Collin Lawrence Sones

Submitted for the degree of Doctor of Philosophy

August 2003

University of Southampton

ABSTRACT

Faculty of Engineering and Applied Science

Optoelectronics Research Centre

Doctor of Philosophy

Domain engineering techniques and devices in lithium niobate

by Collin Lawrence Sones

This thesis presents the results from investigations directed at novel approaches to domain engineering single-crystal congruent lithium niobate at the micron/sub-micron scale for practical device applications.

Experimental etch-rate measurements from a parametric study of etch-rates and etch-quality of single-crystal lithium niobate z-faces, as a function of specific ratios for mixtures of HF/HNO_3, to ascertain whether the widely-employed 1:2 mixture was in fact optimum for achieving the largest differential etch-rates between lithium niobate z-faces, revealed that pure HF produced an etch-rate that is a factor of two higher than that for the more frequently used 1:2 mixture. The observed etch-quality as compared to the 1:2 ratio was also improved for either pure HF or HF/HNO_3 in a 1:4 ratio. A discussion of the etch-chemistry involved, and an explanation of the observed difference in etch-rates between the +z and –z faces has been proposed. The experimental results are also suggestive of a second differential etch-rate between virgin and newly poled z-faces.

The observed variation in the differential etch-rate as a function of time-delay following poling, was suggestive of small atomic displacements following poling, and was quantified by the evidenced shifts in six major Raman spectral peaks.

The noticeable modifications in the etch-behaviour of undoped congruent z-cut lithium niobate by pre-illumination with sub-picosecond UV-laser radiation of 248nm wavelength at energy fluences below the ablation threshold, demonstrates the potential applicability of this technique for μm-scale surface structuring of lithium niobate.

An innovative technique for surface domain-inversion, based on the conventional e-field poling, but involving an intentional over-poling step, was employed to fabricate 1D and 2D periodic structures with good domain uniformity. Domain periods as short as ~1μm have been achieved, and the technique shows full compatibility with standard waveguide fabrication techniques in lithium niobate. Quasi-phase matched harmonic generation at the fundamental wavelength of 1.064 μm, by means of the first-order (G_{10}) reciprocal lattice vector, from a surface hexagonally poled planar annealed proton exchanged waveguide, with domain period of 6.7μm, was demonstrated. First-order quasi-phase matched blue light generation with reasonable efficiencies at 413.17nm, with domain periods of 2.47μm from a surface poled Ti-indiffused channel waveguide was also demonstrated.

Finally an novel route, sequentially employing techniques such as photolithographic patterning, e-field poling, direct-bonding and domain-sensitive differential wet etching for the fabrication of freestanding piezoelectric micro-cantilevers in single-crystal lithium niobate, with MEMS/MOEMS end-applications, was demonstrated.

Contents

Chapter 5: Surface domain inversion and applications

Chapter 6: Domain engineering and MEMS/MOEMS application

Acknowledgements

I would like to thank Prof. Robert Eason for the abundant ideas, and the much needed encouragement and support that he has provided during the past three years.

I am thankful to Dr Sakellaris Mailis for passing on the much useful expertise and skills. I am also thankful to Alessandro Busacca for the great help during our collaborative work. A special thanks to my office-mates and fellow research students for their support.

I am also grateful to all my friends, who have been supportive all along my studies.

And finally I would like to thank my parents, my wife and my family for their prayers and good wishes

always giving thanks to God the father for everything, in the name of our Lord Jesus Christ.

Ephesians 5:20

Chapter 1
Introduction

1.1 Introduction

The first growth of lithium niobate (Ballman'65), followed by the first reports of successful single-domain growth of this synthetic ferroelectric crystal by the Czochralski technique (Nassau'66), resulted in the use of this material in realising signal processing chips for television and video cassette recorders. A great deal of advancement in the material quality since then and the development of mature optical waveguide fabrication techniques have also resulted in its use in integrated optical devices such as high speed optical modulators extensively employed in long distance dense wavelength division multiplexing telecommunications systems allowing increased transmission capacity and in commercial and military navigation systems using an optical signal processing chip. The characteristic technological attribute that allows its non-linear properties to be tailored by modifying the size, shape and periodicity of the ferroelectric domains has resulted in its use for applications such as optical dispersion compensation, optical wavelength conversion and optical parametric generation. The piezoelectric property of lithium niobate has made it quite significant for the growing mobile phone industry and its photorefractive property has further prompted its investigation for holographic image processing and data storage.

The popularity of this transparent man-made material thus results from the distinctive combination of the inherent physical properties like piezoelectricity, photorefractivity, non-linearity and the electro-optic effect.

The continuing technological advances towards miniaturisation for varied applications (such as bio-sensors and accelerometers for airbags) is a direct consequence of the massive downscaling in size of the silicon based integrated circuits observed in the microelectronics industry. Integrated circuit fabrication routes (with conventional fabrication techniques like photolithography, wet etching, thin film deposition, metallisation and ion-implantation) further extended by sculpting in the third spatial dimension with techniques like bulk/surface micromachining have provided the added potential for complex structuring.

Similarly engineering of the ferreoelectric domains and/or structuring lithium niobate at the micron or sub micron scale by either bulk or surface modifications could

provide an added functionality further broadening the extent of its applications to encompass the elusive domain of silicon microstructuring/MEMS. Exploring realistic techniques to structure lithium niobate at the micro/nano scale for a wide range of intriguing applications such as photonic crystals with controllable band gaps, highly efficient high power visible laser sources, digital information storage devices and micromachines is the motivation behind this research.

Attempts to microstructure lithium niobate have only been investigated to a limited extent so far with use of traditional processes employed on a regular basis within the microelectronics/semiconductor industry almost always resulting in planar/two-dimensional surface structures such as ridges, grooves/slots/depressions, relief patterns, gratings (Chen'97), and v-grooves (Ichikawa'98) for applications in integrated optics. A range of techniques each having its own set of advantages and disadvantages have been used so far for structuring and/or machining lithium niobate. Mechanical grinding and ultrasonic impact grinding were used to grind spherical depressions for geodesic lenses in Ti-indiffused lithium niobate substrates (Chen'77). A modified modulator/switch on a z-cut lithium niobate substrate with a deeply excavated slot between the two coupling waveguides, formed by ion-milling was demonstrated (Minakata'79). A horn structure ridge channel waveguide was fabricated by CF_4 plasma etching of lithium niobate (Lee'79). CHF_3 electron cyclotron resonance plasma etching was investigated as a means of dry etching lithium niobate for optical modulators (Shima'98) and further employed for fabrication of ridge optical waveguides (Mitsugi'98). Reactive ion etching was used to fabricate ridge type waveguide modulators in lithium niobate (Kaminow'74) and later employed to fabricate a 1.5μm wide and 1.1μm deep line with a mixture of CCl_2F_2, Ar and O_2 in an x-cut lithium niobate substrate (Jackel'81). Reactive ion beam etching (Ren'87) and sputter etching (Sopori'80) are a few other dry etching options also investigated earlier on. A few other maskless machining techniques with high power laser pulses with photon energies in excess of the bandgap of lithium niobate such as UV laser etching in Cl_2 atmosphere (Beeson'88) and laser driven chemical etching by a 248nm KrF and 270nm dye laser in the presence of powdered KF (Ashby'86) were also examined for creation of surface features. Sub band-gap laser machining of lithium niobate using a cw Ar-ion laser with sub-band gap photon

energies of 3.53eV in a direct write set up followed by selective removal of the laser processed substrate by chemical etching was also investigated (Christensen'95).

The technique of employing wet chemical etching of the proton exchanged regions with greatly enhanced etch rates when etched with HF (of the order of 10^3 observed by Mizuuchi'90) or a mixtures of HF and HNO_3 for structuring lithium niobate was first proposed by (Laurell'92). Mach-Zehnder modulators (Cheng'95) in z-cut lithium niobate and ridge waveguides in z-cut (Chen'95), x-cut (Lee'95) and y-cut (Cheng'97) lithium niobate have been reported using this technique.

A few innovative techniques for microstructuring lithium niobate with the end goal of fabricating useful structures finding applications in the field of optoelectronics however have been indigenously thought of and tried here. These techniques have exploited the use of selective wet or chemical etching which has the effect of distinguishing the presence of optically invisible ferroelectric domains in lithium niobate because of their significantly different etch rates. The technique of etching domains predefined by the technique of electric field induced poling of lithium niobate to effectively structure a range of very smooth, well-defined and deep two-dimensional μm scale spatial structures like ridges, trenches and micro-tips was first demonstrated by (Barry'98). This technique of microstructuring lithium niobate by etching the domains inverted by spatially selective electric field poling was used to fabricate alignment grooves for simplified optical fibre alignments (Eason'99) and ridge waveguides (Barry'99a). A similar two-step micro-structuring approach that takes advantage of the modified wet-etching characteristics of the optically treated lithium niobate surfaces (with laser fluences below the ablation threshold) was investigated to fabricate surface relief gratings (Mailis'00 and Brown'02). The use of the so-called optical poling technique (Ross'97 & Brown'99) which employs simultaneous application of optical and electrical field for producing periodically domain inverted structures in lithium tantalate and the light induced frustration (Barry'99b & Boyland'00) of etching in lithium niobate which combines the use of light and etching are a few other micro-structuring techniques also explored at this research centre. The research work presented in this thesis is an effort to progress and improve these developed microstructuring approaches and further augment the available set of structuring tools for demonstrating new or improved devices.

1.2 Outline of the thesis

The thesis begins with a brief historical background of lithium niobate in chapter 2. The same chapter then reviews the crystalline structure of lithium niobate and discusses some of its physical properties relevant to the research work presented such as the optical non-linearity and the piezoelectric properties.

The third chapter begins by introducing certain elementary concepts such as Curie temperature, spontaneous polarisation and domains for ferroelectric crystals leading on to the idea of domain inversion or *poling* as it is most commonly referred to. The idea of poling is further explained from the crystalline structure perspective. Several techniques that have been used to achieve domain inversion in lithium niobate such as crystal growth, heat treatment, Li_2O out-diffusion, Ti-indiffusion and e-beams are then briefly reviewed, finally concluding with a detailed explanation of the most commonly employed technique of room temperature electric field induced domain inversion.

Chapter 4 begins by discussing in brief some domain visualisation techniques used to assess the quality of domain inversion followed by a discussion at length of the frequently used visualisation approach of wet or chemical etching in the context of the potential application of this technique for micro-structuring lithium niobate. The chapter then describes some experimental investigations conducted to ascertain whether the widely used etchant mixture of 'HF and HNO_3 in the traditional ratio of 1:2' is indeed the ideal choice for achieving the optimal etch rates and better etch quality. A reaction formulation explaining the observed differential etching mechanism between opposing crystallographic z-faces is then proposed and discussed. The following section focuses on further experimental trials that revealed a latent etch mechanism in lithium niobate, also evidenced by Raman studies conducted within the research group. The chapter concludes by explaining the light-induced-frustrated-etching experiments performed to demonstrate its applicability for structuring surface relief gratings in un-doped lithium niobate.

Chapter 5 starts by introducing the concept of quasi-phase matching for non-linear interactions using periodically domain-inverted lithium niobate. The chapter then further discusses the proposed innovative but simple single-step technique of surface periodic poling, for achieving surface domain inversion to depths consistent with optical waveguides in lithium niobate. Some experimental results achieved using this technique to structure one and two-dimensional periodically poled structures in

lithium niobate are discussed. Quasi-phase-matched second harmonic generation experiments from a surface hexagonally poled planar annealed proton exchanged waveguide and a surface periodically poled Ti-indiffused channel waveguide in lithium niobate are presented and discussed. The chapter concludes with some preliminary experiments conducted to improve the demonstrated technique of surface periodic poling.

Chapter 6 briefly introduces the field of MEMS and MOEMS as a possible research topic that can be explored with the aid of the tools available for structuring lithium niobate. The chapter reports in details the entire fabrication procedure, integrating IC fabrication processes and ferroelectric domain engineering techniques, used to fabricate the first freestanding three-dimensional microstructures in lithium niobate. A suggested route for piezoelectric actuation of the micro-cantilever structures has been investigated. The chapter concludes by discussing some simple mathematical calculations to deduce the induced strains / changes in structural dimensions and the displacement and frequency of vibration for some test structures.

Chapter 7 summarises conclusions drawn from entire work and discusses future areas of work.

1.3 References

Ashby C.I.H, Brannon P.J, *Appl.Phys.Lett*, **49(8)**, 475, (1986)

Ballman A.A, *J. Am. Ceram. Soc*, **48**, 112, (1965)

Barry I.E, Eason R.W, Cook G, *Appl.Surf.Sc*, **143(1-4)**, 328, (1999b)

Barry I.E, Ross G.W, Smith P.G.R, Eason R.W, *Appl.Phys.Lett*, **74(10)**, 1487, (1999a)

Barry I.E, Ross G.W, Smith P.G.R, Eason R.W, Cook G, *Mater.Lett*, **37(4-5)**, 246, (1998)

Beeson K.W, Houlding V.H, Beach R, Osgood Jr, *J.Appl.Phys*, **64(2)**, 835, (1988)

Boyland A.J, Mailis S, Barry I.E, Eason R.W, *Appl.Phys.Lett*, **77(18)**, 2792, 2000

Brown P.T, Mailis S, Zergioti I, Eason R.W, *Opt.Mater*, **20(2)**, 125, (2002)

Brown P.T, Ross G.W, Eason R.W, Pogosyan A, *Opt.Commun*, **163(4-6)**, 310, (1999)

Chen B.U, Marom E, Lee A, *Appl.Phys.Lett*, **31(4)**, 263, (1977)

Chen K, Ihlemann J, Simon P, Baumann L, Sohler W, *Appl.Phys A*, **65**, 517, (1997)

Chen W.L, Chen R.S, Lee J.H, Wang W.S, *IEEE Photon.Technol.Lett*, **7(11)**, 1318, (1995)

Cheng R.S, Chen W.L, Wang W.S, *IEEE Photon.Technol.Lett*, **7(11)**, 1282, (1995)

Cheng R.S, Wang T.J, Wang W.S, *J.Lightwave.Technol*, **15(10)**, 1880, (1997)

Christensen F.K, Mullenborn M, *Appl.Phys.Lett*, **66(21)**, 2772, (1995)

Eason R.W, Barry I.E, Ross G.W, Smith P.G.R, *Electron.Lett*, **35(4)**, 328, (1999)

Ichikawa T, Kagami M, Ito H, *Opt.Lett*, **23**, 1138, (1998)

Jackel J.L, Howard R.E, Hu E.L, Lyman S.P, *Appl.Phys.Lett*, 38(11), 907, (1981)

Kaminow I.P, Ramaswamy V, Schmidt R.V, Turner E.H, *Appl.Phys.Lett*, **24**, 622, (1974)

Laurell F, Webjorn J, Arvidsson G, Holmberg J, *J.Lightwave Technol*, **10(11)**, 1606, (1992)

Lee C.L, Lu C.L, *Appl.Phys.Lett*, **35(10)**, 756, (1979)

Lee H.J, Shin S.Y, *Electron.Lett*, **31(4)**, 268, (1995)

Mailis S, Ross G.W, Reekie L, Abernethy J.A, Eason R.W, *Electron.Lett*, **36(21)**, 1801, (2000)

Minakata M, *Appl.Phys.Lett*, **35(1)**, 40, (1979)

Mitsugi N, Nagata H, Shima K, Tamai M, *J.Vac.Sc & Technol A*, **16(4)**, 2245, (1998)

Mizuuchi K, Yamamoto K, Taniuchi T, *Electron.Lett*, **26(24)**, 1992, (1990)

Nassau K, Levinstein, Loiacono G.M, *J.Phys.Chem.Solids*, **27**, 983, (1966)

Ren C.X, Yang J, Zheng Y.F, Chen L.Z, Chen G.L, Tsou S.C, *Nucl.Intr.Meth. B*, **19**, 1018, (1987)

Ross GW, Smith PGR, Eason RW, *Appl.Phys.Lett*, **71(3)**, 309, (1997)

Shima K, Mitsugi N, Nagata H, *J. Mater.Res*, **13(3)**, 527, (1998)

Sopori B.L, Phillips C.M, Chang W.S.C, *Appl.Opt*, **19**, 790, (1980)

Chapter 2

Lithium Niobate: A review of its crystal structure and properties

2.1 Introduction

Lithium Niobate has an extensive array of properties that has made it one of the most widely used ferroelectric materials, with one of its major applications being in the manufacture of surface acoustic wave devices, employed in high speed signal filtering in television-receivers and mobile phones. It does not occur naturally and is therefore a made-made material, synthesized in the single crystal form and thoroughly investigated for the first time for its structural and physical properties at the Bell laboratories, resulting in the publication of the first key papers (Nassau ’66 A&B, Abrahams ’66 A, B & C).

It was first discovered by Matthias ’49 to be a ferroelectric material, having a trigonal crystal structure characterised by large pyroelectric, piezoelectric, electro-optic and photoelastic coefficients. It is a naturally birefringent crystal and possesses a relatively large acousto-optic figure of merit in addition to the very strong bulk photovoltaic effect. This effect in turn combined with the linear electro-optic effect is known to produce a significant photorefractive effect. As a result of its extensive range of characteristics, together with its wide-scale application and availability of high-quality wafers means that it often dubbed as the silicon of non-linear optics and is widely sought after for applications for acoustic wave transducers, acoustic filters, optical amplitude modulators, optical phase modulators, second harmonic generators, Q–switches, beam deflectors, phase conjugators, optical waveguides, holographic memory elements and also holographic data processing devices.

2.2 Crystal structure

At room temperature its crystal structure is a distorted perovskite. It belongs to a trigonal crystal system, exhibiting a three-fold rotational symmetry about its *c*-axis. As shown in figure 2.1, it also exhibits a mirror-symmetry, across three planes that are sixty degrees apart and intersect along an axis referred to as the three-fold rotational axis, which together with the other symmetry operation places it into the 3m-point group. It also is a member of the R3c space group (Abrahams ’66 A). At temperatures

below its Curie temperature of $1120^0 C$, lithium niobate is ferroelectric in nature. The Curie temperature is known to strongly depend on the crystal composition (Carrurthers'71), with its value shifted by 150^0C by a change in the molar concentration of Li from 46-50 mole% (Rauber'78).

In ferroelectric form it is made up of planar sheets of oxygen atoms in a distorted hexagonal closed packed configuration with the lithium atoms and the niobium atoms occupying one third each of the octahedral interstices formed by the structure, leaving the remaining one-third sites vacant. In the + *c* direction the atoms are positioned at the interstices in this order Nb, vacancy, Li, Nb, vacancy, Li … .In the paraelectric state above the Curie temperature the Li atoms lie in the oxygen plane that is $c/4$ away from the Nb atoms, which in turn are centred between the two oxygen planes. This positioning of the atoms defines the materials non-polar state. However as the temperature falls below the Curie temperature the elastic forces come in to play and thus force the Li and the Nb atoms in to new positions relative to the oxygen octahedra, in turn producing a charge separation, causing lithium niobate to exhibit a spontaneous polarisation. It is also referred to as a displacement ferroelectric because of this effect. Figure 2.2 shows the positions of the Li and Nb atoms relative to the oxygen planes in both the ferroelectric and paraelectric phases.

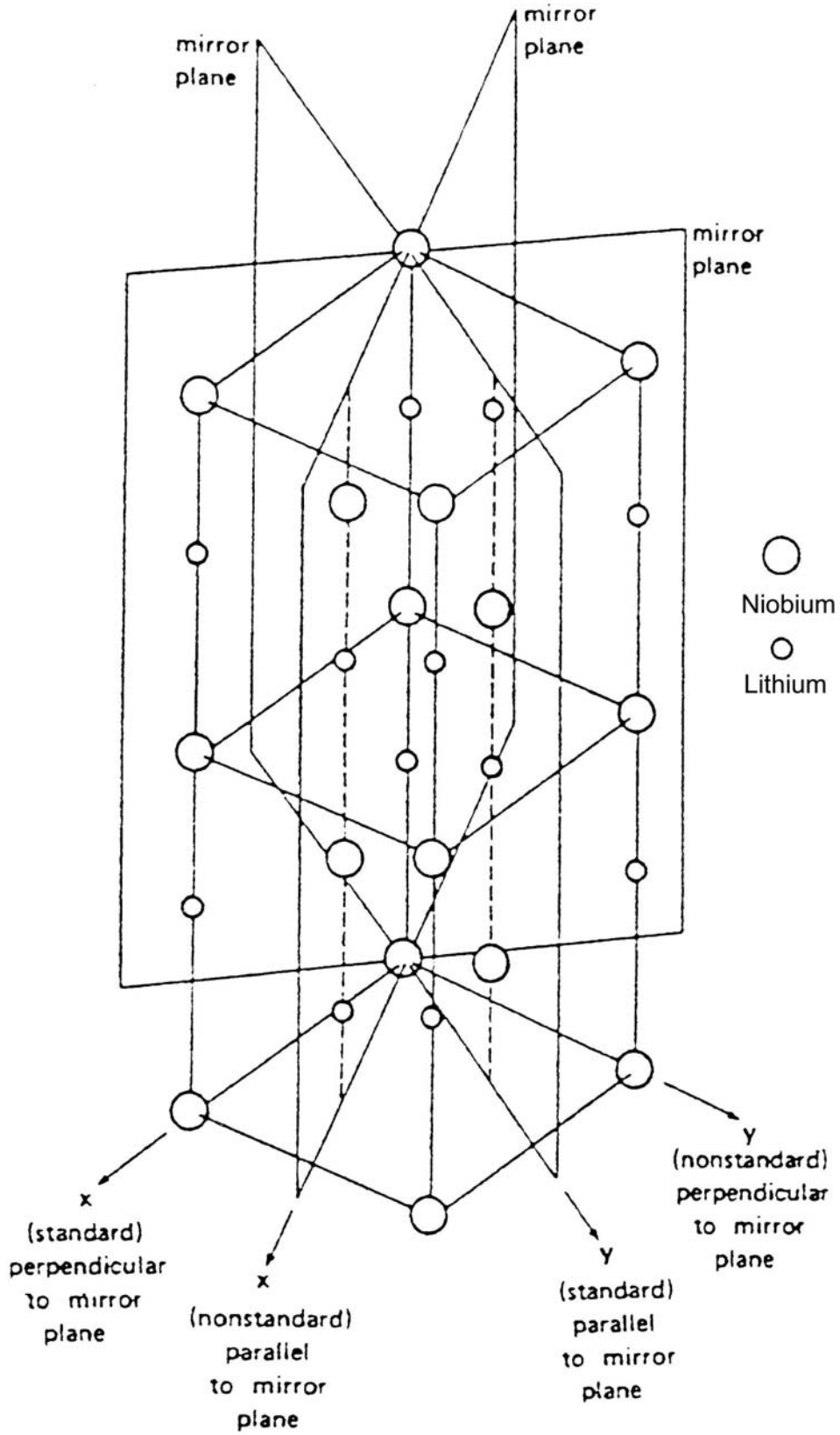

Figure 2.1 Figure showing the three mirror-planes of the lithium niobate unit-cell. The figure also shows the standard orientations of the *x*, *y* and *z* principal axes [after Weis'85]

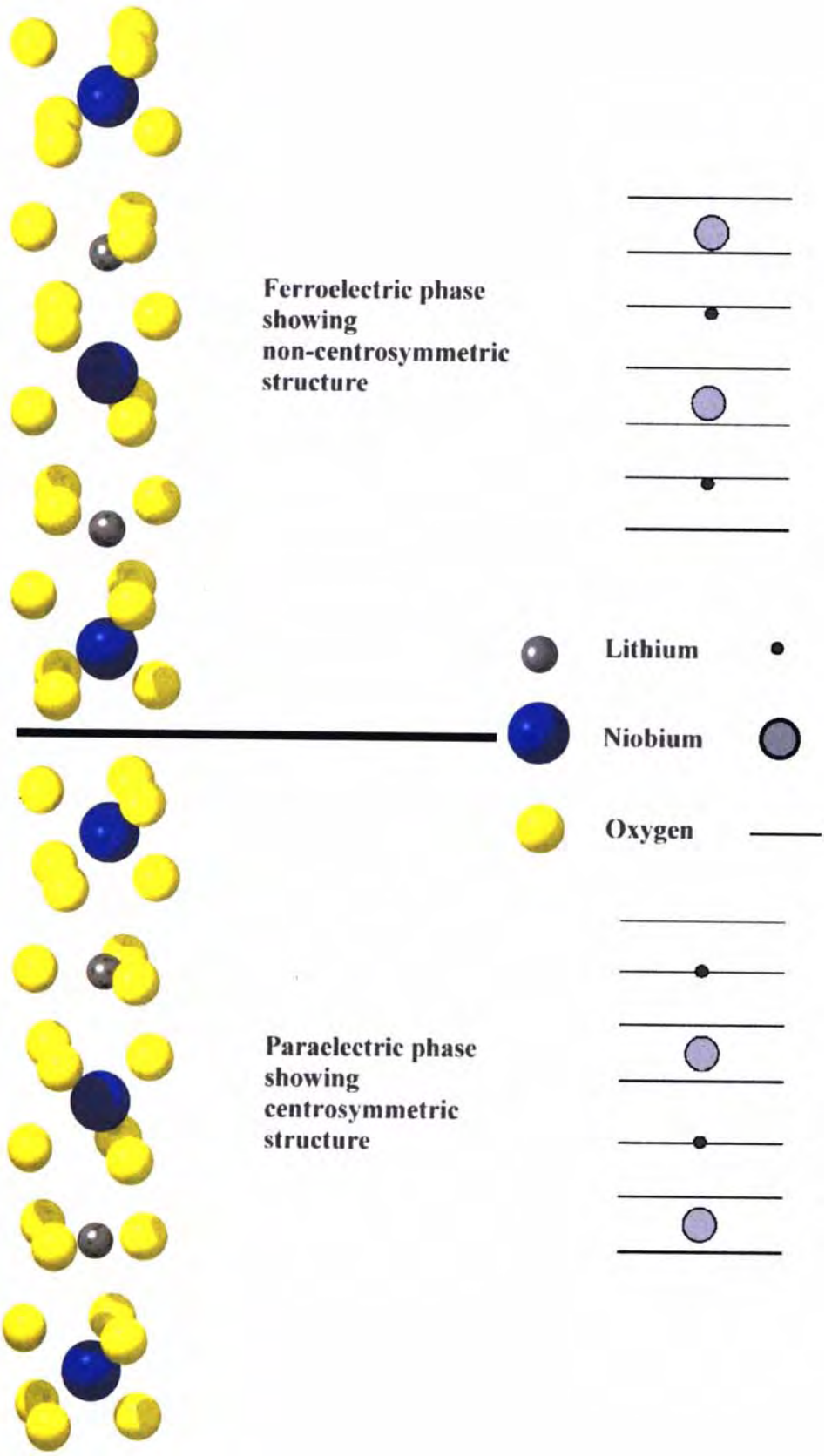

Figure 2.2 Figure showing the positions of lithium and niobium atoms with respect to the oxygen octahedra in the ferroelectric phase ($T<T_C$), and the paraelectric phase ($T\geq T_C$) [after Glass (74)]

Lithium niobate can have two different unit cells namely a hexagonal one (figure 2.3) or a rhombohedral one (figure 2.4). In the hexagonal unit cell a *c*-axis is defined as an axis about which the crystal exhibits a three fold rotational symmetry. The ferroelectric dipoles are aligned along this axis and so the *c*-axis has two corresponding faces, which are perpendicular to this axis and are referred to as the +*c* face and the -*c* face. The standard method of determining the sense (Weiss '85) of the *c*-axis is to compress the crystal along this axis. On doing so, the face, which becomes negative on compression, is called the positive *z*-face. Alternatively the *c*-axis direction is also defined via the face that becomes positive on cooling (Boyd '64).

Both these ideas can be understood qualitatively if we consider the motion of the Li and the Nb atoms relative to the oxygen octahedra on compression or cooling. When the crystal is cooled the elastic forces within the crystal pull the atoms further apart relative to the oxygen octahedra thereby, increasing the net polarisation along the ***c-axis*** and in turn introducing a deficiency of negative compensating charge on the positive face thereby making it more positive. On compression along the *c*-axis the ions move closer to the places that they would have occupied if the crystal were in the paraelectric state, thereby reducing the net polarisation, leaving an excess amount of negative compensating charge on the positive face thereby making it negative.

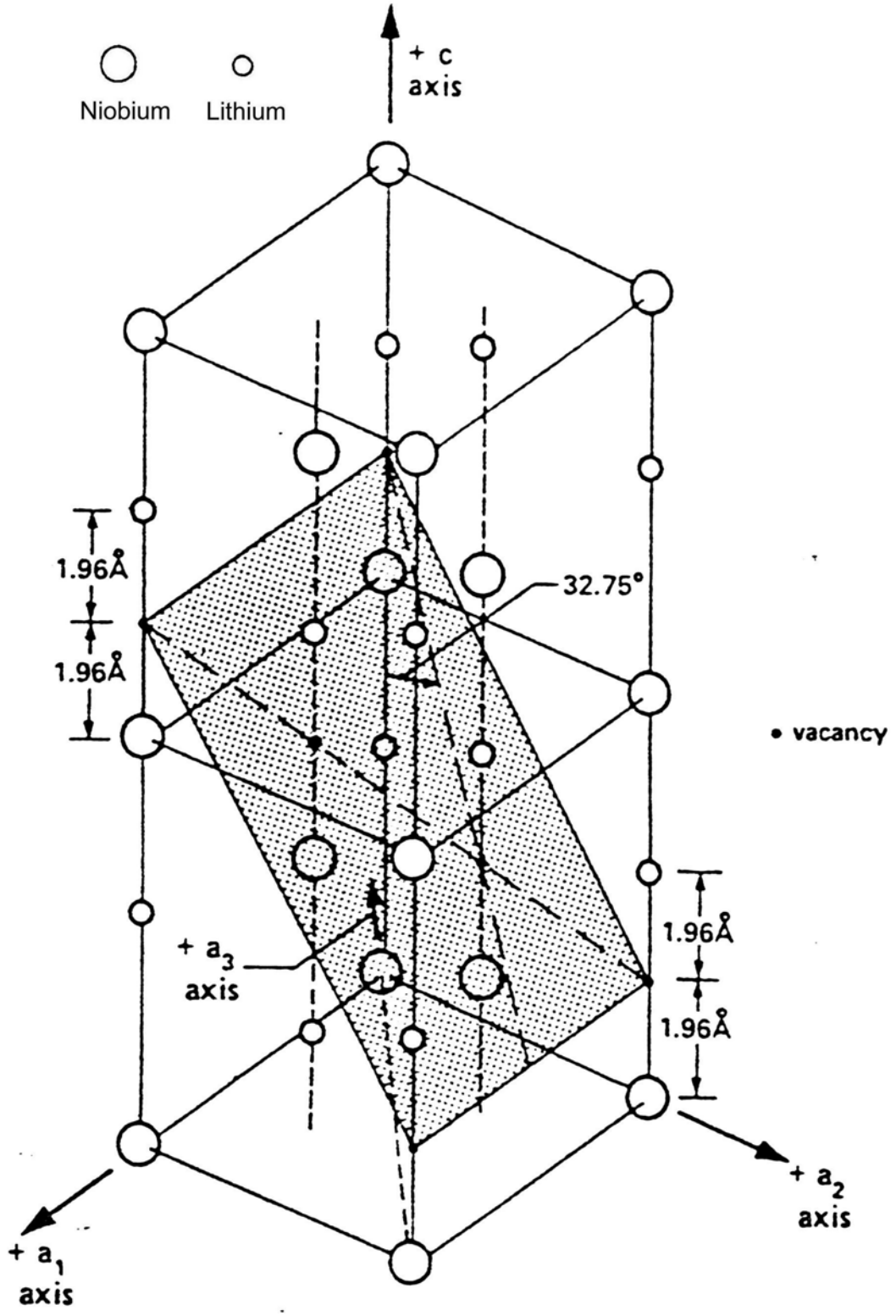

Figure 2.3 Figure showing a conventional hexagonal unit-cell of lithium niobate, with the hexagonal axes (a_1, a_2, a_3, c) and the cleavage plane $\left(0,1,\bar{1},2\right)$ [after Weis'85]

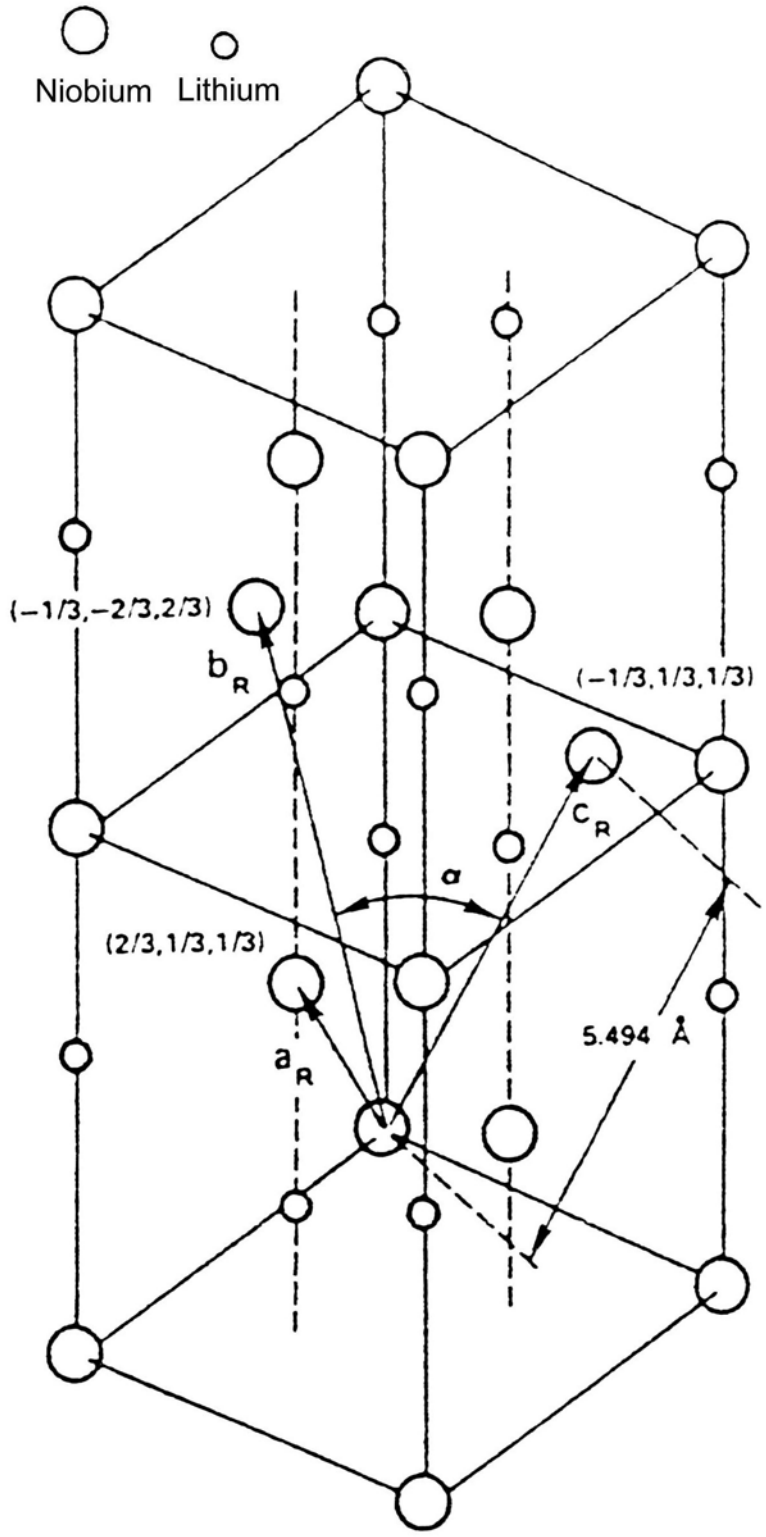

Figure 2.4 Figure showing a conventional rhombohedral unit-cell of lithium niobate, with the rhombohedral axes (a_R, b_R, c_R) and the angle α between them. [After Weis'85]

2.3 Cleavage Planes

Lithium niobate cleaves naturally along the plane $\{0,1,\bar{1},2\}$. As it has a three-fold rotational symmetry it cleaves along the three equivalent planes $(0,1,\bar{1},2),(\bar{1},0,1,2)$ and $(1,\bar{1},0,2)$. The $(0,1,\bar{1},2)$ plane, having the vacant octahedral sites and lying midway between the planes of Li and Nb atoms, qualitatively explains its cleavage. It can be reasonably assumed that cleavage occurs at this vacancy plane, as the bonding perpendicular to this plane, between the positive ions is correspondingly weaker. A coordinate system (shown in figure 2.1) used to describe the physical properties, can be defined once the crystallographic axes have been defined. This is usually a Cartesian (*x*, *y*, *z*) system with the *z*-axis chosen parallel to the *c*-axis and the *x*-axis chosen to be parallel to one of the *a*-axes. The *y*-axis is chosen so that a right-handed system is formed, resulting in it lying in one of the planes of mirror symmetry. The sense of the *z*-axis is the same as the *c*-axis.

Historically lithium niobate has been prepared in both stoichiometric and congruent forms, the latter being the preferred composition. The stoichiometric form holds the Li: Nb ratio at 1:1 and is an attempt to replicate the exact chemical formula ***$LiNbO_3$***. Congruently melting material starts with a composition mixed to give a Li: Nb ratio of 0.94 or having 48.45 mol% of ***Li_2O*** in the start mixture (Lawrence). Crystals with other than congruent starting mixes have been produced but are known to have greater inconsistencies in their optical properties. Though stoichiometry is one of the most important properties of the material, it is also one of the least well measured. The best and most reliable possible indicator of the sample stoichiometry is via the measured Curie temperature (Carruthers ’71 & Bergman ’68). Comparing the Curie temperature of a sample with that of a known stoichiometry uniquely determines the chemical composition of that sample. The lattice parameters are in-turn dependent on the exact composition of $LiNbO_3$.

The thermal expansion of the hexagonal lattice parameter ‘*a*’ can be explained by the tilt of oxygen octahedra with increasing temperature thereby producing a nearly linear thermal expansion of that lattice parameter. The contraction of the hexagonal lattice parameter ‘*c*’ in the temperature range 600^o – 1000^o C is due to the decreasing edge length of the octahedra as the Nb ions move towards their paraelectric position.

2.4 Physical Properties

2.4.1 Pyroelectric Effect

This is the change in the spontaneous polarisation exhibited by the material as a result of the change in its temperature (Prokhorov '90). For a small change in temperature, the change in the spontaneous polarisation is linear with temperature and is of the order of $4\times10^{-5}C/Km^2$ (Savage '66). If ΔP is the change in the spontaneous polarisation as a result of the change in the temperature, ΔT, then the relationship between them can be expressed as: $\Delta P_i = \xi_i \Delta T$, where ξ_i is a pyroelectric tensor, provided this relationship is linear over the range of ΔT under consideration. This effect is a result of the motion of the Li and the Nb atoms relative to the oxygen octahedra. As the movement of these atoms is only along the direction parallel to the *c*-axis the pyroelectric tensor is of the form:

$$\xi_i = \begin{bmatrix} 0 \\ 0 \\ \xi_3 \end{bmatrix} \qquad \textbf{2.1}$$

ξ_3 being negative, indicating that upon cooling the positive *z*-face of the crystal is more positively charged. The pyroelectric effect is an effect which is well known amongst crystals lacking inversion symmetry in their structure, and is a manifestation of the relationship in the crystal between the temperature change and polarisation induced voltage. It is a simpler effect as compared to the other stress related effects, described later, such as the piezoelectric and the elasto–optic effects and has a single non-vanishing coefficient related to a unique axis, namely the *z*-axis. This is the reason why we do not see this effect in the *x* or *y* directions. The effect has two basic forms, a primary one in which a temperature change produces a change in the electric polarisation and a secondary one, which can be observed when the crystal is allowed to change its shape, a case in which the temperature change induces a strain in the crystal lattice.

2.4.2 Piezoelectric Effect

This is a stress related effect where an applied stress induces a polarisation of the material concerned. The relationship between the induced polarisation and the stress, for small values of the induced stress can be expressed as:

$$\mathbf{P} = \mathrm{d}\,\sigma \qquad \textbf{2.2}$$

Where σ is a second-rank stress tensor and d is a third-rank piezoelectric tensor.

We can rewrite this equation in the tensorial form as:

$$\boldsymbol{P}_i = \sum_{jk} d_{ijk}\sigma_{jk} \qquad \textbf{2.3}$$

Thermodynamical arguments further require that

$$\sigma_{jk} = \sigma_{kj} \qquad \textbf{2.4}$$

The d_{ijk} tensor will thus have eighteen elements. However as lithium niobate has a 3m point symmetry and since the Neumann principle imposes the condition that any tensor describing a physical property of a crystal must exhibit no less symmetry than that of the crystal, the piezoelectric stress tensor can be reduced to having just four independent coefficients namely d_{15}, d_{22}, d_{31} and d_{33} (Weis'85)

The converse piezoelectric effect is the direct inverse of the piezoelectric effect, meaning that a piezoelectric material will exhibit a change in its shape as a result of an applied electric field. By thermodynamical arguments it can be proved that the coefficient relating the induced strain to the applied electric field is the same as that in the direct case, which is the coefficient relating the induced polarisation to the applied stress (Nye'57). So in the tensor form the converse piezoelectric effect can be expressed as:

$$S_{jk} = \sum_{jk} d_{ijk}\,\bar{E}_i \qquad \textbf{2.5}$$

where S again is the second-rank strain tensor and E is the applied electric field.

2.4.3 Photoelastic Effect

A regular crystalline lattice has a set of spring constants associated with the interatomic bonds that form the lattice. The way in which these bonds are formed and hence the way in which the lattice is formed is governed by the minimum interatomic potential energy. This requirement means asymmetric lattices have bonds having

different strengths in different directions. So on subjecting such a crystal to a stress the bonds are distorted differently bringing about a change in some of its properties. For relatively small stresses, the magnitude of the induced strain is linearly related to the stress. This strain is in itself related back to the optical properties through an effect called the photoelastic effect, which is a change in the refractive index as a result of the strain in the material. This anisotropic relationship can be expressed as:

$$\Delta\left(1/n^2\right)_{ij} = \sum_{kl} P_{ijkl} S_{kl} \qquad \textbf{2.6}$$

Where $\Delta\left(1/n^2\right)_{ij}$ is a second-rank tensor, which gives a measure of the change in the relative pemittivity of the material. P_{ijkl}, is a fourth-rank photoelastic (strain optic) tensor and S_{kl} is a second rank stain tensor.

As $\Delta(1/n^2)_{ij} = \Delta(1/n^2)_{ji}$, the fourth rank tensor P_{ijkl}, containing 81 elements can be reduced to one with 36 independent elements and can be expressed by a 6×6 matrix. Once again the application of the Neumann principle to P_{ijkl} will then reduce it to a vector with just eight independent elements, p_{11}, p_{12}, p_{13}, p_{14}, p_{31}, p_{33}, p_{41}, p_{44}. A secondary effect also plays an important role in the determination of the values of these coefficients. This effect manifests itself as a result of the coupling of two different effects. The applied stress produces an electric field, because of the piezoelectric effect, which in turn will produce a change in the refractive index as a result of the electro-optic effect. Thus the net effect is a contribution of both the primary photoelastic effect and the inseparable secondary effect.

2.4.4 Bulk Photovoltaic Effect

This effect can be perceived as a flow of a short circuit current through a solid as a result of its uniform illumination. The tensor relationship between the short circuit current density vector and the illumination can be expressed as:

$$\boldsymbol{J} = \sum_{jk} \alpha_{ijk} \boldsymbol{E}_j \boldsymbol{E}_k^* \qquad \textbf{2.7}$$

where E_j and E_k are components of the complex light electric field vector and α is the photovoltaic tensor. Since $\boldsymbol{E}_j \boldsymbol{E}_k^* = \boldsymbol{E}_j^* \boldsymbol{E}_k$, we can express α_{ijk} in terms of a 3×6

matrix with eighteen independent elements. Further application of the Neumann principle, reduces α_{ijk} to just four independent coefficients $\alpha_{15}, \alpha_{22}, \alpha_{31}$ and α_{33}.

2.4.5 Photorefractive Effect

Optically induced change in the refractive index is referred to as the photorefractive effect. Except for optical storage or holographic applications designed to use such a change, the photorefractive effect is an unwelcome phenomenon known to have deleterious effect on the propagating beam quality, consequently deteriorating the optical performance of the device. This behaviour was first reported in lithium niobate as early as 1966, by (Ashkin'66) and then by (Chen'67), and results from an intensity gradient of the illuminating light which subsequently has the effect of producing a charge distribution gradient. Lithium niobate is susceptible to this effect with shorter wavelength radiation and the effect is more pronounced at visible wavelengths around *532 nm* (Miller'98). This effect is a combination of two effects and cannot be thought of as a single response. The mechanism is the activation of charge in the path of light, followed by their migration as a result of the photovoltaic effect, followed by an electro-optic effect. In lithium niobate the charge migration is predominantly as a result of the photovoltaic effect. However the charge migration may at times be as a result of drift or diffusion mechanisms.

2.4.6 Other Fundamental Optical properties

Lithium niobate is classified as a negative uniaxial crystal with two different refractive indices, with its extraordinary refractive index n_e, being lower than or equal to its ordinary index of refraction n_o. This birefringent property makes it suitable for use in many integrated optical, electro-optical and non-linear optical applications. The birefringence of lithium niobate is relatively large, approximately 0.1 (Lawrence'93). When dealing with simple optical properties the other factor that is relevant is its optical transmission. The optical absorption characteristics measured for the bulk crystal have been found to be approximately 0.2 dB/cm, for measurements throughout the visible and the near infrared spectral region (Lawrence'93). At wavelengths below ≈0.4 μm the material is absorbing but there is a good transmission in the near infrared range till ≈5 μm, from where an extensive phonon absorption band causes opacity

until about 60μm. The absorption curve has a range from 0.4 μm to about 5 μm with a few dips in the middle, resulting from resonance or band absorption.

Congruent lithium niobate has an ordinary refractive index n_o, which ranges from about 2.34 to 2.28 and an extra-ordinary refractive index n_e, which ranges from about 2.25 to 2.20, over the visible range. The temperature dependent Sellmeier equation (EMIS '89), for congruent lithium niobate gives a more accurate value and can be expressed as below:

$$n_o^2 = 4.9048 + \frac{1.178x10^5 + 2.314x10^{-2}F}{\lambda^2 - \left(2.1802x10^2 - 2.9671x10^{-5}F\right)^2} - 2.7153x10^{-8}\lambda^2 + 2.1429x10^{-8}F \quad \textbf{2.8}$$

$$n_e^2 = 4.5820 + \frac{0.9921x10^5 + 5.271x10^{-2}F}{\lambda^2 - \left(2.1090x10^2 - 4.9143x10^{-5}F\right)^2} - 2.194x10^{-8}\lambda^2 + 2.297x10^{-8}F \quad \textbf{2.9}$$

where λ is the wavelength in vacuum, in nm, and F is related to temperature by the following equation:,

$$F = (T_C - T_0) \times (T_C + T_0 + 546) \quad \textbf{2.10}$$

Where T_c is the temperature in centigrade and $T_o = 24.5\,^0$C

Table 2.3.6, shown below gives the ordinary and extra-ordinary refractive indices for a few relevant wavelengths.

λ / nm	n_o	n_e
488	2.3486	2.2589
632.8	2.2866	2.2028
1300	2.2205	2.1449

Table 2.3.6 Showing values of the n_o and n_e for three different wavelengths

2.4.7 Electro-optic effect

The electro-optic effect is a classical feature that all non-centrosymmetric crystals (lacking a centre of symmetry) exhibit. The effect was first detected by (Peterson'64). The magnitude of a crystal's electro-optic coefficients can vary over four orders of

magnitude even amongst similar types of crystals. The two commonly observed electro-optic effects are the linear electro-optic effect, referred to as the Pockels effect and the quadratic electro-optic effect referred to as the Kerr effect.

This electro-optic effect can further be explained by using an optical property of the crystal called the indicatrix, which relates the principal dielectric axes (referred to as *x*, *y*, *z*) to their relative refractive indices and is defined as:

$$\frac{x^2}{n^2(x)}+\frac{y^2}{n^2(y)}+\frac{z^2}{n^2(z)}=1 \qquad \textbf{2.11}$$

When an electric field is applied a corresponding change in the refractive index occurs. For the above equation to remain applicable new values of *x*, *y*, *z* must be found. These new values x', y', z' are related to the old *x*, *y*, *z* values by a third rank tensor with 27 elements. Symmetry conditions can then be used to reduce this tensor to one having just four independent elements. In the reduced subscript notation the tensor for lithium niobate can be expressed as

$$r_{ijk}=\begin{bmatrix} 0 & -r_{22} & r_{13} \\ 0 & r_{22} & r_{13} \\ 0 & 0 & r_{33} \\ 0 & r_{42} & 0 \\ r_{42} & 0 & 0 \\ -r_{22} & 0 & 0 \end{bmatrix}$$

The general relationship can be written as $\Delta n \sim r\boldsymbol{E}$, where r is the effective coefficient of the electro-optic tensor that links the specific refractive indices in the *x*, *y*, and *z* directions with directions of the applied electric field. Typical values of the magnitudes of the high frequency (Turner'66) (under constant strain, clamped) and the low frequency (Bernal'66) coefficients (under constant stress, free), at 633nm are of the order $10^{-12} m/V$. The temperature dependence of the electro-optic coefficients was found to be of the order of $5\times10^{-4}/^{0}C$ by (Zook'67). From the indicatrix notation the actual value of Δn can be deduced for the typical applied field, say in the z direction as:

$$\Delta n_e=-n_e^3\frac{r_{33}}{2}\boldsymbol{E}(z) \qquad \textbf{2.12}$$

$$\Delta n_o = -n_o^3 \frac{r_{13}}{2} \boldsymbol{E}(z) \qquad \textbf{2.13}$$

Similar equations for any other arbitrary orientations can also be deduced.

2.4.8 Non-linear optical property

A qualitative explanation of the non-linear effect in lithium niobate can be deduced with the aid of the power series expansion stated below, that relates the induced polarisation **P** to the applied electric field **E**

$$\mathbf{P} = \in_0 \left(\chi^{(1)} \boldsymbol{E} + \chi^{(2)} \boldsymbol{E}^2 + \chi^{(3)} \boldsymbol{E}^3 + ... \right) \qquad \textbf{2.14}$$

Where the $\chi^{(n)}$ are the susceptibility tensors of rank (n+1) and $\in_0$ is the vacuum permittivity. When an electromagnetic disturbance propagates through the medium this oscillatory electric field generates an induced polarisation in the medium. For low intensity of the propagating field, the displacement of the electrons in the medium from their equilibrium position is insufficient to induce any nonlinear behaviour. This means that any higher order terms of equation 2.14 can safely be eliminated, as they do not play a significant role in adding to the polarisation. The polarisation can therefore be expressed as a linear equation:

$$\mathbf{P} = \in_0 \chi^{(1)} \mathbf{E} \qquad \textbf{2.15}$$

However as the electric field becomes stronger these higher order terms start playing a significant role and can no longer be set aside; the response of the medium to the electric field is now a non-linear one. If the applied field is of the form $E_0 \cos \omega_1 t + E_0 \cos \omega_2 t$, then the right hand side of the first equation will have terms such as $\omega_1 + \omega_2, \omega_1 - \omega_2, 2\omega_1, 2\omega_2$ leading to a range of effects such as second harmonic generation, sum frequency generation, difference frequency generation and so forth. The size of the effect is dependent on the values of the non-linear coefficients $\chi^{(n)}$ and the value of the incident optical field. Values for the second order susceptibility is usually given in terms of the non-linear optical coefficient *d*, which is a tensor measured experimentally and related to $\chi^{(2)}$ by the equation:

$$2d = \chi^{(2)} \qquad \textbf{2.16}$$

2.5 Summary

The chapter briefly reviewed the crystalline structure of lithium niobate and also discussed some of the exhibited physical properties relevant to the presented research work such as the non-linear and the piezoelectric property.

2.6 References

Abrahams S.C, Hamilton W. C, Reddy *J.M, J. Phys. Chem. Solids*, **27**, 1013, 1966B.

Abrahams S.C, Levinstein H. J, Reddy J.M, *J. Phys. Chem. Solids*, **27**, 1019, 1966C.

Abrahams S.C, Reddy J. M, Bernstein J. L, *J. Phys. Chem. Solids*, **27**, 997, 1966A

Ashkin A, Boyd G.D, Dziedzic J.M, Smith R.G, Ballman A.A, Levinstein J.J, Nassau K, *Appl. Phys. Lett*, **9**, 72, 1966.

Bergman J.G, Ashkin A, Ballman A.A., Dziedzic J.M, Levinstein H.J, Smith R.G, *Appl. Phys. Letts*, **12(3**), 92, 1968.

Bernal E, Chen G.D, Lee T.C, *Physics Lett*, **21**, 259, 1966.

Boyd G. D, Miller R.C, Nassau K, Bond W.L, Savage A, *Appl. Phys. Lett*, **5(11)**, 234, 1964.

Carruthers J.R, Peterson G.E, Grasso M, Bridenbaugh P.M, *J. Appl. Phys*, **42**, 1846, 1971.

Chen F.S, *J. Appl. Phys*, **38**, 3148, 1967.

EMIS Data review Series No. 5, '*Properties of Lithium Niobate'*, INSPEC, London, 1989.

Glass A.M, Von der Linde D, Negran T.J, *Appl. Phys. Lett*. **25**, 233, 1974.

Lawrence M, *Reports on Progress in Physics*, **56(3)**, 363, 1993

Matthias B.T, Remeika J.P, *Physical Review*, **76(12**), 1886, 1949.

Miller G.D, *Periodically poled Lithium Niobate: Modelling, fabrication, and non-linear optical performance*, PhD Dissertation, July'1998

Nassau K, Levinstein H. J, Loiacono G. M, *J. Phys. Chem. Solids*, **27**, 983, 1966A.

Nassau K, Levinstein H. J, Loiacono G. M, *J. Phys. Chem. Solids*, **27**, 989, 1966B.

Nye J.F, *Physical Properties of Crystals*, Oxford University Press, Oxford

Peterson G.E, Ballman A.A, Lenzo P.V, Bridenbaugh P.M, *Appl. Phys. Lett*, **5**, 62, 1964.

Prokhorov A. M, Kuzminov Yu. S, *Physics and Chemistry of Crystalline Lithium Niobate*, Adam Hilger, Bristol, 1990.

Rauber A, Current Topics in Materials Science, 481-601, Ed. Kaldis E, North-Holland

Savage A, *J. Appl. Phys*, **37**, 3071, 1966.

Turner E.H, *Appl.Phys.Lett*, **8**, 303, 1966.

Weiss R.S, Gaylord T.K, *Appl. Phys. A*, **37**, 191, 1985.

Zook J.D, Chen D, Otto G.N, *Appl. Phys. Lett*, **11**, 159, 1967

Chapter 3
Domain Inversion and Electric field poling

3.1 Introduction

Ferroelectric materials such as lithium niobate encompass a wide range of applications as a result of the broad spectrum of physical properties that it exhibits. Many of these applications and quasi-phase-matching for optical frequency conversion in particular are highly dependent on the ability to precisely engineer the domains within the ferroelectric material. In simple words the quality of the device of which the material is an integral part, is directly governed by the potential to expertly engineer the domains within the material. For highly efficient quasi-phase-matched non-linear optical frequency conversion devices in particular, the need is to precisely manipulate the ferroelectric domains at the micron scale.

Lithium niobate because of its range of optical and non-linear optical properties is one of the most widely researched materials for generation of compact sources of coherent short-wavelength(blue)-light with a prime application in high- density optical data storage. These non-linear optical devices require the fabrication of high precision periodically inverted ferroelectric domain structures with ≈ micron dimensions. The fabrication of such strictly defined patterned structures in ferroelectrics has been one of the most challenging requirements within the non-linear optical research community to date, with various routes being taken by different experimental groups.

Developing a reliable technique to achieve this objective of precise-domain-inversion, has been the motivation for a large part of this research. The target here was to both demonstrate such a technique and also present an understanding of the underlying mechanism.

This chapter begins by explaining some elementary concepts related to ferroelectrics such as Curie temperature, spontaneous polarisation, domains within ferroelectric materials, leading on to understanding of the idea of domain inversion. Several techniques that have been used to achieve this domain inversion in lithium niobate are then briefly reviewed.

3.2 Ferroelectrics and Paraelectrics

A ferroelectric is a pyroelectric material each of whose unit cells exhibit a spontaneous electrical polarisation, which has two or more orientational states, which can be reversed from one state to the other under the influence of some external force. The spontaneous polarisation, or the electrical dipole moment per unit volume, is constrained to one or more of the crystal axes. In case of materials like $BaTiO_3$ the spontaneous polarisation can be orientated along six equivalent directions, whereas in the case of ferroelectrics such as $LiTaO_3$ and $LiNbO_3$ because of their respective structural configuration the polarisation can be orientated along just two states and can be successfully switched between them.

Crystals, which exhibit a spontaneous polarisation or a permanent internal electrical dipole moment even in the absence of an external electrical field, are called polar crystal (Lines'77), with the inherent asymmetry of the crystalline structure responsible for the net effect. The asymmetry creates a unique polar axis within the crystal with the spontaneous polarisation aligned along that direction. The two anti-parallel directions of the spontaneous polarisation within the unit cell mean that the polarisation could be denoted as having a positive or a negative value or sign. However what actually identifies a ferroelectric is the compliance to the fact that the spontaneous polarisation can be switched from one state to the other under the influence of an external electric field with the value of the field that produces this switching being referred to as the coercive field 'E_c' of the crystal. This physically corresponds to the displacements of the constituent positive and negative ions in response to the externally applied field. This concept can be clarified by visualising this effect within a common ferroelectric archetype structure referred to as a perovskite. A prototype perovskite structure shown in figure 3.1 is cubic with a formula unit ABO_3, composed of oxygen octahedra with the metal ion B located within the octahedra and the metal ion A outside it. The adjacent oxygen octahedra are joined by a shared oxygen with a third one occupying spaces in between. A ferroelectric phase transition results from the relative displacements of the ions along the polar axis in response to an external field. Crystal imperfections, temperature, pressure and electrical conductivity all affect the reversibility of the polarisation within the ferroelectric (Lines '77).

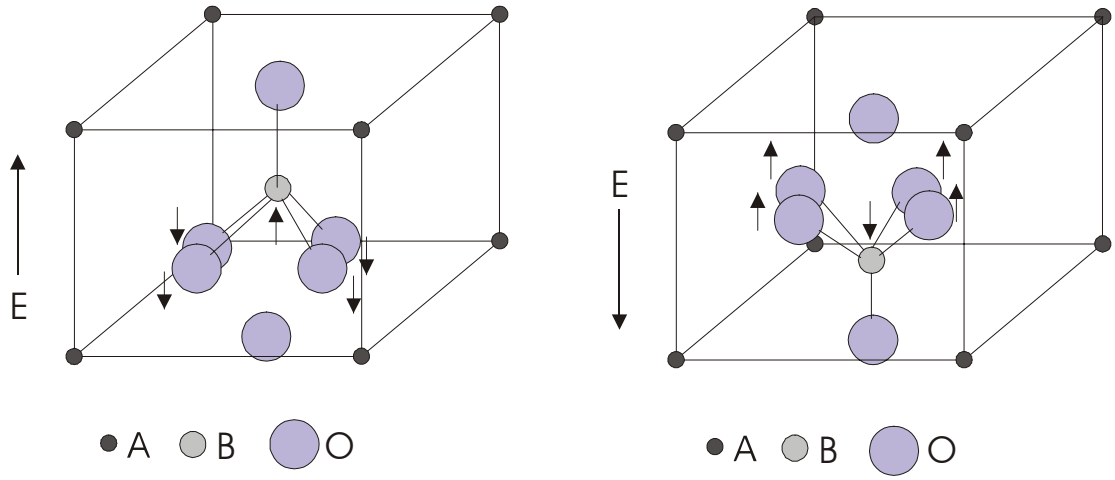

Figure 3.1 Figure showing a prototype cubic unit-cell structure of a ferroelectric like lithium niobate.

Ferroelectrics posses a phase transition temperature above which the crystal ceases to display the spontaneous polarisation, and transforms into the non-polar paraelectric phase. The phase transition can either be due to the ordering of the inherent dipoles or due to a distortion in the crystalline structure and consequently ferroelectrics are categorised as either being disorder-order or displacive in nature. In the paraelectric phase the unit cell acquires a symmetric ionic configuration, which effectively eliminates the internal dipole moment, producing a non-pyroelectric state above the Curie temperature. When the crystal is cooled through the Curie temperature the higher symmetry of that phase is disrupted as the elastic restoring forces return the crystal to the ferroelectric phase, wherein the centre of positive and negative charges no longer coincide. The recovered value of the spontaneous polarisation increases with a decrease in temperature and the relation between the spontaneous polarisation and the temperature can be best understood by considering the distortion in the unit cell just below the Curie temperature. At the Curie temperature the relative displacement of the oppositely charged ions is small and it is relatively easy to eliminate or reverse the polarisation by applying a small electric field in a direction opposite to the spontaneous polarisation. As the crystal continues to cool down from the Curie temperature, further distortion of the unit cell increases charge separation and hence the value of the spontaneous polarisation and in turn the coercive field.

Finally we conclude this explanation of ferroelectrics by elucidating the idea of domains. A ferroelectric may be composed of many such regions within which the

electric dipole moment of each unit cell is aligned parallel to or anti-parallel to the polar axis, or alternatively the ferroelectric may exist in a single domain or single crystal state. When the ferroelectric is cooled through the Curie temperature the multi-domain configuration that ensues minimises the free energy of the crystal with the resultant state exhibiting no net polarisation as a consequence of the cancellation of the respective polarisations of the different domains. However if a sufficiently high electric field is applied along the crystal's polar axis, these domains can align with each other to form a single domain structure, which possess a net macroscopic polarisation. The process of reversing the polarisation of a domain is called domain switching (Zaky'70), with two supposedly (Fatuzzo'62) field-dependent mechanisms responsible for the switching. Polarisation reversal may occur from the growth of an existing domain as a result of sideways motion of domain walls or domain switching which may occur via the random nucleation and subsequent propagation of these new domains in the polar direction, with the latter mechanism being more prominent at higher electric fields.

3.3 Domain Inversion or Poling of ferroelectric Lithium Niobate

As we intend to further explain poling in lithium niobate, it would be worth dwelling briefly in this section on the specifics of its crystal structure in the context of the discussion above. Its distorted perovskite structure has a density of 4.64 g/cm^3 at $25^0 C$ and a unit-cell volume of 318.221 $Å^3$. The corresponding parameters for a rhombohedral unit cell, with two formula units per cell or a hexagonal unit cell, with six formula units per cell are (Rauber'78).

a_R = 5.496Å and α_R = 55.87Å

Or a_H = 5.150Å and c_H = 13.867Å

As explained earlier the crystalline structure composed of distorted oxygen-octahedra that are slightly rotated one above the other, have the metal cations located at the interstitial sites sequentially. The metal ions are much smaller in sizes as compared to the oxygen ions and are not equidistant (Abrahams'66) from the parallel oxygen planes, with corresponding metal-oxygen plane distances being $Li^{+1} - O^{-2} = 0.71\,Å$ and 1.597 Å and $Nb^{+5} - O^{-2} = 0.897\,Å$ and 1.413 Å. The oxygen ions are arranged such that they form triangles in planes parallel to each other and perpendicular to the optical axis, with the maximum distance between them in the plane being 3.62 Å. The

displacement of the metal ions along the z-axis, the only allowed direction of displacement, lends the crystal the dual states. The typical displacements of the metal ions Li^{+1} and Nb^{+5} are $0.45\,\text{Å}$ and $0.25\,\text{Å}$ respectively. It acquires the polar ferroelectric phase from the non-polar paraelectric phase from the resulting displacements, with the direction of displacement deciding the direction of the spontaneous polarisation P_s of the ferroelectric phase.

At room temperature lithium niobate is in a ferroelectric phase with in general a multi-domain structure (Prokhorov'90) with each domain or regions thought of as that volume of the crystal within which all the electric dipoles are aligned along a definite direction, either parallel or anti-parallel to the optical axis of the crystal. The 180^0 domains with their electric dipoles oriented parallel to each other thus contribute to a net polarisation to that domain.

The polarisation of a single domain region produces a depolarising field that affects the adjoining regions. When the crystal is first grown it contains domains with different orientations minimizing the overall depolarising field. The depolarising fields are compensated by external charges on the surface of the crystal or by rearrangement of charges within the crystal. A multi-domain crystal exhibits greatly reduced piezoelectric response because of the averaging effect of the different domain orientations.

Heating multi-domain crystals above the Curie temperature and then cooling them down to room temperature in the presence of an electric field produce the useful single-domain crystals. This poling technique, which has the effect of aligning the domains with differing electric-dipole orientation along the direction of the externally applied field is named field cooling and is the method employed during crystal-growth of the as-purchased single crystal samples. However, in the absence of a poling field it leaves the crystal in a multi-domain structure and is called zero-field-cooling. Hence commercially available ferroelectric lithium niobate is a single-domain at room temperature and exhibits a temperature dependent built-in net spontaneous polarisation. The macroscopic measure of the built-in electric dipole moment, the spontaneous polarisation, is a decreasing function of the temperature, vanishing above the Curie temperature due to the consequent phase transition.

This rearranging or reorienting the spontaneous polarisation within a single-crystal material either throughout its volume or selectively within localised regions is referred to as repoling or sometimes just as poling as we shall call it from here on.

3.4 Poling Techniques

A wide array of treatments that involve heat, local chemical treatment and electrical manipulation have been employed for domain inversion in lithium niobate. A detailed understanding of the inversion mechanism in many of the techniques is not well understood as most of these techniques are empirical in nature and are employed with the sole aim of achieving the end result.

3.4.1 Poling as a result of a Heat Treatment

Elevating the crystal to temperatures close to the transitional Curie temperature during crystal-growth can mimic the simple conditions required for poling. However if periodic modulation is desired this bulk heat treatment will not produce the desired effect. Poling was reportedly accomplished below the Curie temperature by using an intense pulsed electric field that counteracted the internal crystal field. The field strength and the temperature being the two interdependent but key parameters to be considered at the time of poling (Ballman'72), a variation of the above technique used laser-generated thermal pulses instead of a localised pulsed field, in the presence of a steady state electric field on the –z face of a sample held at $400^0 C$ for domain inversion (Houe'95).

3.4.2 Chemically concurrent poling

Poling can be actually induced or affected by heat treatment of lithium niobate in the presence of certain chemicals, because of chemical changes at the exposed interface. Some researchers have exploited the fact that lithium niobate partially dissociates into a number of Li-Nb oxide phases at higher temperatures to induce domain inversion. Inversion occurs in the absence of a field and at temperatures somewhat lower that the Curie temperature in an un-metallized z-cut sample heated in a furnace for several hours either in air or in the presence of flowing Ar gas containing water vapour (essential to suppress the out-diffusion of Li_2O), and subsequently cooled down to room temperature at the rate of $50^0 C$ per minute. The thickness of the domain-

inverted laminar region is strongly dependent on the temperature, time and the atmosphere, increasing for treatment in air rather than in Ar and also with an increased heat-treatment-time and cooling-rate (Nakamura'87).

3.4.3 Poling due to Li_2O out-diffusion

Domain inversion has also been reported underneath the uncovered regions on the $+z$ face of a lithium niobate sample with a periodically patterned silicon oxide layer. Diffusion of Li from the lithium niobate substrate into the deposited silica film, subsequently lowering the Curie temperature was reported to be the cause of the induced domain inversion (Fujimura'91 & Yamamoto'91). A similar explanation describing the above technique was put forth by (Carruthers'71), who stated that the Li deficiency resulting from the preceding Li_2O out-diffusion institutes a change in the material composition at the surface, which in turn lowers the Curie temperature and affects the inversion. However the triangular-shaped shallow domains thus created, typically extend (Yamamoto'91) to depths of only ≈1.5μm and widths of ≈4.5μm, and subtend 30^0 angles with the surface, and are not quite what is desired for typical frequency conversion applications. Interestingly in (Webjorn'89a), a silicon dioxide cladding was employed to reportedly suppress the Li_2O out-diffusion below the covered areas of the periodically patterned + z face. The periodic variation of the composition of the surface layer produces a periodic domain inversion during the later cooling step. In this case too the boundaries between the inverted and the non-inverted regions tend to follow planes that make an angle of approximately 30^0 with the surface.

3.4.4 Surface Chemistry

A number of techniques regularly utilized in the fabrication of waveguides in lithium niobate have documented domain inversion as a result of changes in the inherent crystal field induced by chemical reactions or substitution of impurities.

Proton-exchange at lower temperatures followed by heat-treatment close to the Curie temperature is known to induce domain inversion on the +z face of lithium niobate (Nakamura'90) and on the –z face of lithium tantalate. Having inferred that heat-treatment of a Li deficient layer with a lowered Curie temperature can induce domain inversion within that layer, Nakamura'90, experimented with the proton-exchange

technique to produce the deficient layer. The exchange process replaces the Li^+ ions near the surface of lithium niobate with the H^+ supplied by the benzoic acid thereby yielding a Li deficient $H_xLi_{1-x}NbO_3$ layer (Jackel'82), which is then inverted during the following heat treatment. (Yamamoto'91) used pyrophosphoric acid as it provided higher proton content for replacing the Li content. Inverted domains with semi-circular profiles (Mizuuchi'91 & Ahlfeldt'91) extending to a depth of a few microns, resulting from the above treatment have been reported. Increased heat treatment time has shown to increase the inversion depths and so also an increased proton exchange time is known to reduce the threshold temperature for inversion (Nakamura'90 & Mizuuchi'91).

The Ti-indiffusion procedure routinely used for the fabrication of waveguides in lithium niobate was first reported by (Miyazawa'79), to trigger domain inversion only on its +z face. This occurrence was further confirmed by (Thaniyavaran'85). Domain inversion was reported within the diffused regions of the +z face covered with a patterned Ti film when in-diffusion was attempted for 5-10 hours at a temperature above 1020^oC (Miyazawa'79), with typical inversion depths of the order of $2-4\mu m$ being reported. Increased depths (Thaniyavaran'85) were reported resulting from an increased Ti film thickness and an increased diffusion time. The shape of the inverted domains is known to have a triangular profile making an angle of 30^0 with the surface (Lim'89 & Webjorn'89b & Ishigame'91 & Armani'92). A possible explanation for the inversion observed only on the +z face was presented by (Thaniyavaran'85), who suggested an increased Ti surface concentration on the +z face due to the lower diffusivity of that face. The change in concentration consequently lowers the Curie temperature, and with in-diffusion being performed at temperatures close to the Curie temperature it then increases the susceptibility of the material to domain inversion. (Miyazawa'86) attributes the domain inversion on the +z face to the spontaneous polarisation difference resulting from a concentration gradient of the indiffused Ti. The difference provides a surface electric field anti-parallel to the bulk spontaneous polarisation direction at the +z face. When the field becomes comparable to the internal field associated with the remaining bulk spontaneous polarisation (probably during the cooling-step), only the domain on the +z face is reversed.

The above said treatment of periodic *Ti*-indiffusion for domain inversion also produces a refractive index grating, which has the undesired effect of lowering the

efficiency of non-linear interactions as a result of diffraction and scattering effects (Ito'91).

Another technique employs thermal-oxidation of the deposited Ti-films for domain inversion. The thermal-oxidation at a temperature of $500^0 C$ of Ti-films deposited on the crystal face minimises the refractive index changes and inverts domains at the same time. The inverted domains appear on –z face, outside the patterned areas. The advantage of this method is that the inversion is affected at temperatures well below the Curie temperature (Yamamoto'92).

The photolithographically defined diffusion and ion exchange techniques result in periodic domains, which faithfully replicate the masks employed, however as the domains extend to a shallow layer below the surface, they are compatible with non-linear interactions in waveguide geometries only, and not for example with bulk frequency doubling experiments.

3.4.5 Czochralski crystal growth and Laser-heated pedestal growth techniques.

Periodic domain inversion utilising temperature fluctuations during crystal growth by the Czochralski method was studied by (Feng'80). Displacing the rotational axis from the symmetry axis of the temperature field induced the periodic domain fluctuations. In order to accentuate the growth striae produced the melt was doped with 1wt.% of yttrium. Crystals thus grown had a dopant distribution, which varied sinusoidally along the growth axis. When cooled through the Curie temperature, crystals having periodic laminar structures, with domain periodicities of 6.4μm were obtained.

Chromium-doped lithium niobate crystals with periodic domains appropriate for non-linear frequency mixing studies were later grown by modulating the bias current during the Czochralski crystal growth, by (Feisst'85). The concentration gradient of the non charge-compensated chromium impurities (resulting from the current modulation) was presumed to trigger the domain formation. Ferroelectric domains spatially correlated with the current-induced doping striations were observed. (Aleksandrovskii'92) further extended this approach by growing lithium niobate along the pseudocubic (0112) direction to obtain a flat interface.

The growth of domain inverted single fibres was reported by (Luh'86 & Luh'87). This was followed by the successful growth of $3\,\mu m$ spaced domains suited for frequency doubling to produce blue light, using the laser-heated-pedestal-growth

technique by (Magel'90). A further frequency doubling experiment for the generation of green light was reported by (Jundt'91), who also used the laser-heated-pedestal-growth technique to fabricate 1.24 mm long, single crystal fibres with a $250\,\mu m$ diameter and a domain spacing of $3.47\,\mu m$.

It should be noted that it is however difficult to achieve by the crystal-growth techniques uniform periodic domain-inversion over the desired centimetre length of the crystal, required for highly efficient non-linear interactions.

3.4.6 Electron beams and Electric fields

It can be understood from the previous discussion that a motion of the Li ions across the plane of oxygen atoms is required to invert the direction of the spontaneous polarisation. A model to describe poling below the Curie temperature has been proposed by (Haycock'86), who suggested the use of energetic/accelerated electrons in the presence of an applied electric field, to ionise the crystal and further initiate an open pathway for the motion of the Li ions through the oxygen planes. The local excitation of the oxygen ions by the fast electrons (ionising radiation) generates a transient vacancy in the oxygen plane resulting from the formation of a metastable molecular oxygen ion with a physical dimension much smaller than that of the separate oxygen ions. With the Li-ion being required to move by $\sim 0.05\,nm$ across the oxygen plane the meta stable state needs to exist for $\cong$ a pico-second, inversion is affected under the influence of the applied field. Lithium niobate and lithium tantalate crystals were poled at temperatures of $600^0 C$ and $400^0 C$ respectively, by irradiating them with energetic electrons in the presence of an electric field applied along the c-axis of the crystal.

Periodic domain inversion on the –z face by electron beam bombardment with the assistance of a static electric field and heat has also been reported by (Keys'90). Periodic domain reversal on the –z face of lithium niobate at room temperature and in the absence of an external field with use of an e-beam was first reported by (Yamada'91). The method yielded inversion depths of the order of hundreds of microns and under certain experimental conditions reaching all the way to the +z face of a 1mm thick crystal. The origin of the domain inversion in the electron injected region was thought to be a result of the local field generated by the injected electrons and the field of the charge-up electrons at the surface of the –z face. The domain

inversion, injected the electrons to much deeper locations, inducing further inversion as a result of the local field created by the electrons there (Yamada'91). Domain inversion hence occurs repeatedly at greater and greater depths because of the avalanche effect.

A significant breakthrough in domain inversion and control was demonstrated at the same time by (Ito'91,'92) who used electron beams from a scanning electron microscope to write domains in lithium niobate and lithium tantalate with periods of $7.5\,\mu m$.

However, the success of these researchers who experienced the limitations of slow writing speeds inspired (Yamada'93), to investigate domain inversion by direct application of an electric field with the help of metal electrodes deposited by conventional lithographic techniques on the surface of the crystal. Early work by (Camlibel'69), had shown that applied electric fields could be used to invert domains at fields of 300 kV/cm applied to lithium niobate and other oxide ferroelectric crystals, however dielectric breakdown and lack of domain control prevented the full technological impact of the technique at that time. A number of experiments conducted on electric field poling of lithium niobate by Evlanova, a decade later, have been reported by (Prokhorov'90), however the results were not suggestive of achieving the domain control required for device applications. The successful demonstration of this by (Yamada'93) re-opened the study of this promising approach. Control of domain inversion and the duty-cycle of the periodic structures proved to be relatively more difficult than expected and persistence coupled with an understanding and modelling of the electric field induced domain inversion process culminated in the success reported in the following papers in 1994. (Myers'94, Webjorn'94 and Burns'94).

The appropriate processing recipe for lithographically patterned room temperature electric field poling of lithium niobate, with use of metal-electrodes has been described in (Myers'95). A similar electric field poling technique, which utilizes photolithographic patterning of a photoresist layer to define a periodic-pattern, is descried in (Webjorn'94).

The technique of electric field poling has also been extended to affect poling in other materials of interest such as KTP (Chen'94) and $LiTaO_3$ (Zhu'95 & Mizuuchi'95).

The technique used in our experimental investigations was similar to that used by (Webjorn'94) and is described in the following paragraphs.

E-field repoling or simply E-field poling regularly applied for periodic domain inversion, refers to the process which allows the re-alignment of the spontaneous polarisation within a virgin single crystal ferroelectric like lithium niobate at room temperature under the influence of an externally applied electric field exceeding the coercive field, E_C. A subsequent electric field poling of the domain-inverted crystal has the effect of reversing the direction of the spontaneous polarisation within the inverted areas, restoring it to the original direction as in case of the virgin crystal. The two poling operations cycles the crystal between the two opposite polarisation states of $\pm P_s$ thus generating a hysteresis loop. On the basis of the hysteresis loop that existed in lithium tantalate, both lithium tantalate and its isomorphs were first discovered to be ferroelectric by (Matthias'49). The asymmetry in the hysteresis loop of lithium niobate suggests a preferred poling direction, for which it is easier to reverse the spontaneous polarisation. Beginning from a virgin crystal, the convention adopted refers to that direction for which the applied electric field reverses the spontaneous polarisation at a higher strength as the forward poling direction, while the opposite direction for which the strength of the applied electric field is less is termed the reverse direction (Chao'95).

A schematic representation of the poling process and the experimental set-up used to affect the poling of ferroelectric lithium niobate is shown in figure 3.2.

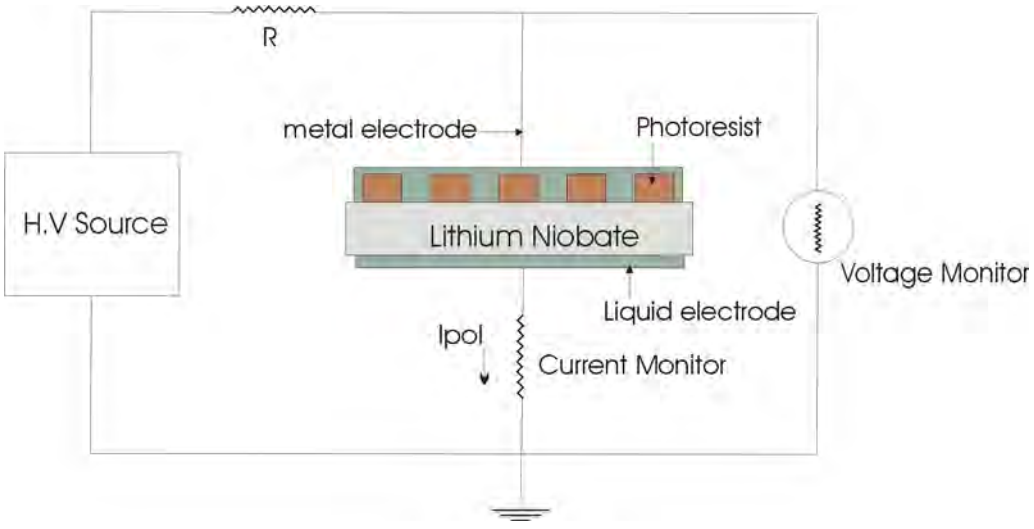

Figure 3.2 Schematic of the set-up used for electric field poling.

The reversal of the spontaneous polarisation is accompanied by a displacement of charge, which causes a transient current often referred to as the poling-current to flow in the poling circuit. The transient current is detected as a voltage-drop across a resistor. The high resistance (of the order of megohms) of the input resistor allows the control of the poling current. Periodic-poling is affected by the application of a high-voltage pulse through the current-limiting resistor across the sample with photo-lithographically defined periodic pattern on the –z face of the sample. Several researchers have chosen to photo-lithographically pattern the +z face of the sample as the domain nucleation process is thought to evolve at the patterned +z face and further extend towards the –z face (Yamada'93). We however have opted to pattern the photoresist on the –z face of lithium niobate as no significant difference (Webjorn'94) has been observed in the poling when either of the faces are patterned for poling. The –z faces of the samples which were to be poled are spin-coated with a positive photoresist with thickness of around 1μm, sufficient to serve as an electrical insulator to the applied field (Webjorn'94). A schematic describing the poling process leading to domain inversion is shown in figure 3.3.

The time varying poling current and the poling voltage are monitored and recorded during the poling process permitting both a qualitative and quantitative analysis of the poling procedure. Domain-inversion results in a current flow to compensate for the time-dependent change in the spontaneous polarisation P_S (=0.72μC/mm^2 for lithium niobate). A charge $Q=2P_S A$, where A corresponds to the area of the inverted domains is transported through the sample. The computer-controlled voltage supply is switched off as soon as the corresponding charge has been detected. The single most important parameter as reported by (Webjorn'94) which influenced poling is that the transferred charge should be twice the product of the spontaneous polarisation and the area.

The required contact between the electrodes and the periodically patterned sample is achieved with the use of conductive liquid gel (Webjorn'94), which is essentially an electrolytic solution of LiCl in water. The liquid electrolyte contact is used to ensure the application of a uniform field over the patterned area. The negative electrode is kept in contact with the patterned –z face whereas the positive electrode connected to a high-voltage supply allows the application of the high voltage pulse with a magnitude slightly higher than the corresponding coercive field of the crystal.

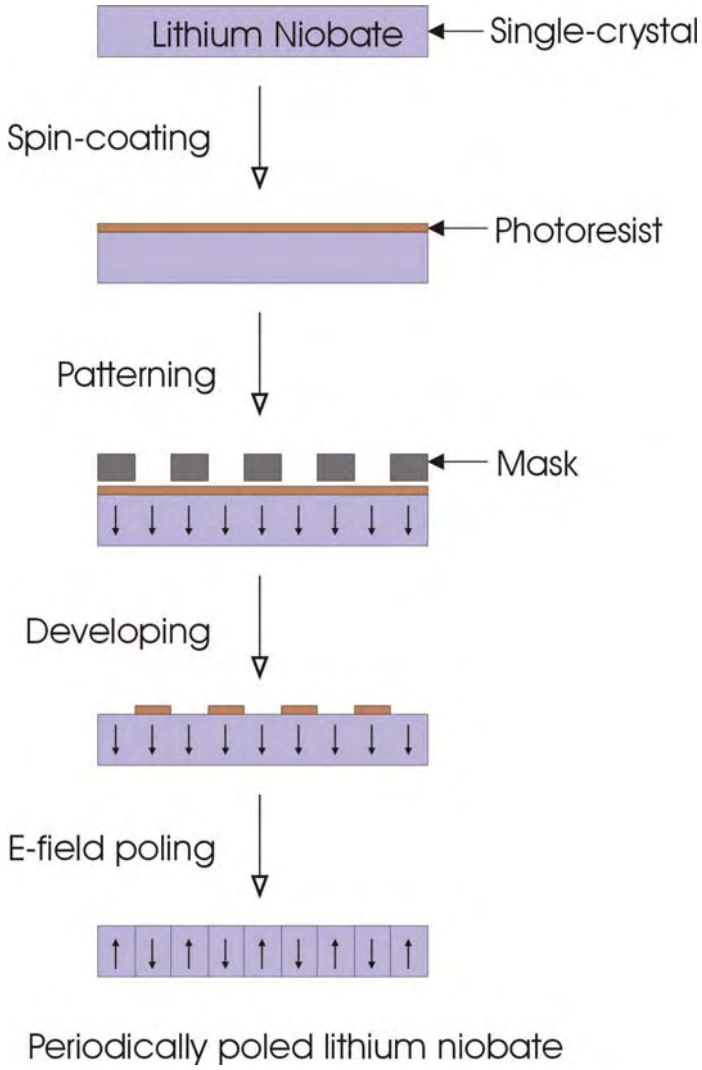

Figure 3.3 Schematic of the poling process

Initial poling trials attempted by several researchers adopted the technique of several poling pulses with varying time durations. The final domain structure as reported by (Webjorn'94) is not strongly influenced by the parameters of the poling pulses and poling by application of a single pulse had been reported by then. The inverted domains revert to their original orientation or domains can be reversed repeatedly if the field is applied for a duration less than 50 ms. However the inverted domains are permanent for fields applied for durations longer than 50 msec after the onset of poling (Byer'97).

Some typical traces of the measured current and voltage during poling are shown in chapter 5; with the area under the current curve representing the total charge, which in turn relates to the area poled.

The exact mechanism behind the formation and growth of domains with time, during the e-field switching is not well understood. Some attempts however have been directed to understand the domain dynamics and a brief summary of the conclusions drawn is described in chapter 5.

The room temperature electric field poling technique and a modified poling technique was used by us for the experiments reported in this thesis.

3.5 Summary

This chapter introduced certain basic concepts such as Curie temperature, spontaneous polarisation and domains for ferroelectrics like lithium niobate and subsequently introduced the idea of ferroelectric domain inversion or poling of lithium niobate. The idea of poling was further explained at length from the crystal structure viewpoint. Several techniques that have been employed to achieve domain inversion in lithium niobate such as Czochralski / laser-heated-pedestal-crystal growth, heat treatment, chemical treatment, Li_2O out-diffusion, Ti-indiffusion and e-beams were briefly reviewed and detailed explanation of the most commonly used technique of room temperature electric field induced domain inversion was presented.

3.6 References

Abrahams S.C, Hamilton W.C, Reddy J.M, *J. Phys. Chem. Solids*, **27**, 1013, 1966.

Ahlfeldt H, Webjorn J, Arvidsson G, *IEEE Photon. Technol. Lett*, **3(7)**, 638, 1991

Aleksandrovskii A.L, Naumova I.I, Tarasenko V.V, *International Symposium on Domain Structures of Ferroelectrics and related materials*, 7-10 July, 1992.

Armani F, Delacourt D, Lallier E, Papuchon M, He Q, Micheli M.De, Ostrowsky D.B, *Electron. Lett*, **28(2)**, 139, 1992.

Ballman A.A, Brown H, *Ferroelectrics*, **4**, 189, 1972.

Burns W.K, McElhanon W, Goldberg L, *IEEE Photon. Technol. Lett*, **6(2)**, 252, 1994.

Byer R.L, J. Nonlinear. *Opt. Phys. Mater*, **6(4)**, 549, 1997.

Camlibel I, *J. Appl. Phys*, **40**, 1692, 1969.

Carruthers J.R, *J. Appl. Phys*, **42**, 1846, 1971.

Chao S, Davis W, Tuschel D.D, Nichols R, Gupta M.C, Cheng H.C, *Appl. Phys. Lett*, **67**, 1066, 1995.

Chen Q, Risk W.P, *Electron. Lett*, **30(18)**, 1516, 1994.

Fatuzzo E, *Phys. Rev*, **127**, 1999, 1962.

Feisst A, Koidl P, *Appl. Phys. Lett*, **47(11)**, 1125, 1985.

Feng D, Meng N.B, Hong J.F, Yang Y.S, Yang Z.Z, Wang Y.N, *Appl. Phys. Lett*, **37(7)**, 607, 1980.

Fujimura M, Suhara T, Nishihara H, *Electron. Lett*, **27(13)**, 1207, 1991.

Haycock P.W, Townsend P.D, *Appl. Phys. Lett*, **48(11)**, 698, 1986

Houe M, Townsend P.D, *Appl. Phys. Lett*, **66**(20), 2667, 1995.

Ishigame Y, Suhara T, Nishihara H, *Opt. Lett*, **16(6)**, 375, 1991.

Ito H, *Review of Laser Engineering*, **20**, 236, 1992.

Ito H, Takyu C, Inaba H, *Electron. Lett*, **27(14)**, 1221, 1991.

Jackel J.L, Rice C.E, Veselka J.J, *Appl. Phys. Lett*, **41(7)**, 607, 1982.

Jundt D.H, Magel G.A, Fejer M.M, Byer R.L, *Appl. Phys. Lett*, **59(21)**, 2657, 1991.

Keys R.W, Loni A, Rue R.M.De.La, Ironside C.N, Marsh J.H, *Electron.Lett*, **26(3)**, 188, 1990.

Lim E.J, Fejer M.M, Byer R.L, Kozlovsky W.J, *Electron. Lett*, **25(11)**, 731, 1989.

Lines M.E, Glass A.M, '*Principles and Applications of Ferroelectrics and related materials* ', Clarendon Press, 1977.

Luh Y.S, Feigelson R.S, Fejer M.M, Byer R.L, *J. Crystal Growth*, **78(1)**, 135, 1986.

Luh Y.S, Fejer M.M, Byer R.L, Feigelson R.S, *J.Crystal Growth*, **85(1-2)**, 264, 1987.

Magel G.A, Fejer M.M., Byer R.L, *Appl. Phys. Lett*, **56(2)**, 108, 1990.

Matthias B.T, Remeika J.P, *Phys. Rev*, **76(12)**, 1886, 1949.

Miyazawa S, *Appl. Phys. Lett*, **48(16)**, 1105, 1986.

Miyazawa S, *J. Appl. Phys*, **50**(7), 4599, 1979.

Mizuuchi K, Yamamoto K, *Appl. Phys. Lett*, **66(22)**, 2943, 1995.

Mizuuchi K, Yamamoto K, Taniuchi T, *Appl. Phys. Letts*, **58(24)**, 2732, 1991.

Myers L.E, Eckardt R.C, Fejer M.M, Byer R.L, Bosenberg W.R, Pierce J.W, *J. Opt. Soc. Am B*, **12(11)**, 2102, 1995.

Myers L.E, Miller G.D, Bortz M.L, Eckardt R.C, Fejer M.M, Byer R.L, *IEEE Conference on Non-linear Optics: Material, Fundamental, and Applications*, 25-29th July, 1994.

Nakamura K, Ando H, Shimizu H, *Appl. Phys. Letts*, **50(20)**, 1413, 1987.

Nakamura K, Shimizu H, *Appl. Phys. Lett*, **56(16)**, 1535, 1990.

Prokhorov A.M, Kuzmonov Yu. S, '*Physics and chemistry of crystalline Lithium Niobate'*, Adam Hilger, Bristol, 1990.

Thaniyavaran S, Findalky T, Booher D, Moen J, *Appl. Phys. Lett*, **46(10)**, 933, 1985.

Webjorn J, Laurell F, Arvidsson G, *IEEE Photon. Technol. Lett*, **1(10)**, 316, 1989a.

Webjorn J, Laurell F, Arvidsson G, *J. Lightwave Technol*, **7(10)**, 1597-1600, 1989b.

Webjorn J, Pruneri V, Russell P.St, Barr J.R.M, Hanna D.C, *Electron. Lett*, **30(11)**, 894, 1994.

Yamada M, Kishima K, *Electron. Lett*, **27(10)**, 828, 1991.

Yamada M, Nada N, Saitoh M, Watanabe K, *Appl. Phys. Letts*, **62(5)**, 435, 1993.

Yamamoto K, Mizuuchi K, *IEEE Photon. Technol. Lett*, **4(5)**, 435, 1992.

Yamamoto K, Mizuuchi K, Takeshige K, Sasi Y, Taniuchi T, *J. Appl. Phys*, **70(4)**, 1947, 1991.

Zaky A. A., Hawely R., *Dielectric Solids*, Routledge & Kegan Paul Ltd, London, 1970

Zhu S, Zhu Y, Zhang Z, Shu H, Wang H, Hong J, Ge C, *J. Appl. Phys*, **77(10)**, 5481, 1995.

Chapter 4
Domain visualisation and Wet etching

4.1 Introduction and chapter layout

Quasi-phase-matched non-linear frequency conversion, using ferroelectric lithium niobate with periodically modulated domains allows efficient frequency conversion of laser radiation into the visible spectrum and its versatility continues to attract the attention of the scientific community. The desired high conversion efficiency of the non-linear interaction however depends primarily on the uniformity of the periodically domain inverted structure of the ferroelectric used.

While electric field induced periodic domain inversion is now a fairly mature technique, considerable research focus is still directed to understanding the mechanism underlying the nucleation and growth of domains in ferroelectrics. The uniform periodic structures required for the non-linear processes can be fabricated regularly with high precision if the mechanism behind the formation and motion of the domain walls during periodic poling can be fully understood. Several techniques with the prime intention of visualising and studying the formation and growth of anti-parallel domains, and also assess the quality of the poled structures have been used to date.

This chapter begins by briefly discussing some domain visualisation techniques used to assess the quality of domain inversion. The following section discusses the wet or chemical etching route to domain visualisation at some length, as the application of such a technique could also be used for micro-structuring lithium niobate. The following section describes some experimental investigations conducted to ascertain whether the ‘widely used’ etchant mixture of ‘hydrofluoric and nitric acid in the ratio of 1:2’, is indeed the ideal one. A reaction formulation explaining the differential etch mechanism is proposed. The concluding section focuses on further experiments, which revealed a latent etch mechanism in lithium niobate, as evidenced by some Raman studies.

4.2 Review of Domain Visualisation techniques

Several techniques have been developed to date with the prime aim of understanding the mechanism that governs the formation and the growth of domains and domain

walls in ferroelectrics. A range of (contact and non contact) microscopy techniques such as second harmonic generation imaging/second harmonic generation microscopy, electrostatic force microscopy, near-field scanning optical microscopy, apertureless near-field scanning optical microscopy (Orlik'00), scanning non-linear dielectric microscopy and atomic force microscopy (Wittborn'02 & Tyunina'99) have been reported in the literature with varying degrees of spatial resolution. A few other techniques such as in-situ visualisation, piezoelectric measurement (Laurell'92), pyroelectric measurement, toning (Laurell'92) and the destructive wet/chemical etching, have also been used to reveal domain structures in ferroelectrics. A conventional polarising optical microscope, which utilizes the (second rank tensor) electrical permittivity / refractive index for imaging is one of the simplest ways of visualizing domain features in ferroelectrics and is often the preliminary investigative step in the visualization procedure.

The non-linear second harmonic generation microscopy technique proposed and used by (Uesu'95 and Kurimura'97), utilizes the change in the sign of the third rank non-linear susceptibility tensor, d_{ijk}, of the imaged periodic anti-parallel ferroelectric domains in $LiTaO_3$ and $LiNbO_3$, to produce the desired image contrast. The non-linear microscope exploits the second harmonic wave phase reversal accompanying the inversion of the spontaneous polarisation between the anti-parallel domains for visualisation, with the interference between the second harmonic waves converting the phase information into a second harmonic (image) contrast. A point-detection technique reported by (Laurell'92) used reflection second harmonic generation to confirm polarisation reversal induced by an ion exchange treatment of KTP. Domain walls in periodically poled KTP and lithium niobate have also been observed by (Bozhevolnyi'98), using second harmonic generation microscopy, with the second harmonic generation enhancement in the transition region between neighbouring domains being exploited for imaging.

The use of electrostatic force microscopy to map domain structures and domain walls in ferroelectrics has been reported by (Saurenbach'90 & Luthi'93). Domain walls were imaged under non-contact operational mode, whereas information about the domain wall structure and information about the polarity of the domains was obtained in the contact-imaging mode of the scanning force microscope used by (Luthi'93). The observed electrostatic contrast in the imaged domain inverted grating in lithium niobate is explained by the interaction between a permanent negative charge present

on the scanning tip and the electric field above the scanned surface; with the magnitude and the distribution of the field being determined by the shape of the domain inverted region (Bluhm'97).

The near-field scanning optical microscopy technique used by (Yang'97) employed a polarisation and phase sensitive near-field scanning optical microscope to image ferroelectric domain walls. A direct observation of the pinning and bowing effect of a 180^0 domain wall under the influence of a uniformly applied electric field has also been reported with use of a collection-mode near-field scanning optical microscope (Yang'99). The strain, resulting from vacancies or distortion of the *O-H* bonds induces a birefringence at the 180^0 domain walls (Gopalan'96) through the photoelastic effect (Narshimamurty'81). The birefringence induced polarisation reversal and phase change of the transmitted light as the near-field scanning optical microscope tip is scanned over the domain wall is used to form the image.

A purely electrical method referred to as scanning non-linear dielectric microscopy, proposed by (Cho'96) for imaging ferroelectric domains, involved the point-to-point measurement of the variation in the non-linear dielectric constant of the specimen. The technique was used to image the third order (non-linear) dielectric constant (which unlike the second order linear dielectric constant is sensitive to spontaneous polarisation reversal and changes sign with inversion of the spontaneous polarisation) profiles of an yttrium doped lithium niobate sample with periodic domains by (Gao'98), with 3μm resolution. A sub-micron imaging resolution has been reported by (Cho'99).

An in-situ visualisation technique aimed at observing the nucleation and growth of domains (Shur'00,'01,'02) and further control the undesired spreading of domains during electric field poling for periodic structures was put forth by (Missey'00), via the scattering exhibited by the periodic structures when observed through cross polarizers being used for the real time study.

The stable charged domain walls that evolve during the electric field switching of lithium niobate further produce an electric field which induces a local variation in the refractive index through the electro-optic effect (Gopalan'99a) consequently allowing the visualisation of the dynamic domain patterns during switching and that of static ones after turning off the applied field. The (Gopalan'99b) technique of electro-optic

microscopy has been used for real time observation of 180^0 domain kinetics in lithium tantalate and lithium niobate.

The optical birefringence exhibited by 180^0 domain walls in congruent lithium niobate even in the absence of an external electric field is related to the internal field (Gopalan'97) in the crystal and also associated with the Li non-stoichiometry (Gopalan'98), can be employed to image domains between cross-polarizers.

4.3 Wet / Chemical Etching

A destructive diagnostic technique, referred to as wet or chemical etching, is frequently employed to reveal domains in ferroelectrics and takes advantage of the different rates of interaction between a chemical-etchant and the different crystal surfaces/ planes. The varying etch-rates/reaction-rates have the effect of revealing some surfaces/planes (with lower etch-rates) compared with planes with higher etch-rates. The preferential etching has the effect of creating distinguishable variation in the topography of the etched surface, which can then subsequently be easily viewed with conventional imaging microscopes. The etching of periodically poled quasi-phase-matching crystals using different acids/alkalis or other chemical-mixtures has the undesired effect of frosting the chemically-attacked surface, consequently rendering the crystal unsuitable for further non-linear frequency experiments as the surface irregularities lead to high losses resulting from scattering at the etched surface. However, differential etching by acid mixtures is an effective tool regularly adopted to characterise anti-parallel periodic domain structures (oriented along the z-axis) in ferroelectric lithium niobate as the etchant has a preference of reacting only with the –z face of the crystal and leaving the +z face untouched. This consequently leaves periodic relief-structures on the etched face of the crystal.

Various reagents were examined by (Nassau'66), to gauge their ability to etch or polish lithium niobate crystals, between room temperatures and $100\,^0C$ include

- Hydrofluoric acid (*HF*), nitric acid (HNO_3), sulphuric acid (H_2SO_4), ammonium hydroxide (NH_4OH), lithium chloride (*LiCl*), phosphoric acid (H_3PO_4), acqua regia, chromic acid and combinations thereof.

And from $100\,^0C$ to $400\,^0C$ include

- Potassium hydroxide (*KOH*), potassium dichromate ($K_2Cr_2O_7$), potassium permanganate ($KMnO_4$), potassium fluoride (*KF*), potassium bromide (*KBr*),

lithium chloride, potassium sulfate (K_2SO_4), lithium sulfate (Li_2SO_4), sodium sulfate (Na_2SO_4), potassium nitrate (KNO_3), sodium borate ($NaBO_2$), sodium tartarate ($Na_2C_4H_4O_6.2H_2O$), potassium pyrosulfate ($K_2S_2O_7$), sodium tungstate (Na_2WO_4) and combinations thereof.

It was also observed that adjacent domains on *c*-axis surfaces appeared slightly darker than the other on a *15 sec to 60 sec* immersion in *molten potassium hydroxide*.

A similar effect was also observed when lithium niobate was treated for *15 minutes* at 50^0C with a mixture of two parts of *30% hydrogen peroxide* (H_2O_2) and one part of *30% sodium hydroxide (NaOH*), which had the ability to differentiate between the two faces.

However the best polishing and etching effect was observed when a mixture of *one part of HF acid and two parts of* HNO_3 *acid* was used (Nassau'66). All the subsequent work carried out by these authors and many subsequent researchers has employed this etchant, and has further prompted other researchers to take a lead from this result and use this specific etchant mixture.

The etch-rate and the appearance of the etch-pits (proposed to reveal the point of intersection of dislocations with the etched surface) on the etched-face were found to be strongly dependent on the orientation and the polarity of the domains along *z*-axis. As the orientation is varied away from the *z*-faces, the etch-rates were found to approach each other, until in directions perpendicular to the *z*-axis where both of the positive and negative domains was reported to etch at the same rate (Nassau'66). The shape of the pits revealed on the etched planes was found to depend on that crystal plane, with prolonged etching changing only the size of the etched-pits but not their density.

The use of a polishing technique to reveal domain structures in lithium niobate crystals by exploiting the slight difference in hardness across a domain boundary is also reported (Nassau'66). Lithium niobate crystals ground and polished with Linde A (0.3μm alumina) and Linde B (0.05μm alumina) on Buehler AB microcloth revealed domain structures, which were visualised by a reflection-mode microscopic examination. Pruneri'95 reports a similar effect that accounts for the difference in the etch-rates of the up and down domains, oriented along the z-axis when polished by Syton.

Several etchants were experimented with to configure the best option by Evlanova have been documented by (Prokhorov'90). Some of the reactants tested were:

- *KOH melt* at 400^0C for 15 to 60 seconds
- Mixture of 2 parts of 30% H_2O_2 and 1part of *NaOH* at 100^0C for 15 minutes
- Solution of KHF_2 in concentrated HNO_3 at 100^0C for 5 minutes
- Mixture of 1 part of *HF* and 2 parts of HNO_3 at their boiling point of 110^0C for 10 minutes.

The last option was found to be the best as it revealed domains not only on surfaces normal to but also domains on surfaces parallel to the polar axis of the crystal (Prokhorov'90).

Hot etching was employed for studying domain structures of larger specimens with thickness of more than 2 mm and crystal boules; however brittle specimen samples were etched at room temperatures to reveal the domains. Some of the etchants used in this case were:

- Mixture of *HF* and HNO_3; *HF* with an *admixture* of $KMNO_4$
- Mixture of *HF* with *caustic potash*.

The best results in terms of differentiating the domains were obtained when a mixture of *HF* and HNO_3 was used in the ratio of *1:4* with an etching time of 20 hours. It was observed that the surfaces concerned had to be well polished to obtain the desired results (Prokhorov'90). Later on several researchers have also resorted to the use a pure HF solution to etch periodically poled lithium niobate.

The chemical-etching technique though destructive in nature was further investigated by us with the aim of micro-structuring lithium niobate for useful applications in micro-electromechanical (MEMS) or micro-opto-electromechanical systems (MOEMS). Additionally as all previous surveyed research literature does not dwell on the reasons for the use of the 'always-used', *specific 1:2* $HF:HNO_3$ etchant ratio for domain investigations in lithium niobate, some experiments were directed to investigate what affect other etchant-ratios would have on the etched negative z-faces.

The next section explains some experiments performed to ascertain the fact that the *always-used* etchant ratio of $HF:HNO_3$ is in fact not the most ideal one. An explanation of the etching-mechanism is also proposed and explained in the following section.

4.4 Introduction to the Etching Studies

As described in the previous section insufficient reasoning behind the extensive use of the etchant mixture of hydrofluoric acid and nitric acid in the ratio of 1:2, prompted the following investigation of experimenting with different ratios of the same etchants. Also, as will be described in the following chapter, the difficulty encountered in etching samples bonded by various adhesives (instead of the finally adopted direct-bonding technique), prompted us to try some etching experiments using mixtures having different volumetric ratios of hydrofluoric acid and nitric acid, instead of the mixture having the two acids in the conventional ratio of 1: 2 respectively. We also performed some etching experiments with mixtures of hydrofluoric acid and water, again having the two in different volumetric proportions, to get a detailed picture of the roles played by the three different constituents of the etch mixture, in the etching mechanism. Etching studies with mixtures of nitric acid and water in different amounts in the mixture was not considered as it was known that nitric acid in itself was incapable of etching, a fact that was confirmed by an experiment conducted to etch with just nitric acid.

This etching technique has also been employed to reveal discontinuities in the crystal, along which the etching is known to proceed at a much faster rate. As our prime goal here was to fabricate structures of *nm* to μm dimensions in single crystal lithium niobate using the wet etching technique, it was necessary to try and understand the mechanism involved. This domain sensitive structuring of lithium niobate is quite unlike silicon microstructuring, where anisotropic etching is the most common route to microstructuring. Selective etching and / or sacrificial etching with appropriate etch stops to carve out the structural material has been a widely researched and established route to microstructuring for MEMS.

We have performed a parametric study of the etch rates and the etch quality as a function of the specific ratios of the two constituents to conclude that the ratio of 1:2, is in fact not quite the best in achieving the largest differential etch rate (Sones'02). We also discovered the presence of a second differential etch behaviour, between the virgin and recently re-poled faces.

4.4.1 Experimental Set Up and Procedure

All the lithium niobate samples used for the experiments were provided by Crystal Technology, USA, and were optically polished z-cut circular single crystal wafers having a diameter of 76.2 mm and a thickness of 500μm. The samples were diced in house to the required size of 15 mm x 30 mm and then cleaned using the regular multiple solvent cleaning procedure (described in Appendix A) in clean room environment preparing them for the subsequent photolithography stage. The –z face of the cleaned samples were spin-coated with a Shipley 1813 photoresist of a thickness of ~1μm, achieved with spinning speed of 5500 rpm. A rectangular pattern of 6 mm x 20 mm was then photolithographically imposed in the photoresist using a Karl Suss mask aligner with an exposure time of 10sec at intensities of ~8 mW/cm^2 at an exposure wavelength of 365nm. The rectangular patterned area of the single crystal sample was then reversed with the conventional domain engineering technique of electric field poling by application of an electric field exceeding the intrinsic coercive field of 22 kV/mm. The domain inverted samples were then diced in four separate pieces, each of dimension 6mm x 5mm for the following etching-study. The intentional selection of *different* regions of the *same* sample for the subsequent etching-study would necessarily ensure as much uniformity as possible in both the source material, and the associated preparatory processes of photolithography and poling.

Each of the poled samples was then etched in mixtures of hydrofluoric acid and nitric acid with different volumetric ratios of the constituent acids. The volumetric ratios selected were such that the most commonly used ratio of 1: 2 was within the interval of the selected values, in turn allowing a comparative study of the various results obtained with different ratios. The chosen ratios were 1: 0, 1: 1, 1: 2 and 1: 4, with the first and second numbers in the ratios indicating the proportion of hydrofluoric acid and nitric acid respectively in the etchant-mixture. The hydrofluoric acid and nitric acid solutions used were 48 % and 78 % weight by volume solutions in water. All the chemicals used were of electronic grade, and were provided by Fischer Scientifics, U.K. The samples were then etched for a specified period of 15 hours at a sustained temperature of 60^0 C**.**

A second etching study was done using diluted mixtures of 48 % hydrofluoric acid in water, with ratios identical to those in the previous case i.e. 1:0, 1:1, 1:2 and 1:4, with

the first and second figures in the ratio indicating the amount of 48% hydrofluoric acid and water in the mixture. The etching time and temperature too were the same as used in the first study.

All the etching was carried out within a PTFE container, kept on an integral hot plate with a magnetic stirrer, which stirred the etchant and ensured uniform etching of the sample faces. After etching the samples were thoroughly cleaned with deionised water and blown dry by N_2. Both the sample faces were then studied using a Tencor Alpha step surface profilometer to determine the etch depths. A set of ten different readings was taken for each depth measurement on the two faces, to average out any error relative to the lack of smoothness of the etched areas. A scanning electron microscope was also used to examine the overall surface topography.

4.4.2 Measurements and Analysis

A schematic explaining the poling and etching geometry common to both the etching-studies is shown in figure 4.1, with the etch-depth measurements on the two different z-faces depicted in figure 4.1c.

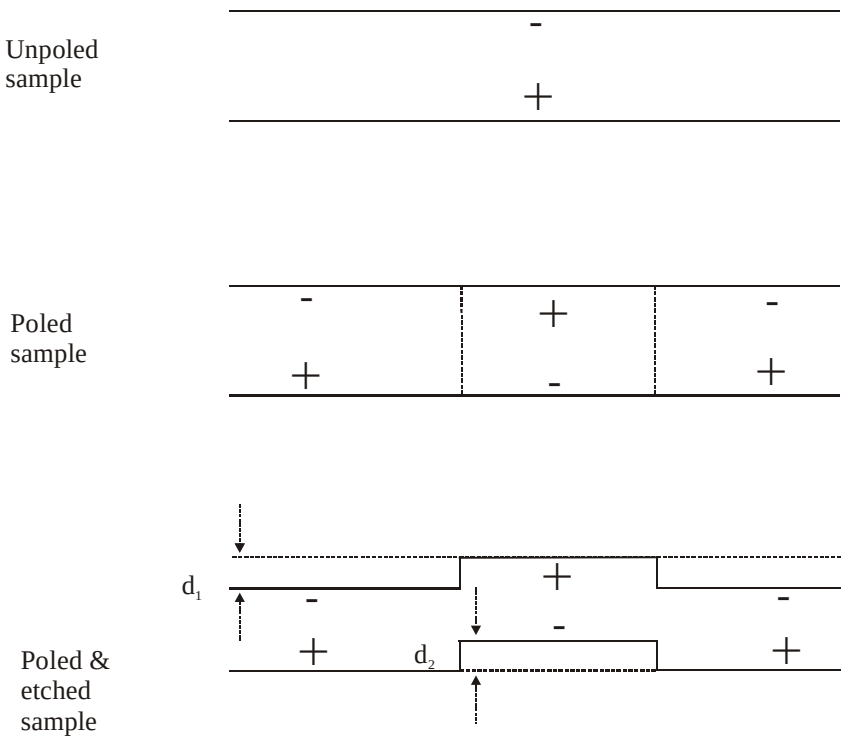

Figure 4.1 Schematic showing the resulting features on the +z and –z faces after spatially selective poling (b) and etching (c).

An extremely large difference is observed (Barry'98) to exist between the etch rates for the +z and –z faces of lithium niobate; with the –z face etching at an average room temperature etch-rate of ~0.8 μm per hour, and the +z face remaining virtually unetched even after a prolonged exposure of 600 hours to the acid mixture of HF/HNO_3 in the ratio of 1:2. As seen in figure 4.1, starting from a virgin sample, domain inversion of the central region and subsequent etching with the acid etchants produce on one face an island of +z in the background of –z and a complementary –z island in the background of +z. The two etch depths were labelled d_1 and d_2 respectively. A tabular representation, of the Alpha-step measurements of d_1 and d_2 on both faces, for the two etching-studies with mixtures of HF/HNO_S and HF/H_2O, are shown in table 4.1 and 4.2 respectively.

The collected data allows comparison of the etch rates for the –z and +z faces, and also between the virgin –z face and the newly poled –z face and is suggestive of the existence of a second differential etch rate between the newly poled and the virgin –z faces. Earlier reported works on the polarisation hysteresis and reduction of the coercive field for back-poling compared to forward poling (Chao'95, Brown'99 and Gopalan'97), offer some reason to suppose that the two etch rates may differ. Hence two possible differential etch rates may be involved in the etching studies, namely that between the +z and –z faces and that between the virgin –z and the newly poled –z faces with the differential etch rate between the latter described by an effective contrast ratio, c defined as a normalised quantity:

$c = (d_1 – d_{2)} / (d_1 + d_2)$

Table 4.1 Data for the study with HF and HNO_3

Ratio of HF: HNO3	Percentage of HF in the etchant mixture	Etch depth measurement on the –z face (with a poled +ve region) d_1 in μm	Etch depth measurement on the +z face (with a poled –ve region) d_2 in μm
0:1	0%	0	0
1:4	9.6%	26.19 ± 0.74	22.90 ± 0.64
1:2	16%	48.30 ± 2.40	43.30 ± 1.61
1:1	24%	70 ± 1.81	64.80 ± 1.74
1:0	48%	81.90 ± 1.97	83.80 ± 1.63

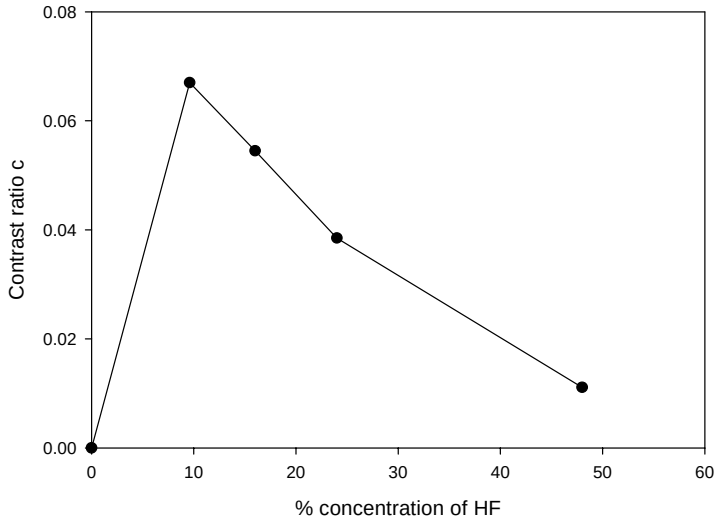

Figure 4.2 Plot showing variation of the contrast ratio 'c' with concentration of HF.

The plot in figure 4.2, showing a variation in the contrast ratio 'c' with the concentration of HF for the set of data shown in table 4.1, suggests that the second differential etch between the virgin and newly poled -z faces would be more conclusive/pronounced for (a lower) 9.6 % concentration of HF.

Table 4.2 Data for the study with HF and water

Ratio of HF: water	Percentage of HF in the etchant mixture	Etch depth measurement on the –z face (with a poled +ve region) d_1 in μm	Etch depth measurement on the +z face (with a poled –ve region) d_2 in μm
1:4	9.6%	1.59 ± 0.37	1.38 ± 0.17
1:2	16%	3.50 ± 0.20	2.5 ± 0.22
1:1	24%	6.75 ± 0.35	5 ± 0.28
2:1	32%	22.54 ± 2.13	20.47 ± 1.60
1:0	48%	81.90 ± 1.97	83.80 ± 1.63

The corresponding plots of the measured etch depth d_1 and d_2 on the opposite z faces versus the percentage of HF in the etchant mixtures of HF/HNO_3 (used for the first study) and HF/H_2O (used for the second study) are as shown in the figures 4.3 and 4.4.

Two sets of data points for the depths $d_1$and d_2 described via figure 4.1 are included in the plots and the error bars for each data point represents the standard deviation deduced for each set of ten depth measurements done with the surface profilometer.

The numbers in brackets on the plots represent the ratios of the constituent acids in the etchant mixtures used for the two studies.

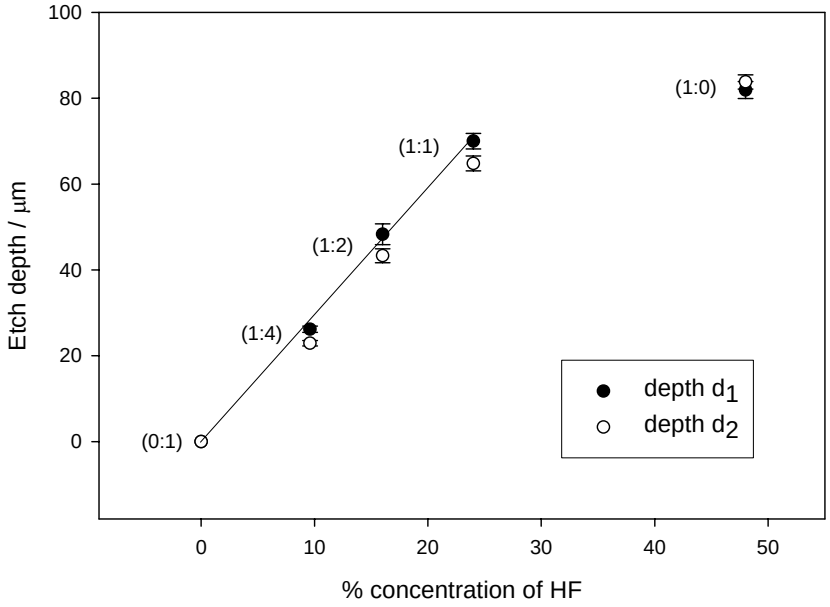

Figure 4.3 Plot of the measured etch depths d_1 and d_2 for samples etched in mixtures of HF/HNO_3 for 15 hours at a temperature of 60^0C. The straight line is the best fit for the first four data points

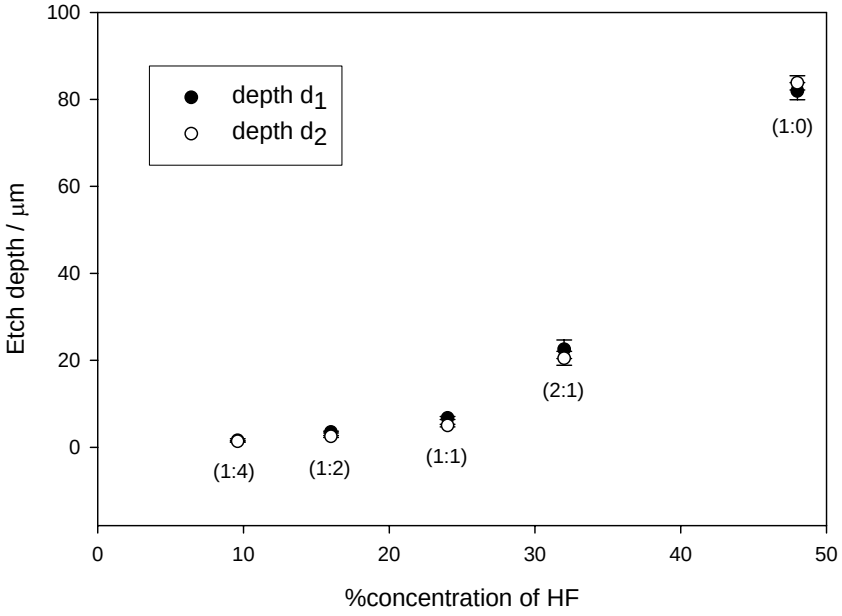

Figure 4.4 Plot of the measured etch depths d_1 and d_2 for samples etched in mixtures of HF/H_2O for 15 hours at a temperature of 60^0C

It can be easily inferred that the generally used 1:2 etch mixture of HF/HNO_3 etches approximately at half the rate as the pure HF etchant solution with no HNO_3, and labelled (1:0) in the plots. In contrast as expected the pure HNO_3 etchant solution with no HF, and labelled (0:1) in the plots, produces no observable etching. The collected information for the etch depths also suggests the existence of a second differential etch rate quantified by the contrast ratio c, and could be of help in the lithium niobate MEMS work described in chapter 6, where precise control of the etching rates and back-etching is highly desirable for sculpting the desired free standing structure in the bulk of the lithium niobate substrates.

The plot of the etch depth measurements d_1 and d_2 for the second etching study with diluted mixtures of 48% HF plotted as a function of the percentage of HF, shows a rapid increase for concentrations between ~ 20% - 30%, and is also suggestive to a lesser extent of the second differential etch rate.

The SEM micrographs shown in figure 4.5, of the samples etched in mixtures with different volumetric ratios of HF and HNO_3, indicate a distinct difference in the etch depths achieved and the surface roughness of the etched –z face. What is immediately evident is that the widely employed ratio of 1:2, neither yields the optimum etch rate nor the best smoothness of the etched –z face. In fact the pure HF solution (no HNO_3) produces the best results.

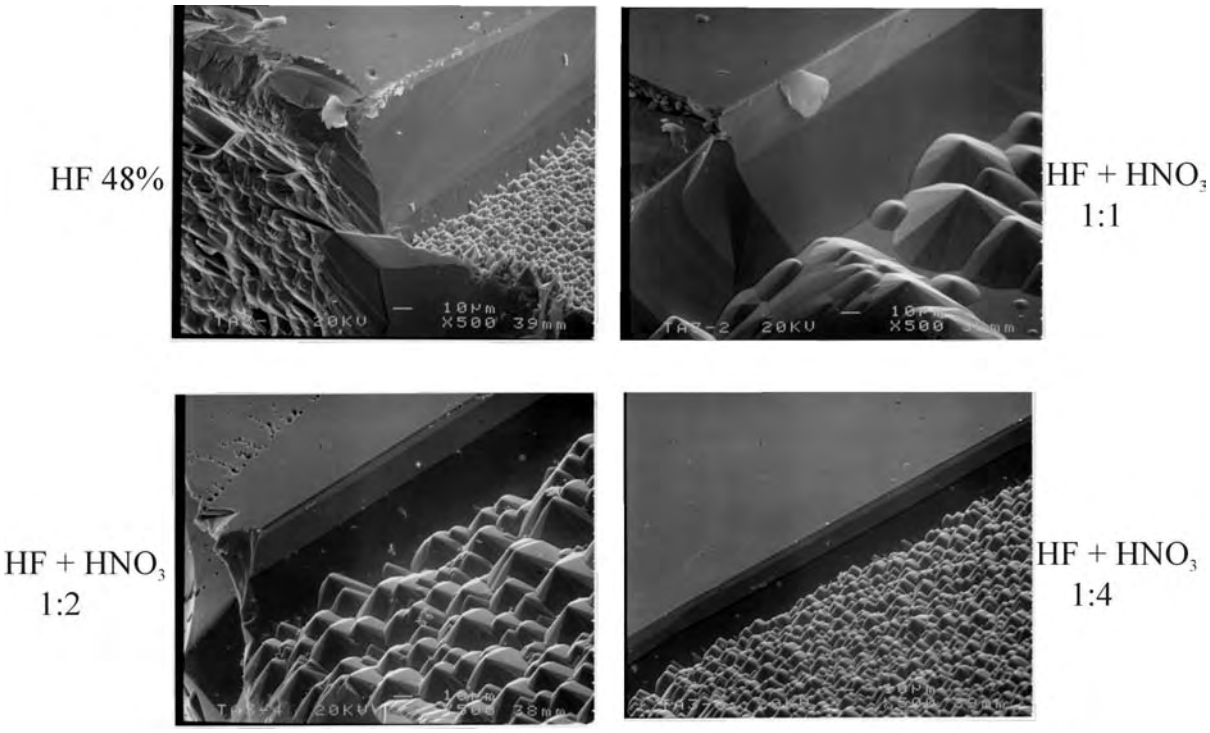

Figure 4.5 SEM image showing the unetched +z faces and the etched –z faces for the four samples showing the visible difference in height and surface morphology of the etched –z faces.

The SEM images of the etched sample faces of figure 4.5 show a walled feature separating the unetched +z regions from the etched –z regions with structures having a three fold symmetry. As the side faces of these peaks that are neither +z or –z faces etch at rate different from the –z face the roughness once established by the etching process is maintained throughout the process.

The plan views seen in figure 4.5 of the same etched regions make the comparison of the smoothness of the etched surfaces more apparent.

It can be conclusively inferred from the SEM images of the etched faces shown in figures 4.5 and 4.6 that the widely used etchant HF/HNO_3 with a constituent ratio of 1:2, is neither optimal in the etch depths achieved, nor in the smoothness obtained for the etched –z faces. The best results for the etch depths and the etch smoothness at the used temperature of 60^0C is instead achieved with the pure HF acid solution.

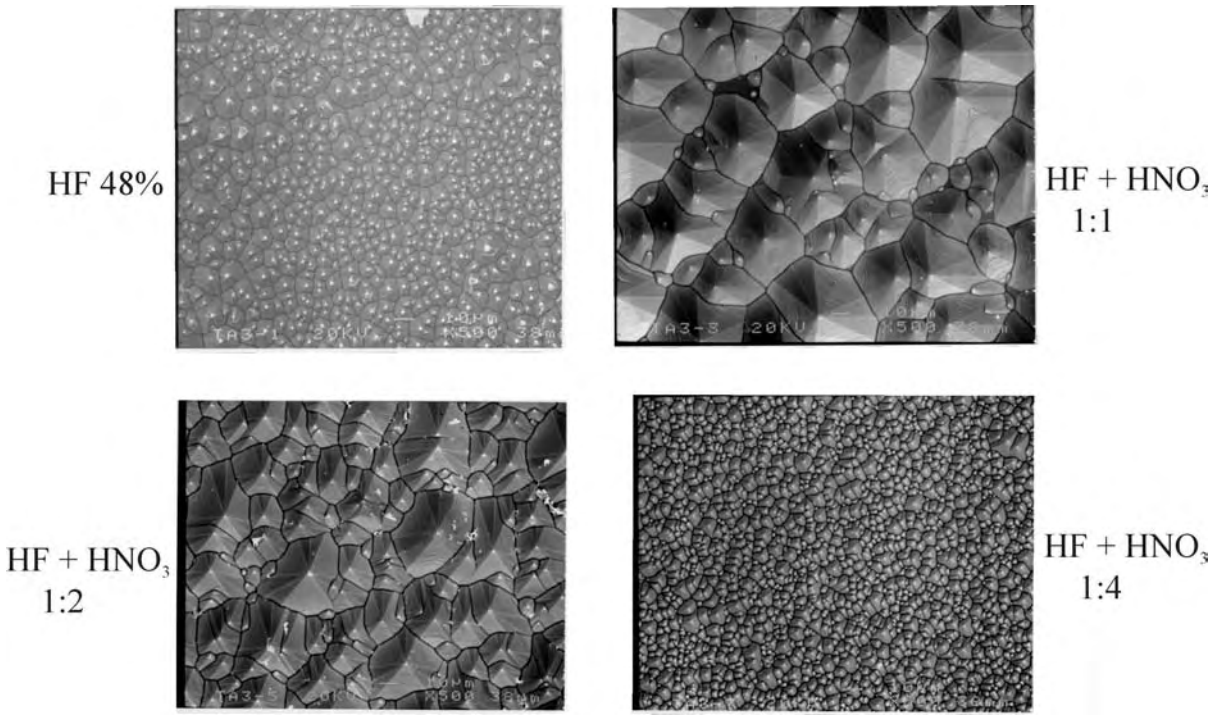

Figure 4.6 Plan views of the same etched surfaces making comparison of the smoothness of all the surfaces more apparent.

4.4.3 Chemistry of etching mechanism and the differential etch rate

A proposed explanation for understanding of the etch mechanism underlying the differential etch behaviour for the +z and –z faces is described in this section. The plots of the variation in the etch depths with change in % proportion of HF in the etch mixtures HF/HNO_3 and HF/H_2O, show an almost linear increase in the etch rate with the amount of HF and a contrastingly superlinear increase in the etch rate with amounts of HF in the latter case. This variation in the etch rate with the concentration of HF or with the proportion of water in the etching mixture has never been addressed so far to our knowledge. In the absence of any previous quantitative report on this etching reaction analogy was drawn from a recently conducted study by (Knotter'00) of HF etching of SiO_2, with hydroxide-terminated surfaces as expected in our case. Knotter concluded that etching of SiO_2 in HF was a controlled fluoride substitution of the surface hydroxide. The accelerating effect of the low pH was attributed to the greater extent of the surface protonation, leading to hydroxide removal as a precursor to fluoridation by the HF_2^- or H_2F_2 at very low pH.

The highly plausible notion that etching is initiated by surface protonation immediately explains two quantitative observations from the etching experiments,

namely the faster etching of -z face due to easier absorption of the positively charged proton, and the increase in the etch rate with increase in the concentration of the acidic protons.

An explanation of the quantitative observations, namely the super linear increase with increase in the HF concentration in the absence of nitric acid and the almost linear increase with amount of HF added to the concentrated nitric acid follows.

4.4.3a HF solutions

The rapid increase in the etch rate as the HF concentration approaches 48% does not correlate with the acid proton concentration computed from the thermodynamic data presented by (Knotter'00). Of the many attempted correlations, the most successful fit and the most plausible physical explanation is shown by the logarithmic plot (figure 4.7), with the rates plotted against the ratio $c_{HF}/c_{H_2O} - c_{HF}$ where c_{H_2O} and c_{HF} are the total molar concentrations of water and HF in the mixture. The logarithmic plot used shows that the etch rate is proportional to the plotted ratio over a range of at least two orders of magnitude. There is a good reason to exclude one of the data points, namely that for the 2:1 ratio, which lies somewhat off the fit for the other points, because of the possibility of a systematic error perhaps in one of the electric field poling parameters used, as this data was taken at a later stage, and was not a part of the first etching studies.

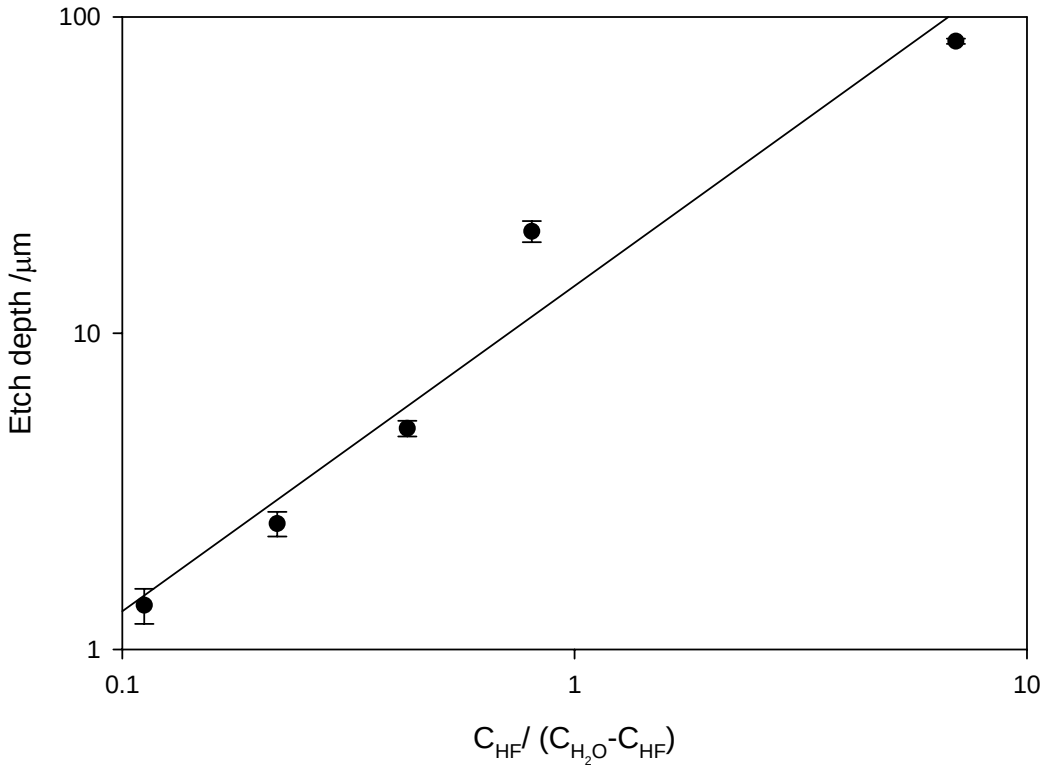

Figure 4.7 Log-log plot showing a variation of the etch depth with c_{HF}/c_{H2O}-c_{HF} for the data shown in figure 4.3. The straight line is a linear regression.

The suggested inverse correlation with the c_{H2O}-c_{HF} is due to the reduced thermodynamic activity of water at high HF concentrations. It is known that the water is complexed by HF to form H_3OF (Cotton'88) so that only the residual, uncomplexed water would be active in the dehydroxylation equilibrium:

$$MOH_s + H^+ \Leftrightarrow M_s^+ + H_2O_{free} \qquad \textbf{4.1}$$

Where MOH_s and M_s represent normal and dehydroxylated surface groups.
If dehydroxylation only occurs for a small fraction of the surface, due to the weakness of the acid, the concentration of the dehydroxylated surface sites can be expressed as:

$$\left[M_s^+\right] = K_1\left[H^+\right]/\left[H_2O_{free}\right] = K_1\left[H^+\right]/\left(c_{H2O} - c_{HF}\right) \qquad \textbf{4.2}$$

However a square root dependence of the etch rate on c_{HF} from this expression should be expected, since the proton concentration itself varies with the square root of c_{HF} according to the equilibrium:

$$H_2F_2 \Leftrightarrow HF_2^- + H^+ \;\; ; \;\; \left[H^+\right] = \left[HF_2^-\right] = K_2\left[H_2F_2\right]^{1/2} \approx K_3 c_{HF}^{1/2} \qquad \textbf{4.3}$$

Computations from Knotter's data show that H_2F_2 is the majority fluorine containing species in the system.

The linear dependence of rate on c_{HF} can be explained by assuming that fluoridation of the surface occurs by an electrostatically enhanced attack of M_s^+ by HF_2^-

$$M_s^+ + HF_2^- \rightarrow MF + HF \qquad \textbf{4.4}$$

$$rate = k_1\left[M_s^+\right]\left[HF_2^-\right] = k_1K_1\left[H^+\right]\left[HF_2^-\right]/\left(c_{H2O} - c_{HF}\right) = k_2 c_{HF}/\left(c_{H2O} - c_{HF}\right) \qquad \textbf{4.5}$$

As required, where $k_2 = k_1K_1K_3^2$

4.4.3b HF/HNO_3 solutions

Data for the etch solutions containing HNO_3 show a simpler relation where the etch rate is simply proportional to the HF concentration. The model in this case assumes that nitric acid is probably strong enough to saturate the negatively charged surface with protons, dehydroxylate completely and then cover the M_s^+ surface with nitrate:

$$MOH_s + H^+ \rightarrow M_s^+ \rightarrow MNO_3 \qquad \textbf{4.6}$$

The subsequent reaction is determined by the rate of fluoride substitution at the surface. Here there is no electrostatic enhancement of HF_2^- attack, so that the more abundant H_2F_2 is more effective than HF_2^- in this case.

$$MNO_3 + H_2F_2 \rightarrow MF + HNO_3 + HF \qquad \textbf{4.7}$$

$$rate = k_3\left[H_2F_2\right] \approx k_4 c_{HF} \qquad \textbf{4.8}$$

This proportionality is verified in the data of figure 4.3, which shows a straight line passing close to the origin as expected, since zero HF gave a zero etch rate. One result which did not fit the model was the result for 48% HF, where the model for the HF solutions was applicable in the absence of nitric acid.

In conclusion the above model also explains the observation that the etch rate is much faster for the negative z face, since a negative face would favour protonation by increasing the value of K_1. Also, the short metal-oxygen bond on the positively charged surface should be more stable, and therefore less reactive than the long bond on the negative surface. The suggested mechanism for the etch rate in aqueous HF involves an initial dehydroxylation of the negatively charged surface by proton attack followed by an electrostatically enhanced reaction of the subsequent positively charged surface with HF_2^- anions, with the rapid increase in the rate near the 48% composition attributed to the reduction in free H_2O concentration. However the linear dependence in the etch rate with the HF concentration for the aqueous HF/HNO_3 solutions is a result of the attack of the nitrate covered positive surface by the abundant neutral species H_2F_2, with an initial protonation considered essential in both cases, and much slower on the positively charged face.

4.5 Investigation of time delay on the etching mechanism in lithium niobate

Experiments to investigate a possible latency effect, in the etching mechanism of single crystal lithium niobate after domain inversion by electric field poling were performed. A simple set of experiments to ascertain if there is any observable change between the etch rates of the virgin and the newly poled regions of lithium niobate samples, etched at different intervals of time after poling are described in this section. These experiments to gather any information about the effect of relaxation of inherent internal fields with time reflected in the consequent time dynamic movements of atoms, on the mechanism of differential etching (the etch rates and the etch quality) were conducted as they could be an essential tool in aiding the micro-structuring experiments.

4.5.1 Experiments and results with HF/HNO_3 solution

A standard 500µm thick z-cut lithium niobate wafer was diced into rectangular samples of dimension 50mm x 20mm and subsequently subjected to a standard

sequential solvent cleaning procedure. The cleaned sample was spin coated, photolithographically patterned and subsequently developed to produce a rectangular region, having a dimension of 42mm x 10mm, in the middle of the sample. The rectangular area, defined by the previous step of photolithography was then transferred to the sample bulk by the conventional electric field poling, which has the effect of inverting the ferroelectric domain within the pre-selected rectangular region. The sample was then diced off into six separate samples each of which had a domain inverted region with a dimension of 7mm x 10mm. As with previous experiment conducted to study the effect of the different ratios of the acids in the used etchant mixture on the etch rates, so also in this case it was essential to select test samples diced from one poled sample, to ensure as much uniformity as possible, in both the source material and the associated processes.

The poled and diced samples were then etched at different times, in a mixture of HF and HNO_3 acid at an elevated temperature of 60^0C, for a period of twenty hours. The ratio of HF:HNO_3 in the etchant mixture was 1: 4, which as deduced from the previous set of etching studies, was known to yield smoother etched regions and a higher differential etch rate between the virgin region and the newly poled region. The hydrofluoric acid used was a 48% solution in water whereas the nitric acid was a 70% solution in water, and their purity was of electronic grade.

The poled samples were placed on a specially designed sample holder, which was immersed in a PTFE beaker containing the etchant mixture. The etchant mixture was continuously stirred so as to uniformly etch the sample face. An integral hot plate with a stirrer ensured uniform etching and maintained the desired temperature.

The first sample was etched five hours after poling. One of the samples was annealed for five hours at a temperature of 350^0C in an oxygen rich environment, a known technique used to reduce the electric field poling induced stresses in the crystal. The annealed sample and another of the diced samples were etched, 24 hours after they had been poled. Two other samples were etched 21 days and 42 days, after poling. This long time delay was to ascertain whether such time lags relax any internal field present within the poled sample, in turn producing different etch rates after different time periods. The etched samples were then characterised using a surface profilometer, Tencor-200 alphastep, for measuring the etch depths d_1 and d_2 on the two faces. The etch depth measurements; d_1 and d_2 are as shown in the schematic in figure 4.1. An average of twenty different depth measurements was taken at different

positions on the sample faces for each of the two data points, to reduce any error in the measurements, due to lack of smoothness of the etched region. A table of measurements for the two etch depths along the two faces of samples, etched at different times after poling is given below:

	Etch depth measurement with std deviations, on the –z face (having a poled +ve region) d_1 in μm	Etch depth measurement with std deviations, on the +z face (having a poled –ve region) d_2 in μm
Sample etched after 5 hours	29.58 ± 1.78	27.31 ± 1.54
Sample etched after 24 hours (with no intermediate annealing step)	52.04 ± 2.66	51.33 ± 2.67
Samples etched after 24 hours (annealed before etching)	53.83 ± 2.72	52.82 ± 2.00
Sample etched after 21 days	33.73 ± 0.67	34.36 ± 0.79
Sample etched after 42 days	34.95 ± 1.12	35.56 ± 1.37

Table 4.3 Etch depth measurements for samples etched in HF/HNO_3 mixture in the ratio if 1:4, at 60^0C for 20hrs.

As observed in the previous etching study, no definite trend suggestive of a secondary differential etch rate between the virgin material and a newly poled region is evident. The set of obtained data does indicate a similar pattern for the etch depth measurements on the two faces, with a sudden peak in their values for the 24hrs measurement as seen in figure 4.8.

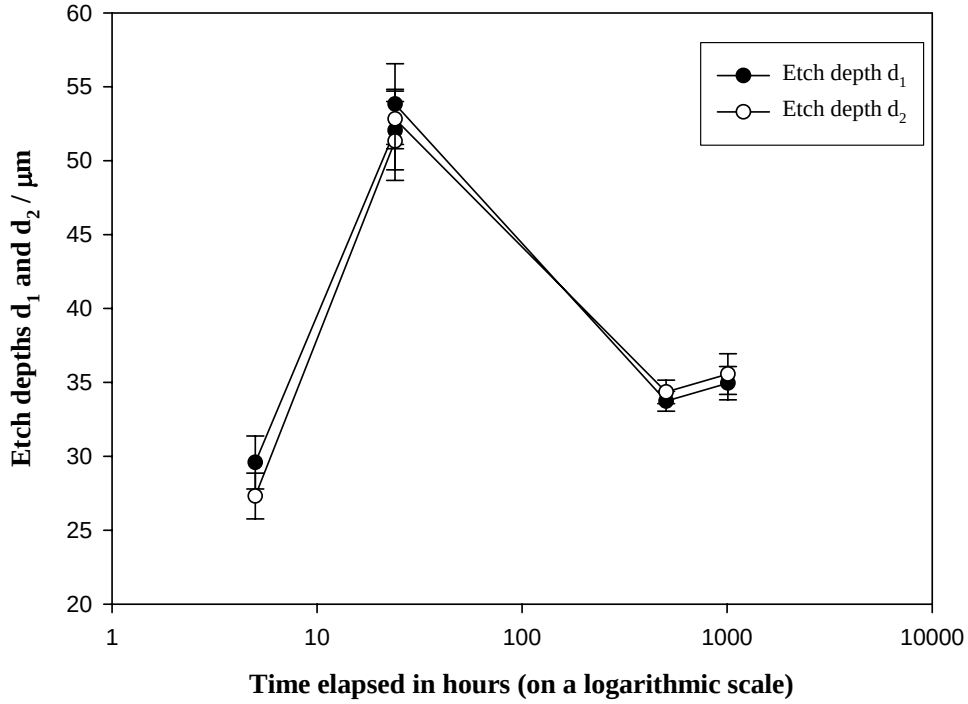

Figure4.8 A plot of the etch depth measurements d_1 and d_2 versus time for the different samples etched for a period of 20hrs at a temperature of 60^0C in HF/HNO_3 mixture in the ratio of 1:4.

4.5.2 Experiments and results with HF solution

To conclusively ascertain this sudden variation in the etch depth/etch rate was not a random measurement error a similar experiment was performed however in this case the samples were etched at room temperatures and in the pure HF acid for a period of 10hrs. The smoother etched surfaces with use of pure HF would also reduce the deviations in each of the measured depths d_1 and d_2. The data collected from this study is shown in table 4.4 and plotted in the graph depicted in figure 4.9.

	Etch depth measurement with std deviations, on the –z face (having a poled +ve region) d_1 in μm	Etch depth measurement with std deviations, on the +z face (having a poled –ve region) d_2 in μm
Sample etched after 4 hours	9.49 ± 0.46	9.69 ± 0.31
Sample etched after 14 hours	9.63 ± 0.42	10.12 ± 0.30
Sample etched after 24 hours	10.23 ± 0.44	10.47 ± 0.32
Sample etched after 34 hours	9.68 ± 0.32	9.95 ± 0.37

Table 4.4 Etch depth measurements for samples etched in pure HF at room temperature for 10hrs

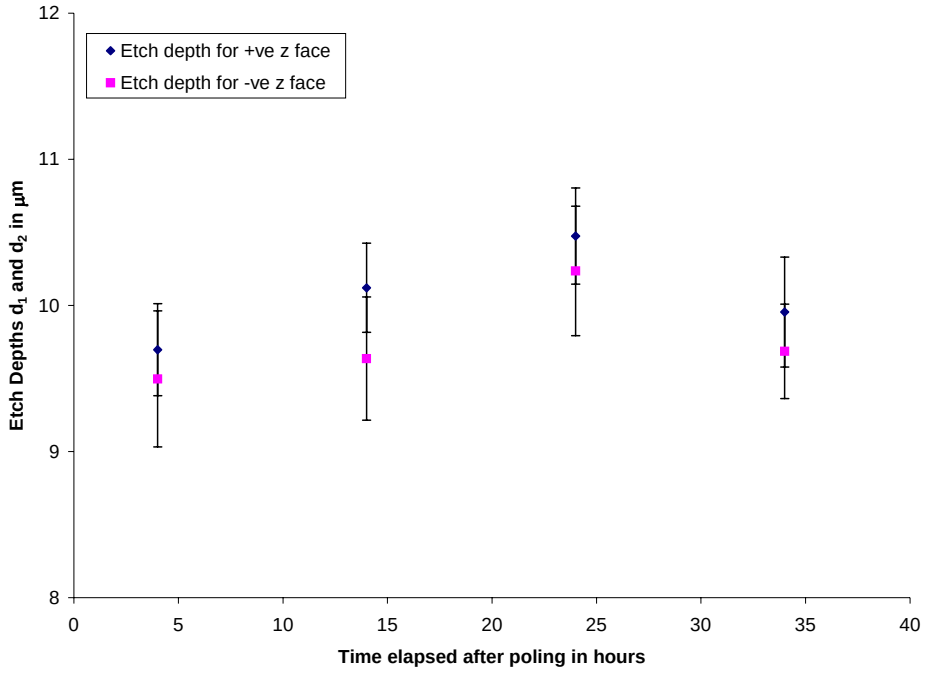

Figure 4.9 Plot showing the variation in the etch depths d_1 and d_2 with time for samples etched in pure HF at room temperature for 10hrs.

A closer examination of the plotted data shows a similar increase in the etch depth/etch rate for the 24hr measurement, though not quite as discernible as from the first set of experiments with the HF/HNO_3 mixture it is apparent that the etching behaviour is sensitive to time delay, and possibly therefore to the presence of the

internal fields. As a relatively small displacement in the positions of Li and Nb atoms within the crystalline unit cell is sufficient to produce a significant difference in the corresponding etch rate for the –z and +z faces, the observed time dependent change in the etch rate following poling is a clear indication of extremely small displacement in the atomic positions (Scott'03).

Raman spectroscopic analysis, sensitive to any variation in atomic positions within a sample was employed to study the time dynamics of the spectral positions of the six major single peaks in the observed Raman spectrum of single crystal congruent lithium niobate. (All the Raman measurements were done by fellow research colleague Jeffrey Scott, using facilities available at the department of chemistry of the university). The precise positions of the six peaks prior to poling were established by four different Raman spectral measurements at two different positions on the –z face of a virgin z-cut sample. Domain inversion was then achieved by the conventional e-field poling technique, and further spectral measurements were then recorded at intervals of 8 minutes for a total period of 4 hours. A small spectral shift (<1 cm^{-1}) in the absolute spectral positions of each of the six Raman lines centred at 153, 237, 332, 432, 581 and 872cm^{-1} was observed, with two peaks shifted to higher frequencies and four to lower frequencies. Some of the lines were also seen to recover with differing times towards their original positions before poling with time constants of the order ~few hours. Most interestingly the differences in the deduced recovery times are consistent with the reported multistep electronic and ionic relaxation processes in lithium niobate and lithium tantalate. The time constants for the recovery of the internal fields following poling have been reported to vary from tens of milliseconds (Ro'00) through several days (Gopalan'97) to even being incomplete after a month (Gopalan'98b).

The collected etch-data in tables 4.3 and 4.4 substantiate the supposition that there is a recovery of the exact atomic or ionic positions following poling, which is reflected by the approximate factor of two increase in the etch rates seen after a time delay of 24 hours (measurements in table 4.3).

In conclusion the very small atomic displacements which result in the observed Raman spectral shifts translate into a measurable variation of etch rates much less than the reported differential etch rates between the –z and +z faces of lithium niobate (Barry'98).

4.6 LIFE study

LIFE is an acronym for Light Induced Frustrated Etching, of doped and undoped lithium niobate. It explains the effect of incident light, which can reduce or completely inhibit the normal etching mechanism of lithium niobate. This is to say that incident light can partially or even totally frustrate the etching behaviour. So far, frustrations of etching (Barry'99), and the presence of a latent etch frustration effect (Boyland'00) has been observed of –z face of z-cut Fe: doped lithium niobate single crystals, with use of visible c.w laser radiation of wavelength 488nm.

The explanation of this behaviour can be attributed to the photoelectrochemical modification of the etching mechanism as a result of light induced charge migration from the dopant Fe ions. This latent effect, in which the illumination of the sample has a marked effect on the subsequent etching at the lithium niobate etchant interface, for periods of at least several hours after the illumination had been removed, could also be a resultant contribution from the bulk photovoltaic effect, which is known to be stronger in relatively heavily doped crystals (Huignard'89).

The strength of this photovoltaic effect is characterised by the concentration of the Fe dopant. Its two valence states, Fe^{+2} and Fe^{+3}, play a major role, with the photoconductivity determined by the electron transfer by these two states (Sommerfeldt'88). This charge transfer is particularly pronounced in the visible absorption bands of Fe^{+2} at approximately 2.6eV (476nm) and for Fe^{+3} at 2.55eV (488) and 2.95eV (420). The motion of excited electrons along the c-axis generates a light-induced photovoltaic current. Discretely spaced inhomogeneities, created by the diffusion of impurity atoms and vacancies, serve as donors and traps for the electrons. The flow of the photovoltaic current through the defects leads to an accumulation of charges and thereby subsequent repolarisation (Nagata'00), which not only creates microdomains but also causes large defects to develop in the wafer. The accumulation of the charges affects the diffusion of the fluorine ions from the etchant and hence the etching mechanism. In undoped crystals the mechanism is vastly different from that in the doped crystals and is mainly a contribution of the direct intraband excitation, as the excitation photon (248nm, ~4.8eV) is of energy exceeding the band gap (~4eV) of the crystal (Weis'85). However taking into account the small penetration depth and the short pulse duration of the illuminating laser beam it seems reasonable that the underlying principle in the generation of free charge carriers may not be the bulk photovoltaic effect but the Dember effect, observed in insulators (Kallmann'60) and

semiconductors (Badics'79), wherein equal number of oppositely charged carriers generated in the illuminated region subsequently migrate depending on their respective mobilities generating a voltage difference across the bulk. An inhomogeneous excitation results in a concentration gradient of free charge and a consequent photovoltage (Kallmann'60). It is likely that the space charge distribution excited by the radiation enables the latent etch frustration effect.

4.6.1 Experiments and Results

The experimental work involved the illumination of congruent lithium niobate samples by the output of a 500 fs excimer laser followed by their immediate etching in the mixture of $HF+HNO_3$, in a volumetric ratio of 1:2. High quality projection of various patterns of ~μm scale, on the negative face of the crystal, was obtained by spatial modulation of the laser beam, with the aid of an optical projection microscope system.

The optical system comprised a modified optical microscope with a Schwartzchild reflecting x25 objective, specially coated for high reflection at 248nm, enabling demagnification of the projected aperture and an optical attenuator for controlling the throughput. Rectangular features 180μm in length and ~10μm in width were printed on the face of the sample. Optical throughputs with values between 12% and 0.12% were employed by using the attenuator, with the energy reaching the surface at zero attenuation being 0.55mJ, corresponding to an intensity of 1.1×10^{12} W/cm^2, after projection from the objective to a spot size of 240x240μm^2. The laser ablation threshold was then determined, which turned out to be 60mJ/cm^2, slightly less than the value of 80mJ/cm^2, obtained for the conventional KrF nsec excimer laser pulse at 248 nm. Our interest being in illumination at fluences below threshold, where the laser fluence is insufficient for removal of material from the surface, we performed investigations with varied fluences and pulses to observe the effect of the intensity and the exposure on the etch frustration mechanism. An array of spots with rows of different fluences and columns of different number of pulses were recorded on the –z face of the sample. The fluences used were 885mJ/cm^2, 398mJ/cm^2, 177mJ/cm^2, 44mJ/cm^2 and 9mJ/cm^2 at 1, 10, 100 and 1000 pulses respectively.

A transition from direct laser ablation to etch frustration was observed, which was evident from the ablation pits formed for fluences above 60 mJ/cm^2, seen in the alpha step measurement of the surface in figure 4.10.

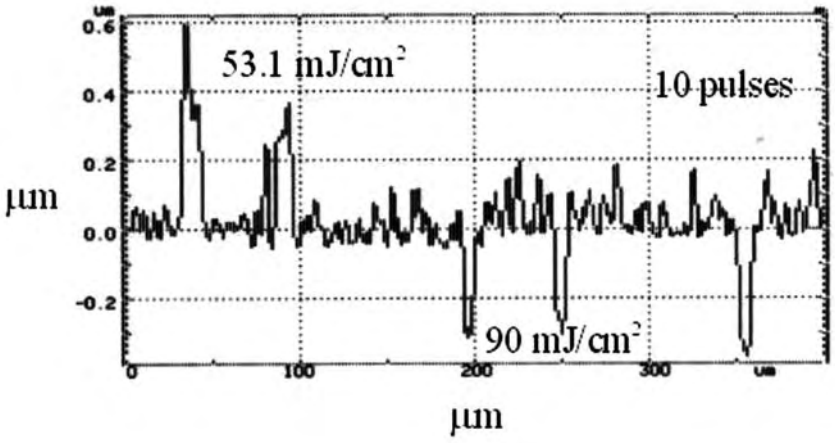

Figure 4.10 Alpha step scan showing a transition from ablation to etch frustration; with the two ridges on the left of the scan corresponding to the 10 pulse irradiation at 53.1mJ/cm^2 while the ones on the right correspond to 10 pulse irradiation at 90mJ/cm^2

It was also deduced that a saturation of the etch frustration effect was also observed for pulses at or below the 100 pulses level for a fluence of 44.25mJ/cm^2 as the heights of the ridges formed by the etch frustration after a 100 pulse illumination was nearly the same as that for the 1000 pulse illumination too. An alpha step scan showing this is shown in figure 4.11.

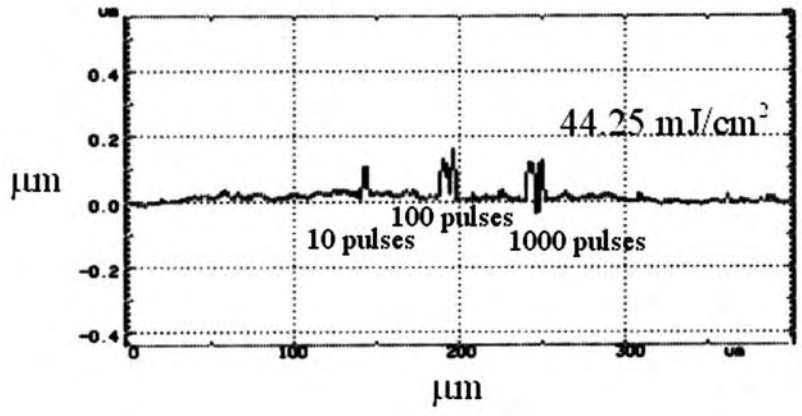

Figure 4.11 Alpha step scan of the etch frustration ridges produced by an illumination fluence of 44mJ/cm^2 followed by a one hour wet etching at room temperature. Saturation is apparent for exposure at or below 100 pulses.

The saturated ridge height after one hour of etching was 100nm, which indicates an etch frustration of ~20%, the normal etch rate without illumination being nearly 550nm. Different saturation levels and hence different etch frustration levels were observed for different energy fluences. The alpha step scan shown in figure 4.10 shows the twin ridges having a height of near about 400nm for a 10 pulse illumination at a fluence of 53.1mJ/cm^2, which corresponds to an etch suppression of ~80%. The scan also shows twin ablation pits corresponding to an ablation above threshold of 90mJ/cm^2. A scanning electron microscopy picture of the two regions mentioned above is as shown in the figure 4.12.

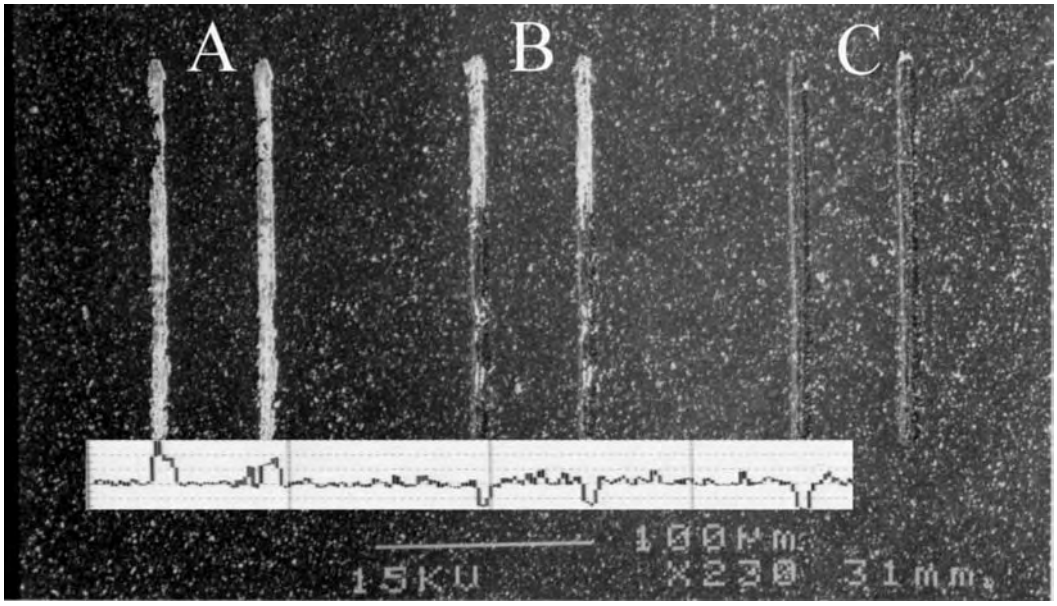

Figure 4.12 SEM image showing a transition from etch frustration to laser ablation. Repeated sets were produced for three different values of exposure. The inset is a rescaled version of figure 4.10, allowing a direct comparison.

The pre-illumination of lithium niobate sample faces was done by fellow research colleague Sakellaris Mailis, using laser facilities available at F.O.R.T.H-IESL, Laser and Application division, in Crete, Greece.

4.7 Summary

Domain visualisation techniques used to assess the quality of domain inversion were discussed in brief followed by a discussion at length of the frequently used visualisation approach of wet or chemical etching in the context of the potential application of this technique for micro-structuring lithium niobate.

A parametric study of the etch rates and the etch quality as a function of the traditionally used etchant mixture of 'HF:HNO_3 in the specific ratio of 1:2' to ascertain if indeed it was the ideal choice for achieving the optimal differential etch rates and etch quality, and also investigate a recently observed second differential etch behaviour was presented. It was immediately apparent from the experimental investigations that the widely used ratio was optimum neither in the etch depths achieved nor in the smoothness achieved for the etched –z faces, moreover it can be conclusively seen that the etch rate achieved with that ratio is approximately half of that with the pure HF solution. The best results for the depth and the smoothness were observed for the pure HF solution at the temperature of 60^0C. The hugely improved degree of smoothness associated with the pure HF solution could be exploited for realising deep three-dimensional structures on lithium niobate.

The set of data collected from the etching studies with different HF:HNO_3 and HF:H_2O ratios are suggestive of a second differential etch rate between the newly poled material and the virgin material. The behaviour is well quantified by the contrast ratio parameter and could be of potential use in structuring application where precise control of the etch rates and back etching is desirable.

A proposed reaction formulation explaining the observed differential etching mechanism between opposing crystallographic z-faces was also discussed (Sones'02). The suggested mechanism for the etch rate in aqueous HF involves an initial dehydroxylation of the negatively charged surface by proton attack followed by an electrostatically enhanced reaction of the subsequent positively charged surface with H_2^- anions, with the rapid increase in the rate near the 48% composition attributed to the reduction in free water concentration. However the linear dependence in the etch rate with the HF concentration for the aqueous HF:HNO_3 solutions is a result of the attack of the nitrate covered positive surface by the abundant neutral species H_2F_2, with an initial protonation considered essential in both cases, and much slower on the positively charged face.

Systematic experimental trials were conducted to gather information about the effect of a time delayed internal field relaxation, on the mechanism of differential etching; the etch rates and the etch quality, as this could prove be an essential tool in aiding the micro-structuring experiments undertaken. The experimental data for the HF:HNO_3 ratio at an elevated temperature and that for the pure HF solution at room temperature

revealed a latent etch mechanism in lithium niobate, also evidenced by Raman studies conducted within the research group. The set of obtained data do not indicate any conclusive trend in the etch rates with time, which was thought to relax the internal field within the poled crystal.

Preliminary experiments with the light-induced-frustrated-etching technique have been presented demonstrating its applicability for structuring un-doped congruent z-cut lithium niobate, resulting in the formation of μm scale surface relief structures. A modification in the chemical etching behaviour of undoped congruent z-cut lithium niobate single crystals was observed on pre-illumination of the –z face of the crystal with sub-picosecond UV laser radiation at 248nm from an excimer laser for energy fluences only below the ablation threshold of lithium niobate (Mailis'02). A systematic study of the effect of the incident energy fluence and total exposure on the etch frustration phenomenon revealed with 20%-80% slower etch rates for the illuminated areas varying with the illuminating energy fluence and exposure were observed. Different saturation levels and hence different suppression levels were also observed for different illuminating energy fluences. The phenomenological explanation of the effect involves laser induced mobile charge carriers which interfere with the electrochemistry of lithium niobate surface effectively reducing the chemical etch rate.

4.8 References

Badics G, Szalmassy, *Phys.Lett A*, **69(5)**, 364, 1979.

Barry I.E, Ross G.W, Smith P.G.R, Eason R.W, Cook G, *Mater.Lett*, **37**, 246, 1998.

Barry IE, Eason RW, Cook G, *Appl.SurfaceSci*. **143(1-4)**, 328, 1999

Berkovic G, Shen Y.R, Marowsky G, Steinhoff R, *J. Opt. Soc. Am. B*, **6**, 205, 1989.

Bluhm H, Wadas A, Wiesendanger R, Roshko A, Aust J.A, Nam D, *Appl. Phys. Lett*, **71(1)**, 146, 1997.

Boyd G.D, Miller R.C, Nassau K, Bond W.L, Savage A, *Appl. Phys. Lett*, **5(11**), 234, 1964.

Boyland AJ, Mailis S et al, *Appl.Phys.Lett*. **77(18)**, 2792, 2000

Bozhevolnyi S.I, Hvam J.M, Pedersen K, Laurell F, Karlsson H, Skettrup T, Belmonte M, *Appl. Phys. Lett*, **73(13)**, 1814, 1998.

Brown PT, Eason RW, Ross GW, Pogosyan AR, *Opt.Commun*, **163**, 310, 1999

Chao S, Davis W, Tuschel DD et al, *Appl.Phys.Lett*, **67**, 1066, 1995

Cho Y, Kazuta S, Matsuura K, *Appl. Phys. Lett*, **75(18)**, 2833, 1999.

Cho Y, Kirihara A, Saeki T, *1*, **67**, 2297, 1996.

Cotton FA and Wilkinson G, *Advanced Inorganic Chemistry*, Wiley, New York, **5th ed**. p.104, 1988

Gao C, Duewer F, Lu Y, Xiang X.D, *Appl. Phys. Lett*, **73(8)**, 1146, 1998.

Gopalan V, Gupta M.C, *Appl. Phys. Lett*, **68(7)**, 888, 1996a

Gopalan V, Gupta M.C, *Ferroelectrics*, **198(1-4)**, 49, 1997.

Gopalan V, Gupta M.C, *J. Appl. Phys*, **80(11)**, 6099, 1996b

Gopalan V, Jia Q.X, Mitchell T.E, *Appl. Phys. Lett*, **75(16)**, 2482, 1999 (a).

Gopalan V, Mitchell T.E, Furukawa Y, Kitamura K, *Appl. Phys. Lett*, **72(16)**, 1981, 1998a

Gopalan V, Mitchell T.E, *J. Appl. Phys*, **85(4)**, 2304, 1999b.

Gopalan V, Mitchell T.E, *J.Appl.Phys*, **83(2)**, 941, 1998b

Huignard JP and Gunter P, *Photorefractive Materials and their Applications: Topics in Applied Physics*, Springer, Berlin, *61*,1989

Kallmann H, Bernard K, Shain J, Spruch G.M, *Phys.Rev*, **117(6)**, 1482, 1960.

Knotter D.M, *J.Am.Chem.Soc*, **122**, 4345, 2000

Kurimura S, Uesu Y, *J. Appl. Phys*, **81(1)**, 369, 1997.

Laurell F, Roelofs M.G, Bindloss W, Hsiung H, Suna A, Bierlein J.D, *J. Appl. Phys*, **71(10)**, 4664, 1992.

Luthi R, Haefke H, Meyer K.P, Meyer E, Howald L, Guntherodt H.J, *J. Appl. Phys*, **74(12)**, 7461,1993.

Mailis S, Brown P.T, Sones C.L, Zergioti I, Eason R.W, *Appl.Phys A*,**74(2)**, 135, 2002.

Missey M.J, Russell S, Dominic V, Batchko R.G, Schepler K.L, *Opt. Express*, **6(10)**, 186, 2000.

Nagata H, Ichikawa J et al, *J.Mater.Research*, **15**, 17, 2000

Narshimamurty T.S, *Photoelastic and Electro-optic Properties of Crystals*, Plenum, New York, 1981.

Nassau K, Levinstein H.J, Loiacono G.M, *J. Phys. Chem. Solids*, **27**, 983, 1966.

Orlik X.K, Labardi M, Allegrini M, *Appl. Phys. Lett*, **77(13)**, 2042, 2000.

Prokhorov A.M, Kuzmonov Yu.S, '*Physics and chemistry of crystalline Lithium Niobate*', Adam Hilger, Bristol, 1990.

Ro J.H, Cha M, *Appl.Phys.Lett*, **77(15)**, 2391, 2000

Pruneri V, Webjorn J, Russell P.St.J, Barr J.R.M, Hanna D.C, *Opt.Commun*, **116(1-3)**, 159, 1995

Saurenbach F, Terris B.D, *Appl. Phys. Lett*, **56(17)**, 1703, 1990.

Scott J.G, Mailis S, Sones C.L, Eason R.W, Accepted for publication in *Appl.Phys A*

Shur V.Ya, Nikolaeva E.V, Shishkin E.I, Chernykh A.P, Kitamura K, Ito H, Nakamura K, *Ferroelectrics*, **269**, 195/1043, 2002.

Shur V.Ya, Rumyantsev E.L, Nikolaeva E.V, Shishkin E.I, *Appl. Phys. Lett*, **77(22)**, 3636, 2000.

Shur V.Ya, Rumyantsev E.L, Nikolaeva E.V, Shishkin E.I, Batchko R.G, Fejer M.M, Byer R.L, *Ferroelectrics*, **257(1-4)**, 191, 2001

Sommerfeldt R, Holymann L et al, *Phys.Status Solidi A*, **106**, 89, 1988.

Sones C.L, Mailis S, Brocklesby W.S, Eason R.W, Owen J.R, *J.Mater.Chem*, **12(2)**, 295, 2002

Tyunina M, Wittborn J, Rao K.V, Levoska J, Leppavuori S, Sternberg A, *Appl. Phys. Lett*, **74(21)**, 3191, 1999

Uesu Y, Kurimura S, Yamamoto Y, *Appl. Phys. Lett*, **66(17)**, 2165, 1995

Weis RS, Gaylord TK, *Appl.Phys.A*, **37**, 19, 1985

Wittborn J, Canalias C, Rao K.V, Clemans R, Karlsson H, Laurell F, *Appl. Phys. Lett*, **80(9)**, 1622, 2002

Yang T.J, Gopalan V, Swart P.J, Mohideen U, *Phys.Rev.Lett*, **82(20)**, 4106, 1999

Yang T.J, Mohideen U, Gupta M.C, *Appl. Phys. Lett*, **71(14)**, 1960, 1997

Chapter 5
Surface domain inversion and applications

5.1 Introduction and chapter layout

Non-linear frequency conversion employing periodically poled ferroelectrics has been researched since the early days of integrated optics and still continues to generate interest. The availability of efficient solid-state lasers in the near-infrared wavelength regime has been made possible by the advent of diode lasers with considerable powers. However, until recently it had not been possible to extend room temperature operation of diode lasers deeper into the visible (shorter than 600nm) and the deep-infrared (larger than 2μm) wavelength region with similarly large efficiencies as those that operate at e.g. 800nm, consequently rendering an absence of coherent laser sources for potential applications such as high-density optical storage. Non-linear frequency conversion of a near infrared diode laser output, to extend the existing range of available range of all-solid-state laser wavelengths seems to be a potential answer to this problem.

Frequency conversion through non-linear interaction can be achieved in either bulk or waveguide geometries in periodically poled ferroelectric media. However as non-linear conversion processes in waveguides can be several orders of magnitude more efficient than single-pass bulk interactions (Stegeman'85), waveguide frequency conversion is an attractive route for such processes. While waveguide frequency conversion promises a lot, the realisation of such processes requires material with a reasonably large non-linear susceptibility, and a low-loss waveguide technology compatible with phase-matching requirements. Several phase-matching routes such as birefringent phase-matching, quasi-phase-matching, modal dispersion and Cerenkov effect have been used; however each technique has its own strengths and weaknesses.

In birefringent phase-matching, the interacting waves are polarised orthogonally so that the birefringence can be used to compensate for the phase velocity mismatch due to the dispersion of the refractive indices. The choice of the non-linear crystal to be used in birefringent phase-matching is thus limited to those having an appropriate balance of dispersion and birefringence. Additionally the technique limits interactions to those involving components of the non-linear susceptibility tensor that can couple orthogonally polarised waves. These constraints hence limit the choice of materials

and also the range of wavelengths accessible, with operations at inconvenient temperatures often required. Other phase-matching options, such as modal dispersion (Stegeman'85) and the Cerenkov effect (Taniuchi'87) are often accompanied by reduced conversion efficiency and non-optimal output modes. The alternative phase-matching approach of quasi-phase-matching uses the periodic modulation of the direction of the spontaneous polarisation / non-linear susceptibility of the ferroelectric material to compensate the phase velocity mismatch between the interacting waves.

Well understood waveguide fabrication techniques in lithium niobate in conjunction with periodic domain inversion technique leads to a very flexible phase-matching technique.

In the simplest quasi-phase-matched interaction process, referred to as second harmonic generation, appropriate periodic modulation of the non-linear susceptibility of the material eliminates the accumulation of phase velocity mismatch between the interacting waves, effectively directing the power flow in the interaction from the fundamental to the second harmonic wave. In the non-phase-matched situation the direction of the power flow reverses periodically as the relative phase between the interacting waves changes, resulting in an oscillation in the power in the generated second harmonic, initially growing while the two are in phase, then decreasing after the phase difference reaches π at a distance of l_c (coherence length), ultimately returning to zero after a distance $2l_c$.

Appropriate selection of the modulation period (l_c), allows the use of the material over its entire transparency range, taking advantage of any (and ideally the largest) component of the non-linear susceptibility tensor. In the case of lithium niobate, interaction is possible involving wavelengths within its transparency range of 0.4 to >5μm, using the non-linear coefficient d_{33} which is seven times greater than the birefringently phasematchable coefficient d_{31}.

One of the major hurdles that prevented widespread use of this phase-matching technique was the difficulty encountered in reversing the sign of the non-linear coefficient every coherence length at such small (few μm) periodicity. However with the demonstration of electric field induced inversion of the spontaneous polarisation in lithium niobate, quasi-phase-matching employing a periodic array of domains with alternating spontaneous polarisations now ranks as the preferred phase-matching route.

Quasi-phase-matched interaction for converting wavelength from the near infrared into the blue / near-ultraviolet region require periodic modulations of the order of 2-4 μm for the most efficient first-order interaction. Conventionally electric field poling applied to bulk crystal samples however has its shortcomings when such short periods are desired because of the stringent aspect ratio requirement, which makes it effectively impossible to implement. A modified periodic poling technique referred to as surface periodic poling, which overcomes the shortcomings of the conventional electric field poling technique and allows the fabrication of periodic structures with periods as short as 1μm, has been developed here, and is described in this chapter.

This chapter begins by introducing the concept of quasi-phase-matching for non-linear interactions using periodically domain-inverted ferroelectrics such as lithium niobate. The following section explains electric field induced periodic poling in brief and the modified surface poling approach, which is one of the important contributions of this research. The final section of the chapter then describes the application of this poling technique for quasi-phase-matched blue light generation from a surface periodically poled Ti-indiffused channel waveguide in lithium niobate.

5.2 Second harmonic generation and quasi-phase-matching in waveguides

As discussed briefly in chapter 2, linear and non-linear optical effects can be described in terms of a linear polarisation P_L and a non-linear polarisation P_{NL} induced by an electric field as follows:

$$P_i = P_i^L + P_i^{NL} = \varepsilon_0 \chi_{ij}^{(1)} E_j + \varepsilon_0 \chi_{ijk}^{(2)} E_j E_k + \ldots \qquad \textbf{5.1}$$

Where 'χ' is the susceptibility tensor and 'ε_0' is the vacuum permittivity, and E_i are the electric field components.

Several non-linear effects such as second harmonic generation; sum frequency generation, difference frequency generation, optical parametric generation etc can be distinguished on the basis of the electric fields involved in the above equation. Sum frequency generation, as an example, is the mixing of two incident light waves of frequencies ω_1 and ω_2 producing a wave with frequency $\omega_3 = \omega_1 + \omega_2$. This effect can be represented in terms of the non-linear polarisation as follows:

$$P_i^{NL}(\omega_3) = \varepsilon_0 \chi_{ijk}^{(2)}(-\omega_3, \omega_1, \omega_2) E_j^{\omega_1} E_k^{\omega_2} \quad \textbf{5.2}$$

Second harmonic generation, or frequency doubling, is a special case of sum frequency generation, wherein a single incident light wave of frequency ω, generates a wave with twice the frequency. The non-linear polarisation for this case can then be expressed as:

$$P_i^{NL}(2\omega) = \varepsilon_0 \chi_{ijk}^{(2)}(-2\omega,\omega,\omega) E_j^{\omega} E_k^{\omega} = 2\varepsilon_0 d_{ijk}(-2\omega,\omega,\omega) E_j^{\omega} E_k^{\omega} \quad \textbf{5.3}$$

Where d_{ijk} is the non-linear optical coefficient.

Substitution of the non-linear polarisation into Maxwell's equation yields the coupled-mode formalism, which yields the energy exchange between the amplitudes of the interacting fundamental and second harmonic waves (Yariv'73). Let us assume that the non-linear interaction takes place within a waveguiding region where the fields are guided in both the *x* and *y* directions. For simplicity we assume that there is interaction between a single fundamental and a single second harmonic mode (both modes involved could however also be of different orders) and interactions occur between the TE modes only. We also use a non-depleted pump approximation where we neglect the depletion of the fundamental beam as a result of energy transfer into the second harmonic during their interaction. Under these simplifying assumptions the coupled mode theory gives the growth rate for the second harmonic amplitude as follows:

$$\frac{dE_{2\omega}(z)}{dz} = -\,i\,K\,E_{\omega}^{2}(z)\,e^{-i\Delta\beta z} \quad \textbf{5.4}$$

where $\Delta\beta = \beta_{2\omega} - 2\beta_{\omega}$ with $\beta_i = (2\pi / \lambda_i)\, n_i$, describes the phase velocity mismatch between the fundamental and the second harmonic. λ_i is the corresponding wavelength in vacuum and n_i the refractive indices.

The coupling constant K in the above equation can be expressed as:

$$K = \frac{\omega}{c} \frac{d_{eff}^2}{n_{2\omega}} \iint E_{2\omega}(x,y) E_{\omega}^2(x,y) dx dy \quad \textbf{5.5}$$

Where d_{eff} is referred to as the effective non-linear coefficient of the material. The second harmonic power at the end of the waveguide can be deduced by integrating equation 5.4 to yield:

$$P_{2\omega}(L) = \frac{2\omega^2}{\varepsilon_0 c^3} \frac{d_{eff}^2}{n_{2\omega} n_{\omega}^2} L^2 [P_{\omega}(0)]^2 h(\Delta\beta,\alpha_{\omega},\alpha_{2\omega},L)\Gamma \quad \textbf{5.6}$$

Where $P_{\omega}(0)$ is the fundamental power at the beginning of a waveguide of length L, and Γ is an overlap integral. The quadratic dependence of $P_{2\omega}(L)$ on the non-linear susceptibility suggests the use of materials with higher values of the optical susceptibility for an enhanced second harmonic power. Moreover for waveguide interactions it is essential that the waveguide fabrication techniques maintain the non-linearity within the guiding region.

The function h, which includes the dependence of the second harmonic power on the phase mismatch $\Delta\beta$ and the integrated loss coefficients α_i at each of the two wavelengths, is expressed as follows:

$$h(\Delta\beta,\alpha_{\omega},\alpha_{2\omega},L) = \exp\left(-\left(\frac{\alpha_{2\omega}}{2}+\alpha_{\omega}\right)L\right)\frac{(\sinh(\Delta\alpha L/2)\cos(\Delta\beta L/2))^2 + (\cosh(\Delta\alpha L/2)\sin(\Delta\beta L/2))^2}{(\Delta\alpha^2+\Delta\beta^2)L^2/4} \quad \textbf{5.7}$$

where $\Delta\alpha = \frac{\alpha_{2\omega}}{2} - \alpha_{\omega}$

For a lossless waveguide α_{ω} and $\alpha_{2\omega}$ are zero and h can then be expressed as follows:

$$h(\Delta\beta, L) = \frac{\sin^2(\Delta\beta L/2)}{(\Delta\beta L/2)^2} \quad \textbf{5.8}$$

and for the phase-matched situation with $\Delta\beta = 0$ the same function can be rewritten as:

$$h(\alpha_{\omega},\alpha_{2\omega},L) = \exp\left(-(\alpha_{2\omega}/2 + \alpha_{\omega})L\right)\frac{(\sinh(\Delta\alpha L/2))^2}{((\Delta\alpha L/2))^2} \quad \textbf{5.9}$$

with the overlap integral representing the inverse effective cross-section of the interaction being expressed as follows:

$$\Gamma = \left(\iint d(x,y) E_{2\omega}(x,y)\, E_{\omega}^2(x,y)\, dxdy\right)^2 \quad \textbf{5.10}$$

where the normalised non-linear susceptibility d(x,y) is defined as the ratio of the non-linearity of the waveguiding material (which differs from the bulk and depends on the spatial coordinates) and the effective non-linear coefficient of the material, d_{eff}. The value of the integral is given by the specific interaction, the details of the index profile and the interacting modes, with a large effective area yielding reduced conversion efficiency.

The fundamental power at the beginning of the waveguide, $P_{\omega}(0)$ and the second harmonic at the end of the waveguide can be related to the external powers P_{ω}^{IN} and $P_{2\omega}^{OUT}$ as follows:

$$P_{\omega}(0) = T_c \; T_f^{IN} \; P_{\omega}^{IN} \qquad \textbf{5.11}$$

$$P_{2\omega}(L) = \frac{P_{2\omega}^{OUT}}{T_f^{OUT}} \qquad \textbf{5.12}$$

Where T_c is the coupling efficiency into the waveguide without the Fresnel reflection loss T_f^{IN} denotes the Fresnel transmission coefficient of the fundamental at the front face of the waveguide and T_f^{OUT} represents the Fresnel transmission coefficient of the second harmonic at the end face of the waveguide.

The overall external efficiency is then defined as:

$$\eta_{\text{device}} = \frac{P_{2\omega}^{OUT}}{P_{\omega}^{IN}} \qquad \textbf{5.13}$$

If the experimental set up is not optimised for the above then a quantity called the internal normalised conversion efficiency, suggestive of the internal properties of the waveguide would be more appropriate. This internal normalised conversion efficiency which expresses the quadratic dependence of the second harmonic on the fundamental power and the guide length, is then described in units of $W^{-1}cm^{-2}$ as follows:

$$\eta = \frac{1}{L^2} \frac{P_{2\omega}(L)}{[P_{\omega}(0)]^2} \qquad \textbf{5.14}$$

substituting the value of $P_{2\omega}(L)$ from equation (5.6) then yields

$$\eta = \frac{2\omega^2}{\varepsilon_0 c^3} \frac{d_{eff}^2}{n_{2\omega} n_{\omega}^2} \; h\Gamma \qquad \textbf{5.15}$$

A maximum value of the normalised conversion efficiency is achieved for a lossless waveguide under phase-matching conditions when h equals one. However as the in-coupled fundamental power $P_\omega(0)$ is often not known because of the difficulty in determining the coupling efficiency T_c, it is more common to reference the normalised conversion efficiency to the internal fundamental power $P_\omega(L)$ at the end of the waveguide and redefine it as follows:

$$\tilde{\eta} = \frac{1}{L^2}\,\frac{P_{2\omega}(L)}{P_\omega^2(L)} = \frac{2\omega^2}{\varepsilon_0 c^3}\,\frac{d_{eff}^2}{n_{2\omega} n_\omega^2}\,\mathrm{h}\,\Gamma e^{-2\alpha_\omega L} \qquad \textbf{5.16}$$

where $P_\omega(L) = P_\omega(0)\exp(-\alpha_\omega L)$ being defined similarly as $P_{2\omega}(L)$ in equation (5.12). The redefined normalised conversion efficiency does not account for the propagation losses and hence overestimates the conversion efficiency if the guide is lossy. For a complete characterisation of the waveguide properties the effect of the propagation loss cannot be neglected and it then becomes necessary to relate the efficiency to $P_\omega(0)$. So also scaling the value in terms of the square of the waveguide length would be unjustified if waveguide non-uniformity, attenuation, thermal effects or optical damage limit the useful waveguide length (Gunter'00). The efficiency is then usually defined in terms of (W^{-1}) as:

$$\bar{\eta} = \frac{P_{2\omega}(L)}{P_\omega^2(0)} = \eta L^2 \qquad \textbf{5.17}$$

In conclusion, efficient frequency conversion is achieved only when the phase-matching condition, $\Delta\beta = 0$ is maintained. It also means that this condition should then be preserved over as long a length of the waveguide as possible for higher overall efficiencies. This then requires comprehensive information of the propagation constants as a function of waveguide parameters such as thickness and width as any discrepancy in the previously mentioned factors together with inhomogenities in the material index leads to inconsistencies in $\Delta\beta$ and hence a reduced phase-matched interaction length. The linear loss at both these wavelengths also affects the efficiency and can be reduced by identifying its origin and optimising the waveguide fabrication scheme and modifying the guide geometry for minimal loss.

If the interacting waves are not phase-matched, the second harmonic wave oscillates periodically along the guided axis due to destructive interference, with the spatial

interference pattern being defined by the factor $\sin^2(\Delta\beta L/2)$. The adjacent peaks of the interference pattern are separated by twice the coherence length, l_c, and expressed as:

$$l_c = \frac{\pi}{\Delta\beta} = \frac{\lambda_\omega}{4(n_{2\omega} - n_\omega)} \qquad \textbf{5.18}$$

In terms of the wave vector formalism the periodicity introduces an additional vector in the wavevector mismatch relation that compensates for the phase mismatch. The additional wavevector component in the wave vector mismatch expression described below, lends an added degree of freedom for achieving phase matching and by correctly selecting its value phase-matching can be achieved for any desired wavelength. The wavevector mismatch for second harmonic generation is expressed as:

$$\Delta\beta = \beta_{2\omega} - 2\beta_\omega - \frac{2\pi m}{\Lambda} \qquad \textbf{5.19}$$

where Λ, is the period of the structural variation and m is an integer which refers to the order of the quasi-phase-matched process, with the most effective conversion being achieved when the periodicity equals twice the coherence length. This type of interaction is referred to as first order quasi-phase-matching and the results in a swift build up of the second harmonic signal. Quasi-phase-matching can also be achieved by selecting a modulation period that is an odd integer times the coherence length and these interactions are hence referred to as higher order quasi-phase-matching processes. However these processes result in a much slower build up of the second harmonic along the interaction length and hence are that much less efficient compared to the first order process. For the higher order interaction processes the fabrication constraints are more relaxed as the required grating periods are much larger (factor of ×3, ×5 etc) than that required for the first order case. The short period structures required for the most efficient first order quasi phase matched conversion processes have been fabricated by an improved electric field poling technique which is discussed in the following section.

5.3 Surface periodic poling

Efficient generation of coherent blue or ultraviolet light is of immediate importance for the development of numerous applications in areas such as displays, optical data

storage and printing. The quasi-phase-matched non-linear technique described previously remains an attractive route for achieving such devices. The first order quasi-phase-matched conversion via second harmonic generation from the near infrared into the blue spectral region requires controlled periodic domain inversion with periods as short as ~2μm.

Even though PPLN with periods for some standard conversion wavelengths are commercially available, the fabrication of periodically poled non-linear crystals with arbitrarily small values of periods, specifically at the sub-micron scale, still remains almost unachievable with the standard poling technique. The high value of the coercive field in congruent lithium niobate in addition to the inherent non-uniformities and defects that always exist in the commercially available crystals restricts the applicability of the electric field poling technique, confining it in practise to the limits of around 5μm for commercially available samples with thickness of 300-500μm.

Some researchers have circumvented this aspect ratio constraint, by polishing the crystals down to a thickness of order 100-150 μm with the aim of achieving finer periods (Kintaka'96a & Yamada'98). An alternative approach referred to as controlled back switched poling was demonstrated (Batchko'99) to achieve periods of 4μm and further refined (Shur'00a) to achieve even shorter periods of 2.6μm.

Alternatively, use of multiple short current pulses during poling has been employed to achieve domain inversion in MgO: LN, which is less susceptible to photorefractive damage. Periods as short as 2.2μm and depths of 1.5μm in combination with waveguide geometries have been achieved (Sugita'01).

Moreover there is great difficulty involved in maintaining such a high aspect ratio, short period and high quality domain structure over large areas and unnecessarily large depths greater than the waveguide depths. For typically employed waveguide geometries, this inversion depth is potentially sufficient, as the waveguiding regions are of similar depths

A different approach referred to as surface poling or *over-poling*, forming an important contribution of this thesis is now described (Busacca'02). With this

modified electric field poling approach surface domain inversion with periods as short as 1μm has been achieved. The depths of the observed surface domains have been seen to vary from a few μm to around 10μm.

5.3.1 The experimental procedure

The technique of surface domain inversion is based on the conventional electric field poling at room temperature. The initial procedures involved are similar to the conventional poling method and includes spin coating one of the z faces of the sample with a photoresist and subsequent definition of the desired periodic pattern within the photoresist using standard photolithography. Instead of defining the periodic structures in metal layers or combinations thereof employed by other researchers, the desired periodic patterns were initially defined within a positive photoresist spun on to the lithium niobate samples. Moreover for the entire surface poling study, –z faces of the lithium niobate samples were photolithographically patterned.

As described briefly in section 3.5.6, in order to employ the conventional electric field poling technique it is necessary to work out the charge Q (= 2 × A × P_S), corresponding to the patterned areas wherein domain inversion is to be achieved. As in all the studies performed, a positive photoresist was spun on the -z faces of z-cut lithium niobate samples; the area 'A' then corresponds to the developed areas (exposed areas on the crystal face and hence the contact area with the conductive liquid gel) of the pattern defined in the photoresist.

The above-defined charge relation does not account however for the variations in the supplier dependent material stoichiometry, variations in the crystal thickness along the patterned areas and specific electrical characteristics of the voltage supply employed in poling. The charge-relation can be corrected to account for the above, by multiplying the right hand side of the same equation by a factor (referred to as the empirical factor, EF), hence resulting in a different value of the calculated charge Q, defined by

$$Q = 2 \times A \times P_S \times EF$$

In conventional poling experiments an empirical factor value slightly exceeding unity (around 1.1 to 1.4) is often used to achieve the desired uniform periodic inversion, with the appropriate value established after repeated trial and error attempts.

As the duration of the applied electric field is governed by the recalculated value of the charge Q, it is then obvious that the duration of the applied electric field is a function of both the area A to be poled and the empirical factor EF. The empirical factor in effect governs the poling process and plays a major role in determining the spatial profile of the periodic structure transferred by the poling step into the crystal. The ferroelectric domains are known to nucleate near the edges of the periodic electrode patterns on the patterned face, and then grow (Shur'00b,'99a, 99b) towards the opposite face of the crystal. Adjacent domains then coalesce leading to the formation of laminar domain walls extending into the entire volume of the crystal. The domains thus defined in the crystal by the domain walls further spread beyond the photolithographically pre-defined areas into the adjacent areas under the insulating resist (Missey'00, Pruneri'95, Myers'95, Yamada'93). Correct termination of the poling voltage pulse can thus prevent this undesired lateral domain extension into neighbouring regions. The empirical factor thereby effectively controls domain spreading within the crystal volume.

For EF values less than unity, domain inversion occurs preferentially in areas where nucleation is easier, for example in areas of increased roughness, leading to the under-poling situation represented in figure 5.1a. Figure 5.1.a depicts these under-poled areas, (not covered by the insulating resist, and hence the areas to which the field was applied) which have not been inverted by the application of the poling pulse in green.

For an empirical factor value ~1, normal poling would be expected with a large-scale uniformity over the entire patterned region, as shown in figure 5.1b. A uniform periodically poled structure with the same mark to space ratio as that of the patterned photoresist layer should ideally be achieved.

If the empirical factor is set to a much larger value than unity, however, then in this over-poling regime, the inverted domains continue to spread laterally, extending their volume more rapidly than required for an ideal 50/50 mark to space ratio grating. The spread of these inverted domains is controlled however by the presence of surface

charge trapped below the periodic insulating resist layer, which has the effect of slowing down the motion of the domain walls (Miller'98) in this surface region. The resultant poling achieved via employing higher values of the empirical factor for poling is depicted in the schematic 5.1c, showing a small amount of material beneath the photoresist which still maintains its original poled state within the otherwise entirely inverted sample. This technique however has the effect of producing large-scale periodic structures just beneath the patterned surface, with domain orientation opposite to that of the bulk sample, and as expected with a periodic structure having a different mark-to-space ratio from that imposed in the photoresist. The periodic structures formed on over-poling the lithium niobate samples however are not visible when observed between cross-polarisers as the entire sample appears uniformly poled, but may be subsequently revealed by brief etching of the sample in HF acid. The over-poling technique described above thus takes advantage of the undesired effect of lateral spreading and merging of the inverted domains beneath the photoresist for fabrication of periodic surface structures extending to useful depths of a few microns. The surface poling technique however would not work when metal electrodes are used to impose the periodic pattern, as charge accumulation below the metal electrodes would thereby be prohibited.

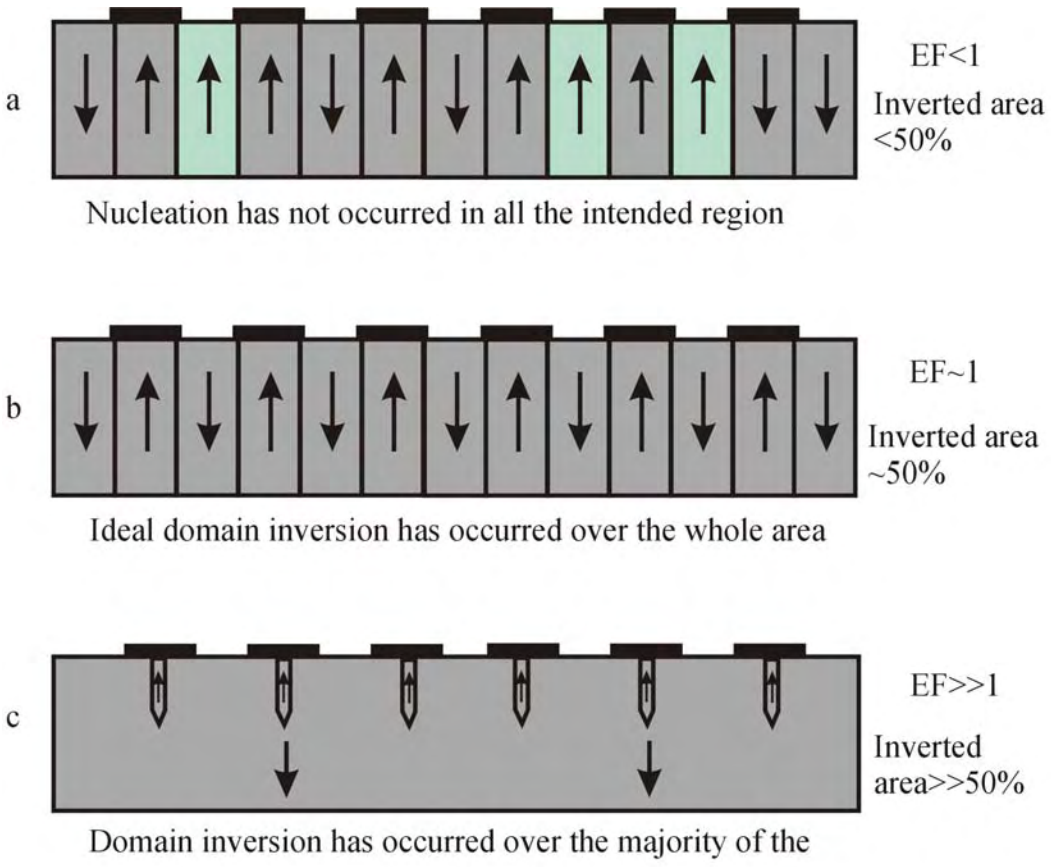

Figure 5.1 Schematic explaining the poling process as a function of the empirical factor used during poling. (a) Underpoling with EF < 1, (b) Normal poling with EF ~ 1, and (c) Overpoling or surface poling with EF >>1

5.3.2 Experimental results and studies to control over-poling

The -z faces of several lithium niobate samples, with thickness of 300 and 500μm, supplied by Crystal Technology, USA and Yamaju Ceramics, Japan, were spin coated with a positive photoresist (Shipley, S-1813) layer of ~1μm and subsequently photolithographically patterned with masks with gratings having periods ranging from 2.47-4μm. A few samples were also patterned with much shorter periods, achieved via an interferometric technique exposing the resist layer with a laser through a phase mask. The patterned samples were then poled by the already discussed over-poling technique, using different empirical factors >>1.

Typical traces of the poling current for a corresponding single voltage pulse as displayed on the oscilloscope in the external poling circuit are shown in fig 5.2. It can be easily inferred from the characteristic current and voltage signatures observed during over-poling that this mechanism is fundamentally different from the backswitching mechanism described in (Batchko'99 & Shur'00), wherein current flow in opposing directions is observed during the poling process.

A range of different overpoling factors from 2-12 was used for these poling studies and the same surface effect was observed in each of the over-poled samples. Figure 5.3 shows the –z face and the y face of a sample with domain periods of 2.47μm, briefly etched in a mixture of HF and HNO_3. Figures 5.4 shows an image of a lithium niobate sample with a similar domain period of 2.47μm but surface poled with different values of EF. The SEM image in figure 5.5 shows the shape of the surface domains as seen on the etched y face of a sample with domain periods of 6.5μm. The sole purpose of etching the sample in each case was to visualise the periodically inverted structure.

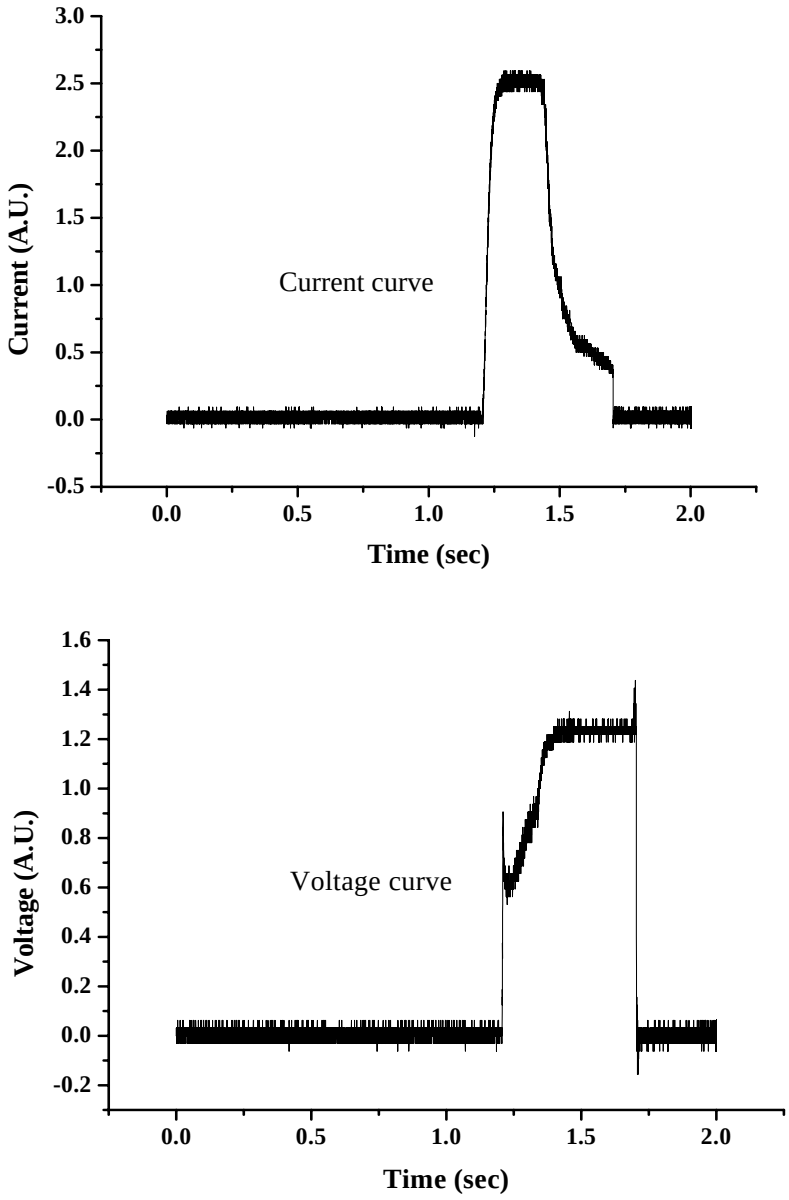

Fig 5.2 Typical single pulse poling signatures for the poling current and poling voltage as recorded on an oscilloscope

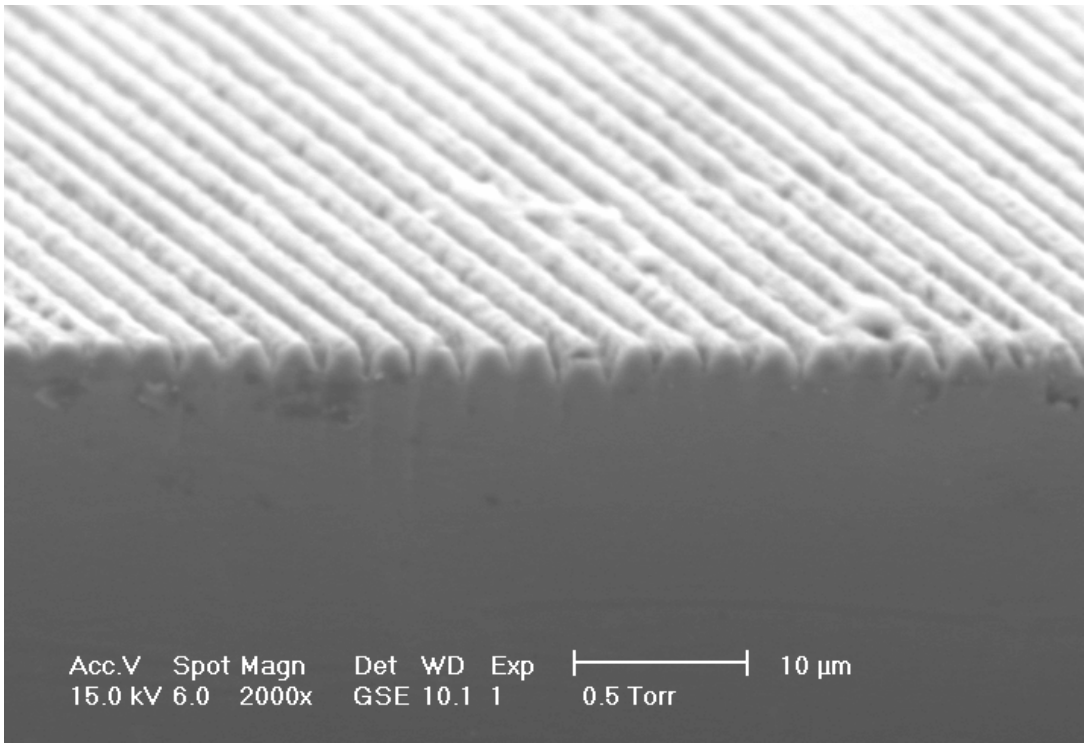

Figure 5.3 SEM image of an etched –z face of an over-poled sample having a period of 2.47µm

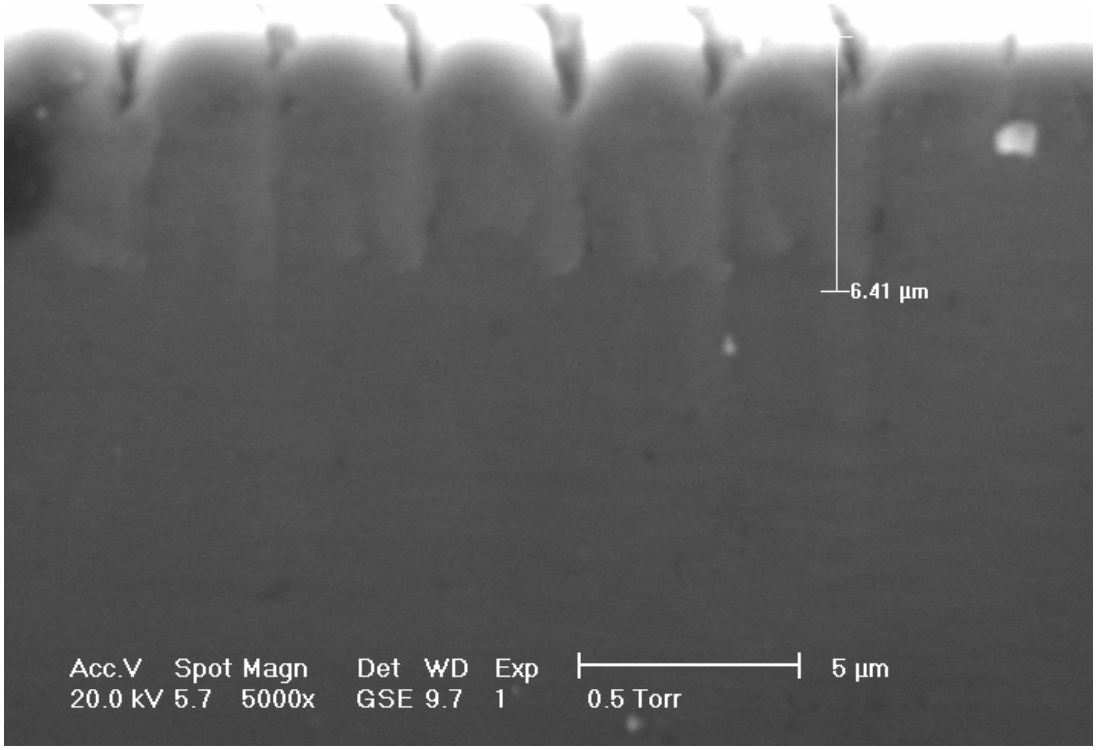

Figure 5.4 SEM image of the y face of a sample (with period of 2.47µm) showing the surface domains extending to depths of ~6.4µm

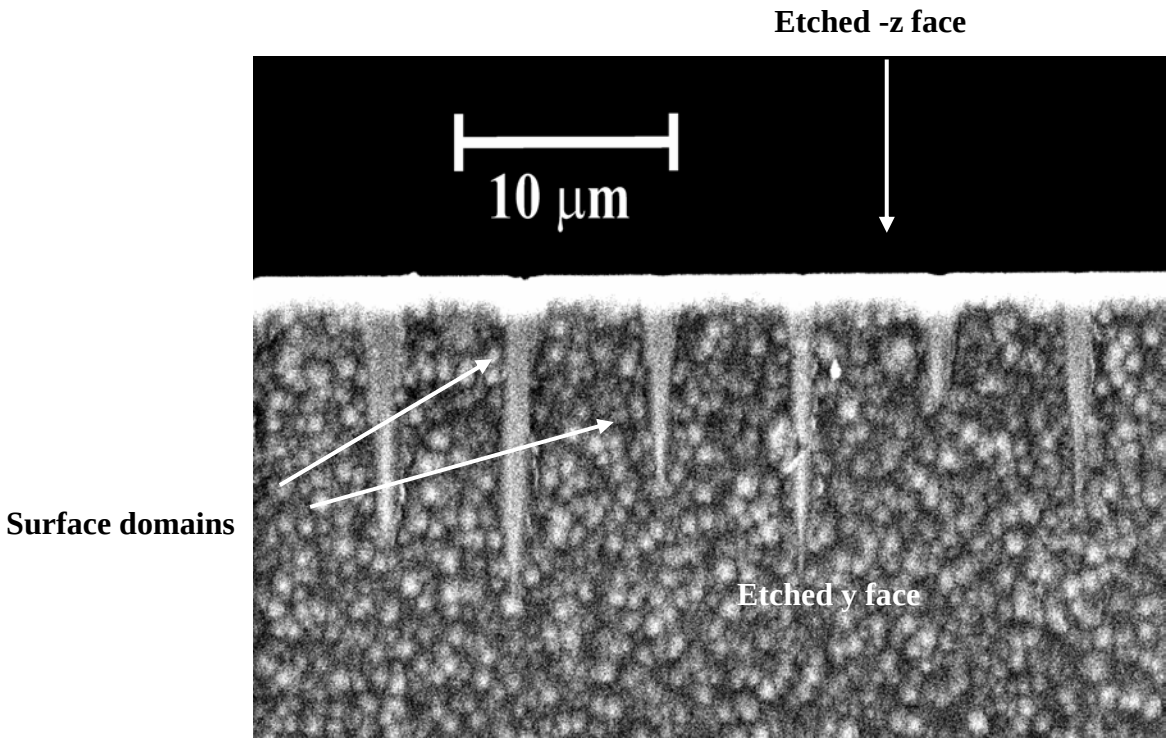

Figure 5.5 SEM image of the y-face of an etched sample (with periods of 6.5μm), showing the typical shapes of the surface domains

For the range of different empirical factors experimented with for the over-poling study, domains were seen to exist only in the near-surface region, with differing depths however, which required a parametric study to establish a link between the depth and the uniformity of these surface domains as a function of the empirical factor employed in over-poling and the period of the structures defined photolithographically in the photoresist before poling. An initial parametric study to establish a relation between them revealed a clear inverse functional relationship between the empirical factor employed in over-poling and the depth of the surface structures. Moreover the depth of the surface domains was also observed to be a function of the period of the structures pre-defined in the photoresist. The plot in figure 5.6 shows the results of the measured domain depths as a function of the period of the pattern photolithographically imposed in the resist (prior to over-poling), for one specific value of the empirical factor (which in this case was 8). The resist on the –z faces of three different 500μm thick samples was periodically patterned with periods of 2.57μm, 3.14μm and 4.05μm respectively and then over-poled with an empirical factor value = 8. The poled samples were then diced along the periodic

structures (along planes parallel to the y faces and perpendicular to the z-faces), polished and finally etched in the acid mixture to observe the presence of surface domains. The depths of the surface domains in each case were then measured with an optical microscope.

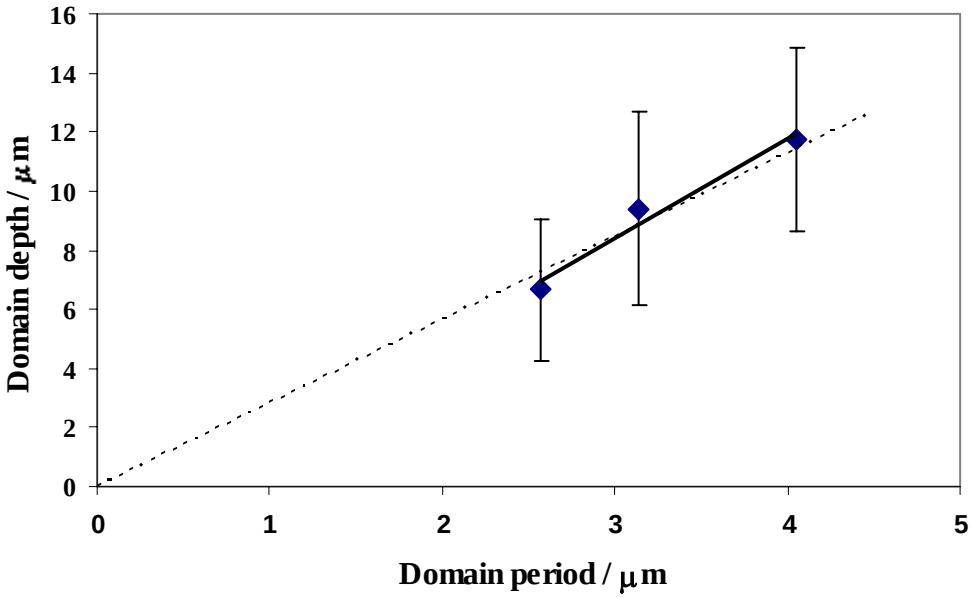

Figure 5.6 Plot showing the variation of the domain depth with domain period for an EF=8

As seen above even though the variation in the measured domain depths (measured for 30-100 periods) is somewhat large, the minimum depths achieved is sufficient for the required overlap with waveguiding regions. Moreover, as the mean depth is observed to scale approximately linearly with the period, for applications that require sub-micron periodicity, this again proves useful as the overlap between the guided modes and the domain-inverted regions is a prerequisite for efficient non-linear interactions. The close agreement between the gradients of the two plots (namely the dashed line which implicitly includes the point (0,0) and the solid line which just includes the three points corresponding to the three periods) in figure 5.6 further justifies the suggested approximately linear relation between these two variables.

Sub-micron periodicity through the entire bulk of wafer samples is generally considered to be un-achievable with the conventional bulk electric field poling technique because of the stringent aspect ratio demands. As shown in figure 5.7 however, which is the SEM image of the etched –z face of an over-poled lithium niobate sample, we can clearly see a surface grating with a periodicity of ~1μm. The

sub-micron periodic pattern was previously defined in the photoresist by illumination via a phase mask and Excimer laser radiation, at 248μm. This interferometric exposure technique via a phase mask or two-beam interferometry is an ideal approach when domain patterning down to periods of 0.3 μm required for backward wave interactions at wavelengths of 1.5 μm and for other applications such as photonic crystals where sub-micron features are required.

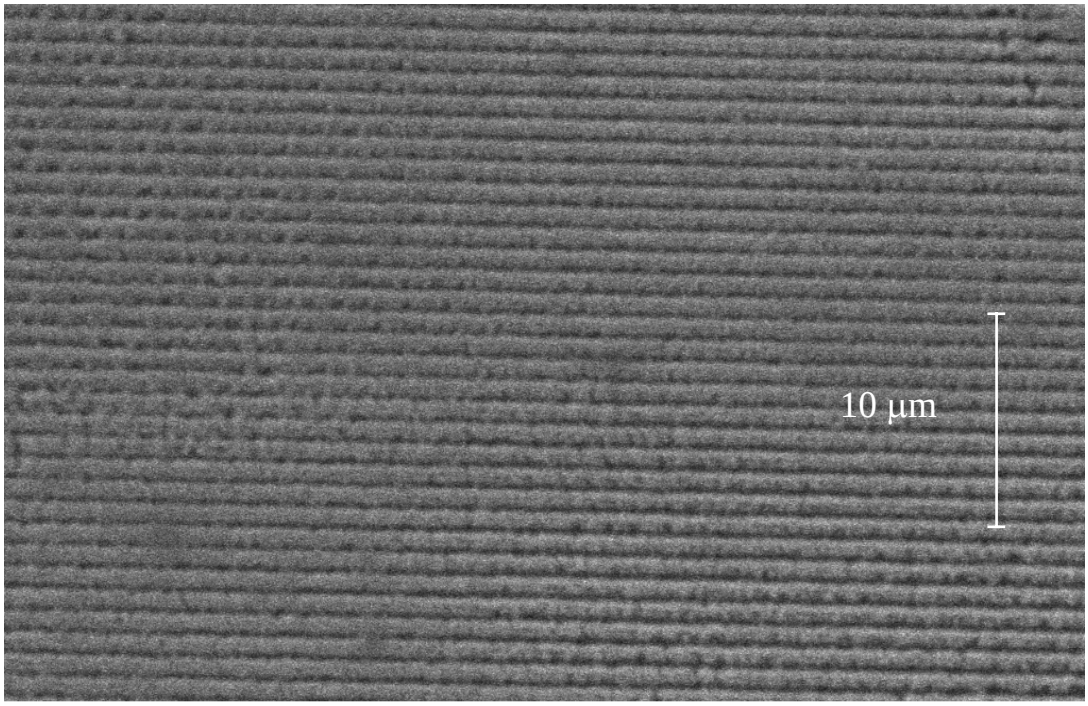

Figure 5.7 Optical microscope image of the etched –z face of a sample with 1μm periodic structure

5.3.3 Surface poling results for samples with predefined waveguides

In order to assess the compatibility of the over-poling technique with standard waveguide fabrication techniques in lithium niobate such as Ti-indiffusion and proton exchange, over-poling of samples with predefined waveguide structures was attempted. Ti-indiffused channel waveguides with widths of a few microns were fabricated on the –z faces of 500μm thick z-cut lithium niobate samples by indiffusion at an elevated temperature of 1050^0C for a period of 11 hours. A Ti film was thermally evaporated on to the patterned –z face and the channel waveguides were

subsequently defined by a lift-off step. The –z faces of the samples with the indiffused channel waveguide were then spin coated with a photoresist, photolithographically patterned and over-poled using different empirical factors. Similar trials were also conducted with proton-exchanged waveguides. The poled samples were briefly etched in HF acid to reveal the periodically poled structures. Figure 5.8 and 5.9 are optical microscope images of the etched –z faces of two different samples; one depicting a surface poled proton exchanged waveguide and the other with a surface poled Ti – indiffused waveguide. The spread of the surface domains all across the extent of the waveguides was confirmed by ion beam milling of a surface poled sample with predefined Ti-indiffused channel waveguides. Figure 5.10 shows the etched –z face of a milled sample showing the surface domains with a periodicity of 6.5 μm extending all through the channel waveguides.

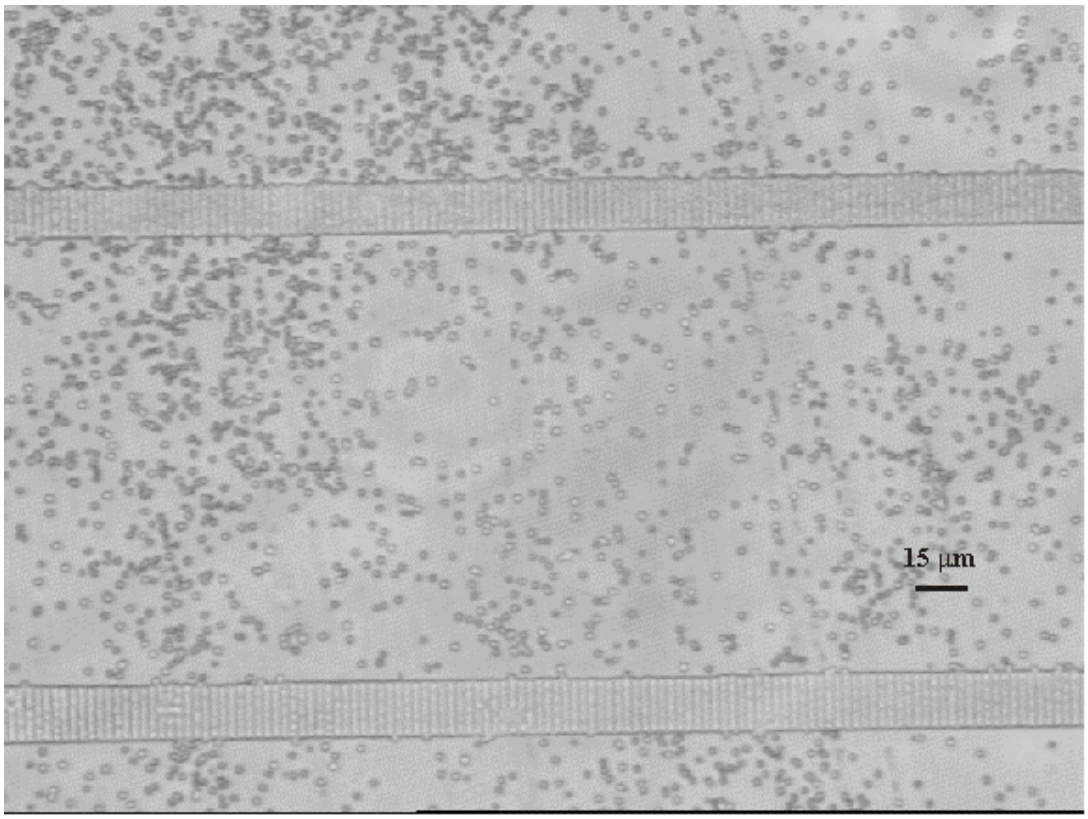

Figure5.8a. Optical microscope image of the etched –z face showing over-poled annealed proton exchanged waveguides.

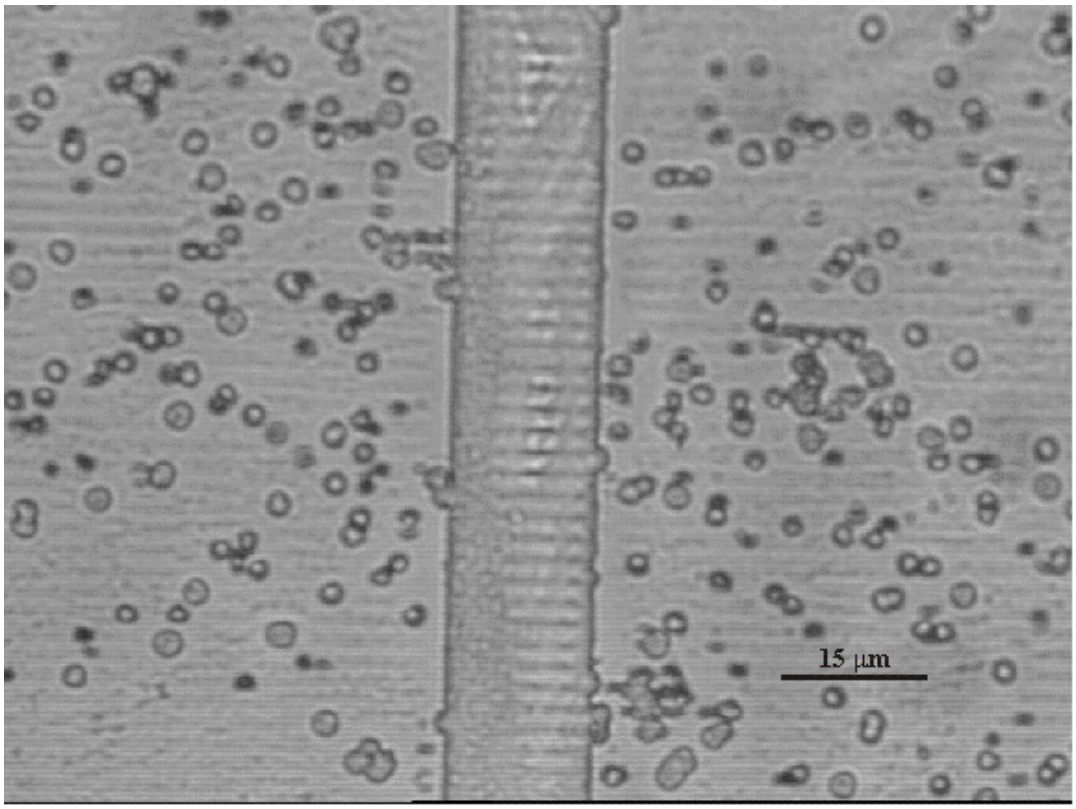

Figure 5.8b Magnified image of one of the proton exchanged waveguide shown in figure 5.8a.

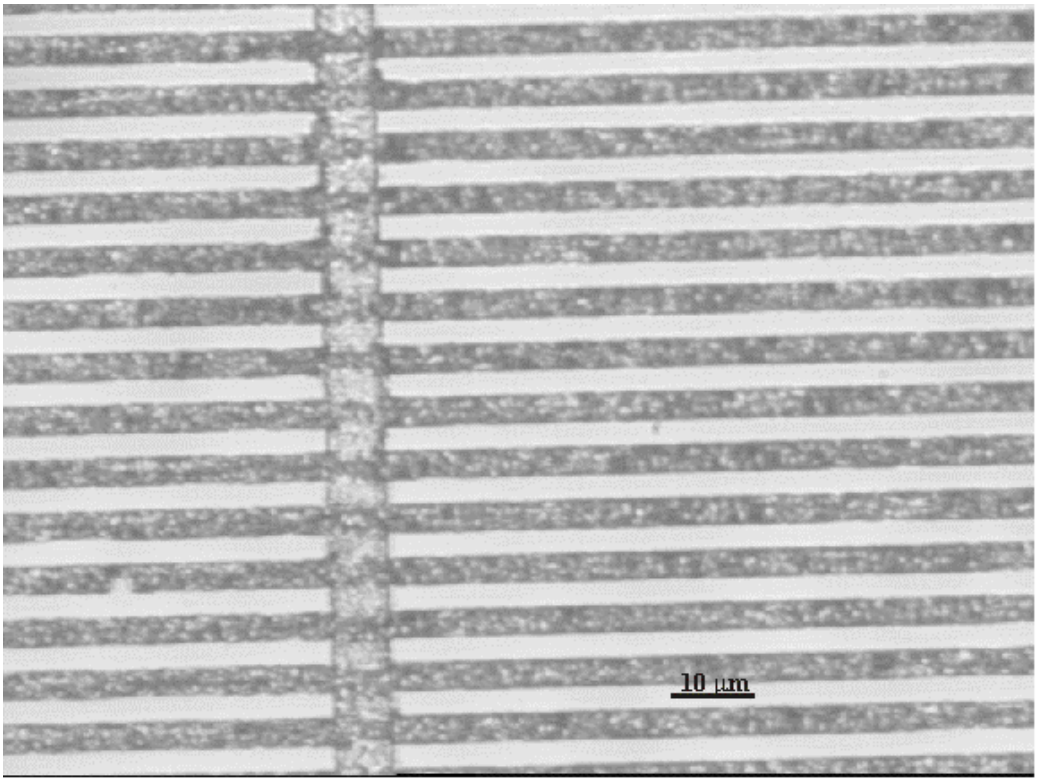

Figure 5.9a Optical microscope image of the etched –z face of a surface poled sample showing the periodically poled structures and extending all across the image and the single Ti-indiffused channel waveguide.

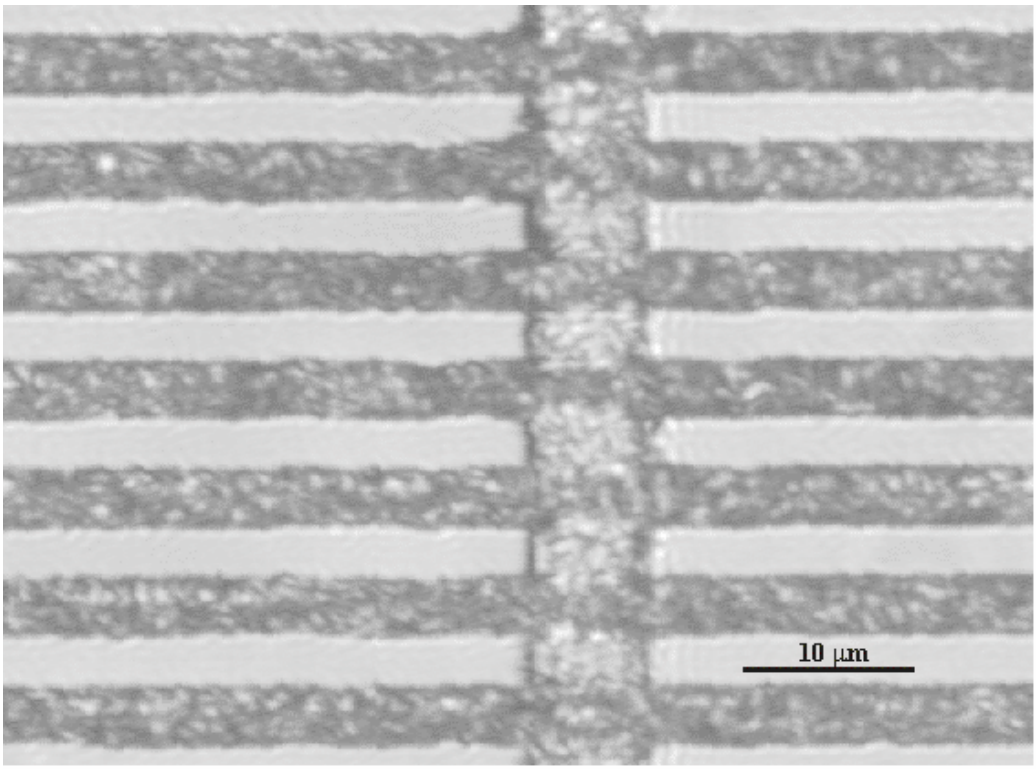

Figure 5.9b Magnified image of the over-poled Ti-indiffused channel waveguide shown in figure 5.9a

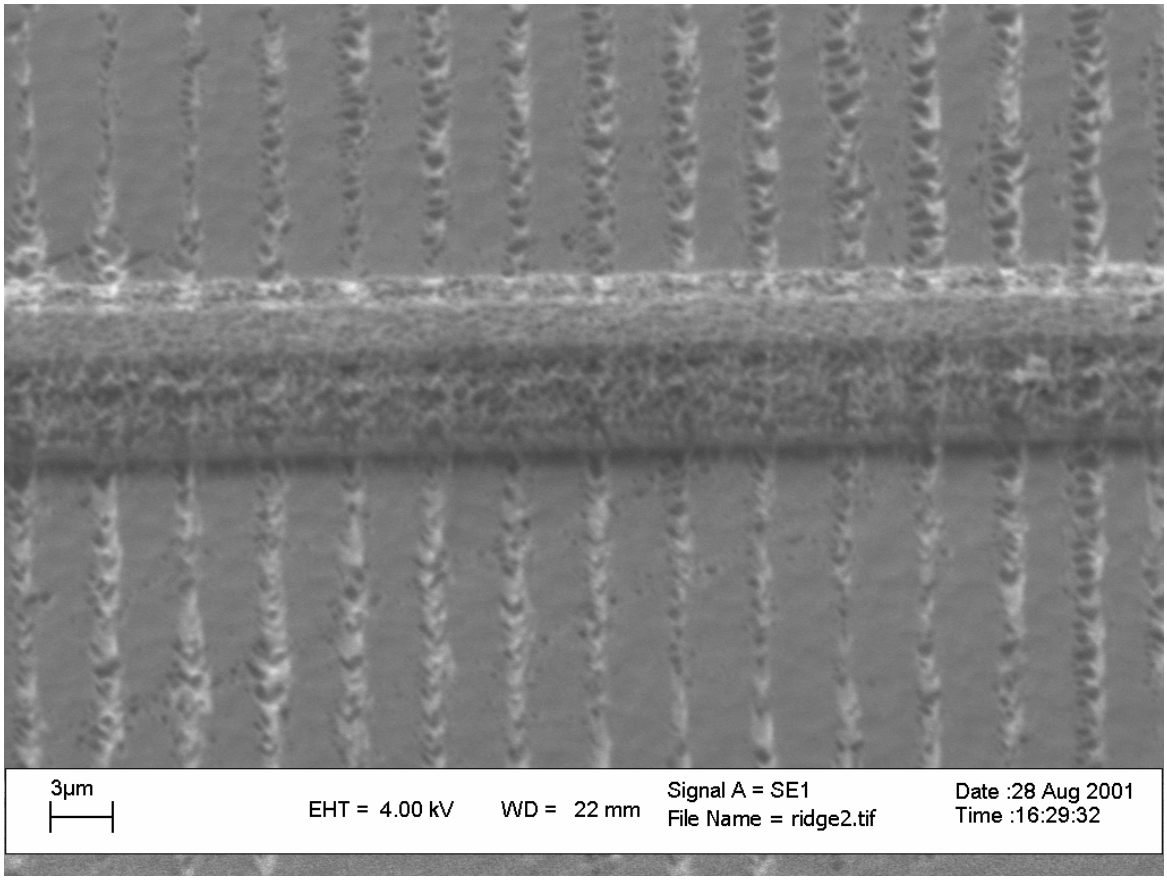

Figure 5.10 SEM image of an etched –z face, showing a ridge waveguide and inverted surface domains extending through the waveguide depth.

5.3.4 Surface poling and 2-D structures

The usefulness of the surface poling technique to engineer two-dimensional structures in lithium niobate was also investigated to gauge the range of applicability of the poling technique. The expansion of periodically poled lithium niobate structures into two-dimensional geometries (Berger'98, Chowdhury'00&'01, Saltiel'00, Sterke'01) has successfully been demonstrated for both single and cascaded non-linear interactions on the same sample in bulk hexagonally poled lithium niobate (Broderick'00). As the application for two-dimensional poled waveguide structures would yield enhanced non-linear interaction efficiency because of tighter mode confinement (Gallo'03), it was obvious to try and fabricate such periodic two-dimensional structures using the over-poling technique.

The possibility of expanding the operation of the two-dimensional domain structures to shorter wavelengths would also be an interesting application. However the apparent

discussed shortcomings of the conventional electric field poling technique in fabrication of such shorter periods render this technique useless. The modified (over-poling) technique with its proven ability of sub micron domain inversion and waveguide compatibility was therefore tried to fabricate such short period two-dimensional hexagonally poled periodic structures in lithium niobate with predefined planar annealed proton exchanged optical waveguiding region.

The –z faces of congruent z-cut lithium niobate were spin coated, photolithographically patterned with periodic hexagonal patterns (with different pattern periods) and over-poled with different empirical factors values from 3-8. While imprinting the hexagonal pattern on the photoresist it was ensured that one of edges of the hexagonal structure was aligned along the y-axis of the crystal. This established routine of aligning that side of the pattern in the periodic structure (defined in the photoresist) with the longest dimension along the crystallographic y-direction of the lithium niobate samples produces greatly improved poling results. The observed greater uniformity achieved in general with hexagonal structures could be attributed to the tendency of the domain walls to align along the crystals hexagonal symmetry (He'03). Figure 5.11a is the SEM image of the etched –z face of a surface poled sample with a uniform two-dimensional hexagonal structure with a pattern period of 7.6μm. Figure 5.11b is a further magnified image.

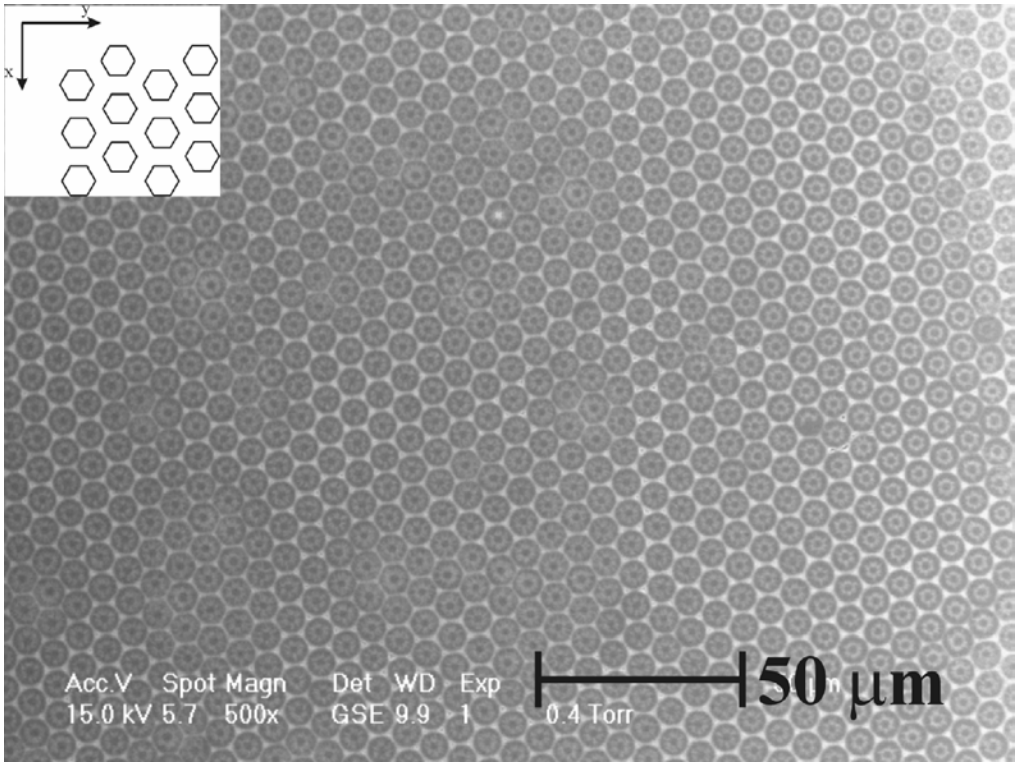

Figure 5.11a SEM image of the etched –z face of a samples over-poled with an empirical factor = 8, showing the two-dimensional pattern with a periodicity of 7.6µm

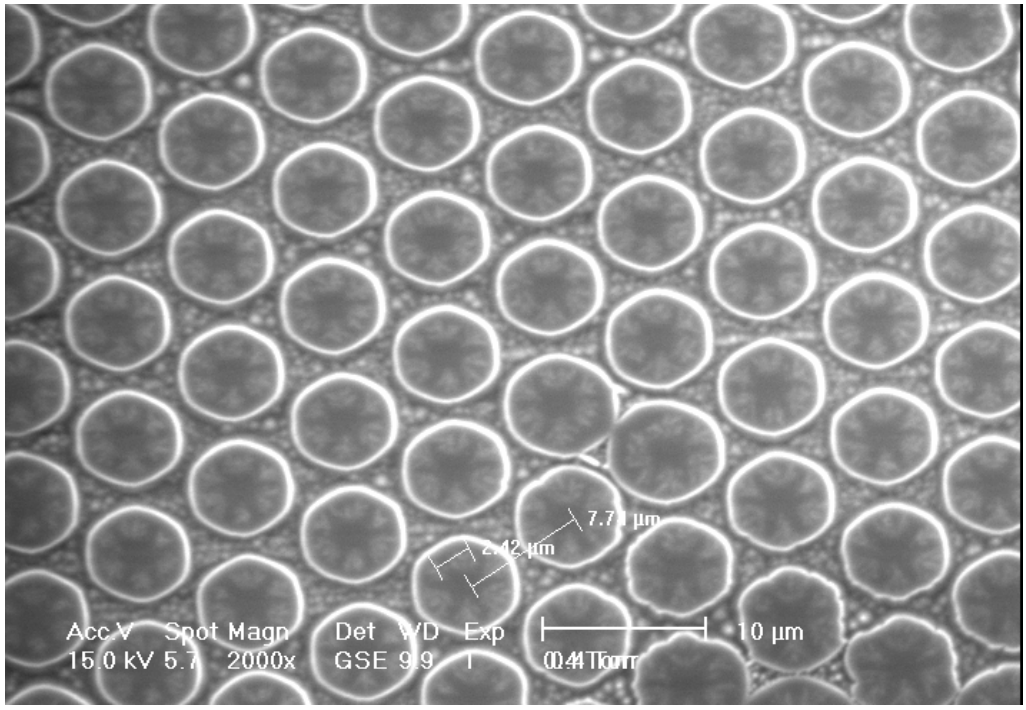

Figure 5.11b SEM image showing a closer view of the same features

The versatility of the surface poling technique was further ascertained by employing such poled waveguide structures for wavelength conversion processes such as second harmonic generation. The following sections describe such attempts with a surface poled Ti-indiffused channel waveguide for first order quasi-phase matched second harmonic generation and a surface domain-inverted planar annealed proton exchanged waveguide for second harmonic generation.

5.4 Non-linear experiments with surface poled hexagonal annealed-proton-exchanged waveguide structure

A planar waveguide was fabricated on the –z face of a z-cut 500μm thick sample of congruent lithium niobate sample by the annealed proton exchange technique described elsewhere (Bortz'91). A shallow (~0.2μm) proton-rich surface layer was formed by a first exchange at 160^0C in pure benzoic acid, followed by annealing for a few hours at 330^0C in air to diffuse the protons deeper into the substrate (to a depth of around 2.2μm). The annealing step also partially reduced the crystal damage and hence the loss in the non-linearity induced by the previous proton exchange step. The waveguide fabrication steps with the corresponding extraordinary refractive index profile are depicted in figure 5.12 shown below. The waveguide structure was fabricated to support only the fundamental mode at the fundamental wavelength of 1.064μm of the Nd: YVO_4 laser source which was used for second harmonic generation described later in this section.

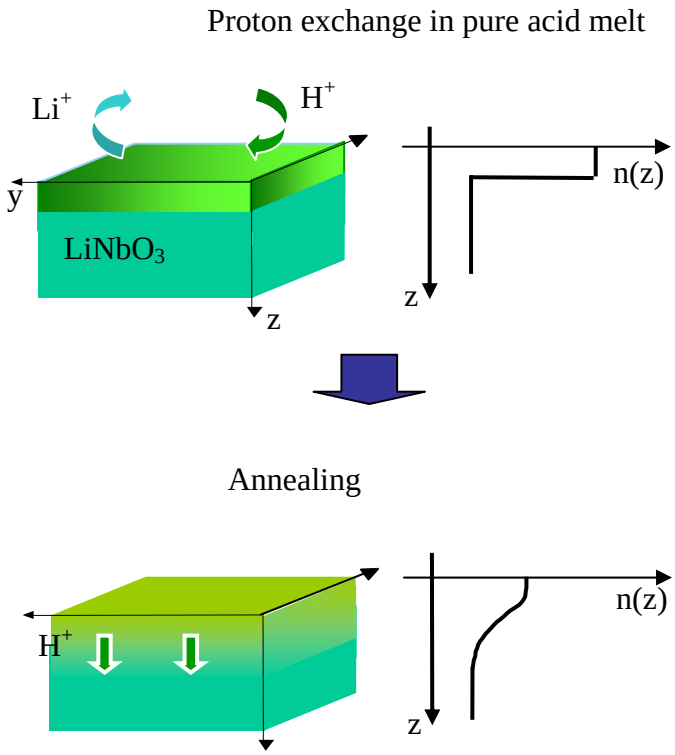

Figure 5.12 Schematic of the fabrication steps for the annealed proton exchanged planar waveguide on z-cut lithium niobate

A two-dimensional periodic pattern with a periodicity of 7.6μm was defined in the spin-coated photoresist above the formed planar annealed proton exchanged region on the –z face of the sample. The two dimensional periodic pattern was transferred into the waveguiding region by the subsequent over-poling step. The empirical factor used for poling the samples was 8. The quality of the pattern created was assessed by etching samples poled with an identical empirical factor but without a predefined waveguide within it. Figures 5.11a and 5.11b are SEM images of one such sample.

For the quasi-phase-matched second harmonic generation experiment a diode pumped Nd: YVO_4 laser was used as the pump source for the fundamental wavelength. The polarisation of the laser beam was controlled using a half-wave plate thereby exciting a TM mode into the planar proton exchanged waveguide. The laser beam was coupled into the waveguide using a microscope objective (with a NA=0.25, focal length of 16.9mm and a working distance of 6.8mm), which focussed the beam at the polished end face (x-face) of the crystal. To tune the device to achieve the phase matching condition, the sample was mounted on a heating element which was driven by a

feedback stabilized power supply for temperature stability between 20^0C and 150^0C. The output form the other end face of the waveguide was imaged on a CCD detector by a second microscope objective and subsequently analysed using beam analysis software. A colour filter placed between the objective at the output end and the camera served to separate the fundamental radiation from the second harmonic allowing only the latter to reach the detector. As the transmission of the filter at the harmonic wavelength of 532nm was 75% the measured second harmonic power was corrected to account for this.

The sample was temperature tuned to achieve the quasi-phase-matching condition. The obtained temperature tuning curve shown in figure 5.13 has a FWHM of the order of 3.5^0C. The temperature tuning curve has quasi-phase matching peak at 105.5^0C and the internal conversion efficiency of the quasi-phase matched second harmonic generation process was 0.145 %/Wcm^2.

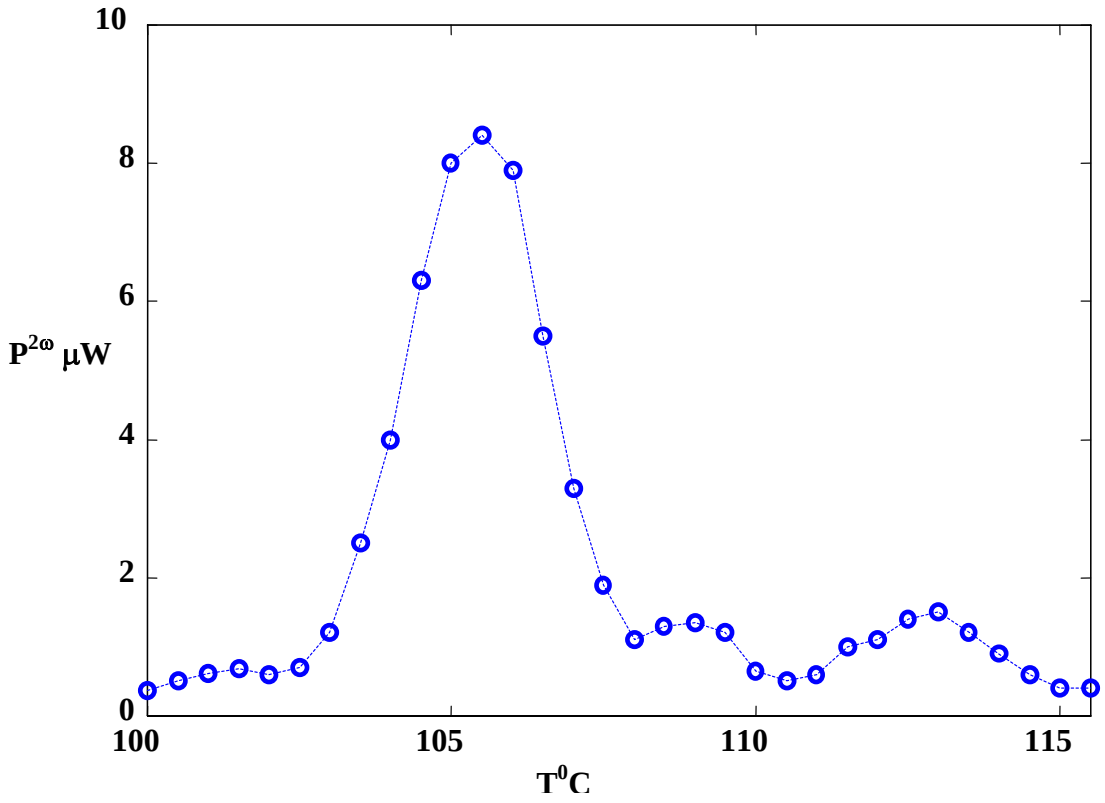

Figure 5.13 Quasi-phase-matched second harmonic generation temperature tuning curve for the planar annealed proton-exchanged waveguide with surface poled hexagonal structures

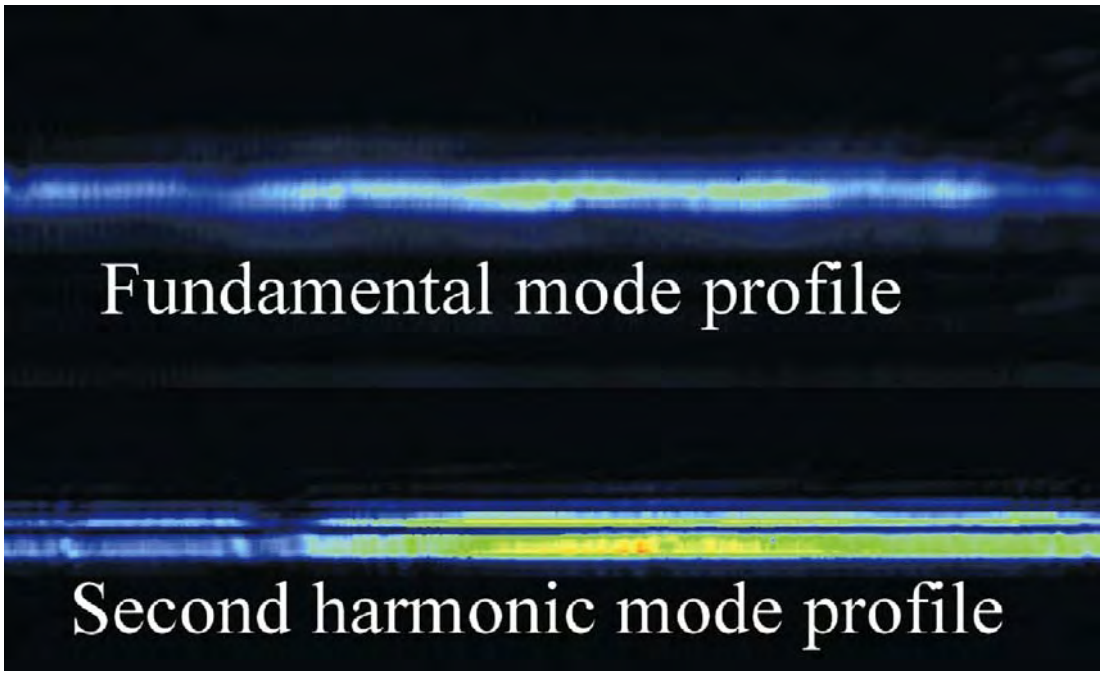

Figure 5.14 Waveguide profiles of the fundamental and the second harmonic mode propagating in the planar annealed proton exchanged hexagonally poled waveguide

From the waveguide profiles of the fundamental and the second harmonic shown in figure 5.14, it can be inferred that the TM_1 mode of the generated second harmonic propagates through the waveguide structure. With the mask used to fabricate the hexagonal pattern (in the photoresist) designed to phase match bulk collinear second harmonic generation process from 1.064μm with the G_{10} vector the interaction with the TM_1 waveguide mode at 532nm appears to be closer to the bulk phase-matching condition than that involving the TM_0 mode. Moreover the waveguide fabrication process is known to reduce non-linearity near the surface of the sample and hence result in a poor overlap between the TM_0 mode of the fundamental and the second harmonic. This problem of induced surface damage can be alleviated by use of the soft proton exchange technique (Chanvillard'00) and use of such a waveguide structure in combination with optimised hexagonal pattern periods could result in better non-linear interaction efficiency.

To further ascertain the compatibility of the surface poling technique with the Ti-indiffused waveguide fabrication procedure we attempted a similar non-linear second harmonic generation experiment with Ti-indiffused channel waveguides with periodically inverted surface structures formed by the over-poling process**.**

5.5 Non-linear experiment with surface periodically poled Ti-indiffused channel waveguides

Channel waveguides spaced 100μm apart and oriented parallel to the crystallographic x-direction, with widths varying from 1.5 μm to 8 μm were fabricated by a thermal diffusions on the –z face of 500 μm thick 30mm long z-cut lithium niobate samples. A 100nm thick titanium film was thermally evaporated on to the –z face of the sample and in-diffused in an oxygen atmosphere at a temperature of 1050^0C over a period of 11 hours. Several sets of 12 evenly spaced channel waveguides were fabricated on the same substrate**.**

The –z face of the samples with the in-diffused channel waveguides was then photolithographically patterned with a 0.7 mm wide and 20 mm long grating structure having a grating period of 2.47μm and was poled using the method for surface domain inversion with an empirical factor 6. The periodic pattern defined on the photoresist had a mark-space ratio 60-40. As the pattern was 7 times wider than the separation between consecutive channels several of them lie inside the periodically poled area.

With surface poling the need to polish off the shallow Li_2O out-diffusion induced domain-inverted layer usually formed on the +z face (Schreiber'01) during the high temperature metal diffusion is not required. This unavoidable polishing step, which would ensure the domains to be unidirectional, can however have an undesirable effect on the poling, as it could well lead to a variation in the thickness of the sample.

The end-faces of the waveguides were then polished for further characterization, leaving the samples 20mm in length. To confirm whether the waveguides were single moded in the spectral region of interest of around 800 nm and 400 nm a near infrared camera was used to study the mode profiles. The waveguide losses at the fundamental and harmonic were estimated to be around 0.5dB/cm.

A cw tunable titanium sapphire laser was used as a pump source for the QPM SHG experiments. The beam was coupled in and out of the polished end faces of the channel waveguides by two separate microscope objectives (with a NA=0.25, focal length of 16.9mm and a working distance of 6.8mm). The output was imaged using the microscope objective on the surface of the detector and the second harmonic was separated from the fundamental radiation by using a high-pass coloured glass filter.

During the experiment the sample was kept at a temperature of 205° C in order to avoid possible photorefractive damage generated either by the fundamental or the second harmonic radiation.

Second harmonic generation was studied from various waveguides with the most efficient blue light generation observed from a 2.5μm wide channel waveguide poled with a period of 2.47μm. To take advantage of the highest non-linear tensor coefficient d_{33}, which is along the z-direction the incident fundamental light beam was TM-polarised. Near-field waveguide mode profile monitoring showed that this waveguide could support only the lowest order TM mode in the range of the fundamental wavelengths (λ~ 825 nm). The wavelength-tuning curve was acquired by measuring the power of the second harmonic as a function of the fundamental wavelength and is depicted in figure 5.15. Two different sets of peaks can be identified in the tuning-curve, with an intense set centred at 412.6 nm corresponding to conversion from the lowest order waveguide mode at the fundamental wavelength (TM_0^{ω}) to the lowest order mode of the second harmonic ($TM_0^{2\omega}$) and a second set of peaks at lower wavelengths corresponding to coupling to a higher order waveguide mode at the second harmonic wavelengths. The weaker second set of peaks present in the tuning curve could possibly have resulted from Fourier artefacts and periodic waveguide irregularities.

The maximum measured second harmonic power for the $TM_0^{\omega} \rightarrow TM_0^{2\omega}$ interaction centred at 413.17nm was 3.46mW for 70mW of pump power. These values were uncorrected for Fresnel losses (14 %) and filter transmission (70%) and hence correspond to an absolute conversion efficiency of 4.9 % / *W*, or a length normalised efficiency of 17.6 % / Wcm^2 (for a corresponding length of 2cms), or an effective length normalised efficiency of 119 % / Wcm^2 (for an effective length of 0.77cm deduced from the tuning curve).

The slightly non-symmetric shape of the tuning curve about the phase-matched wavelength could be as a result of the variation in the index of refraction along the length of the waveguide or alternatively an irregularity in the inverted domain pattern. The fabrication imperfections in such non-optimised devices are known to lead to decreased conversion efficiencies (Fejer'92). The second harmonic power is known to be also affected by even a slight variation in the mark-to-space ratio of the periodic

structure (Kintaka'96) and theoretical calculations with different mark-to-space ratios ascertain a drastic drop in the efficiency with a change in the ratio from 50-50 to 80-20.

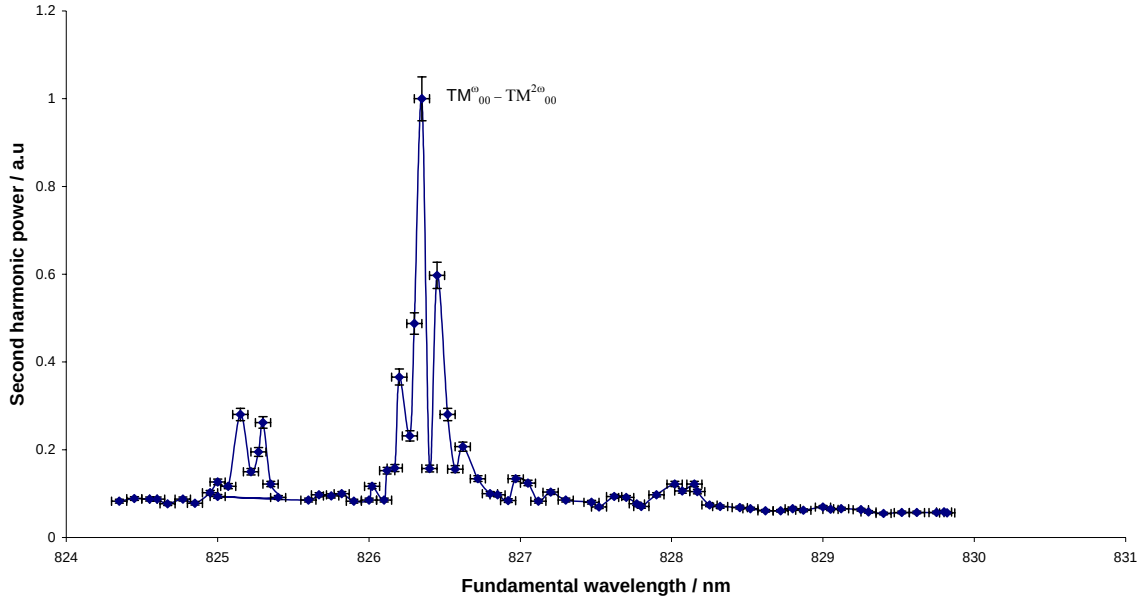

Figure 5.15 Wavelength tuning curve for the quasi-phase-matched second harmonic generation from an over-poled Ti-indiffused channel waveguide.

However this is only a first demonstration showing the potential application of such a scheme, which employs surface inverted domains for first order quasi-phase-matched waveguide interactions. All factors, which limit the performance of the device, are subject to optimization so that more efficient devices with superior characteristics can be fabricated in the future.

The lower value of the efficiency reiterates the fact that over-poling results in a non-ideal mark-to-space ratio which is quite different from the desired 50-50. Brief etching of the over-poled samples have revealed such non-ideal structures (seen in figure 5.3).

5.6 Attempts to achieve the ideal mark-space ratio

The research focus was then shifted to try to optimise the surface poling technique to achieve periodically poled structures with an ideal 50-50 mark-to-space ratio and hence high non-linear interaction efficiencies. It is obvious from the preceding

discussion that the two major factors that would govern the mark-to-space ratio of the periodically poled structure would be the actual mark to space ratio of the periodic pattern defined in the photoresist and the employed empirical factor. Trials were conducted to see how variation of these parameters would actually affect the mark-to-space ratio of the periodically poled structures.

The –z faces of several z-cut lithium niobate samples were patterned with a mask, which had the gratings with identical periods of 6.5μm but with differing mark-to-space ratios namely 15:85, 20:80, 30:70, 40:60 and 50:50. The smaller number in each mark-to-space ratio (duty cycle) corresponds to the opening in the periodic gratings. As a positive photoresist was used to pattern the sample faces the smaller openings in the periodic gratings on the mask would then correspond to identical grating patterns in the photoresist (with smaller openings).

As the inverted domains formed below the exposed regions of the pattern in the resist extend laterally into the neighbouring non-inverted region during the over-poling process, smaller openings in the mask and hence the pattern defined in the resist could produce the desired effect. Conversely large openings would result in total merging of two oppositely spreading domain during the poling process and subsequently no remaining non-inverted surface regions.

The patterned samples were then over-poled with different empirical factors and briefly etched in HF acid to observe the periodically poled pattern formed on the –z faces. Several optical microscope images were taken of each of the poled sample and measurements were carried out to deduce the widths of the etched areas (the dark bands of one such image shown in figure 5.17) and the unetched areas (the bright bands in figure 5.16) on the –z face. The etched areas correspond to the non-inverted regions on the –z face whereas the unetched areas correspond to the domains inverted during the poling process. As the inverted domains are known to spread laterally the unetched regions / bright bands (corresponding to the inverted domain) are wider than the etched regions / dark bands (corresponding non-inverted regions). A schematic explaining the conducted trials is shown in figure 5.16.

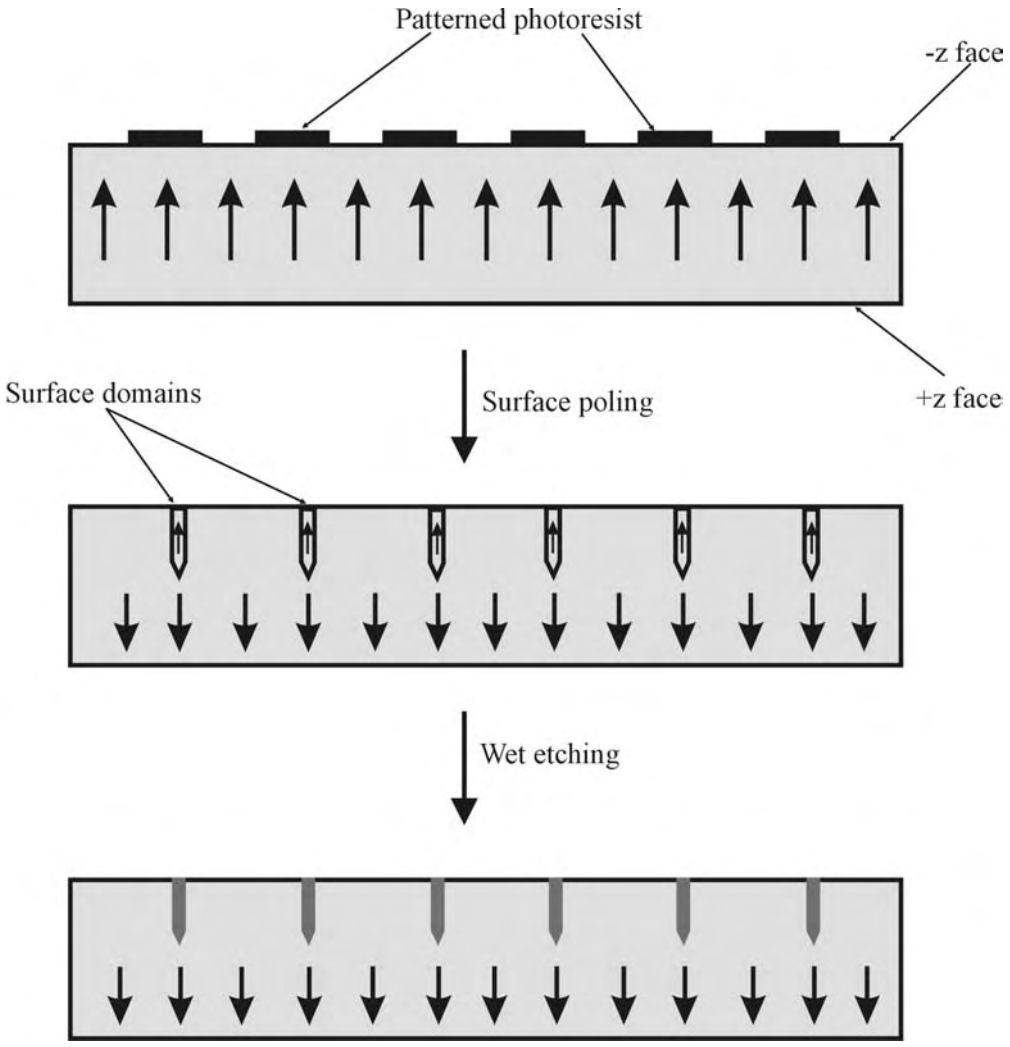

Figure 5.16 Schematic explaining the experiments carried out to study the effect of varying the mark-to-space ratio on the mask and the empirical factor on the periodically poled structure.

A plot of the variation of the ratio of the etched areas (non-inverted areas) / unetched areas (inverted areas) for different values of the empirical factor and different values of the mark-to-space ratio of the periodic pattern imposed on the photoresist is presented in figure 5.18.

The graph in figure 5.18 shows a variation in the ratio of the etched / unetched areas with the empirical factor for two different values of the mark-to-space ratios 20:80 and 25:75. Both the plots show a similar decreasing trend leading towards the ideal 50:50 mark-space ratio for an empirical factor value somewhere in the range of 5 and 6.

The conclusions drawn from this study will then be employed to fabricate actual waveguide structures in an attempt to produce short periodic structures with an ideal 50:50 mark-to-space ratio.

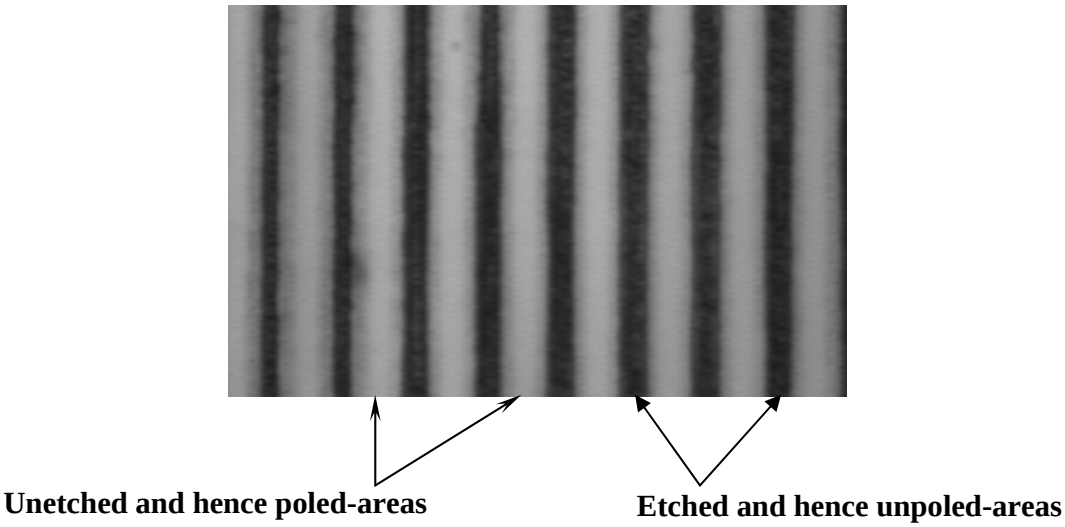

Figure 5.17 Optical microscope image, showing the etched and unetched regions of a briefly etched –z face of an over-poled sample

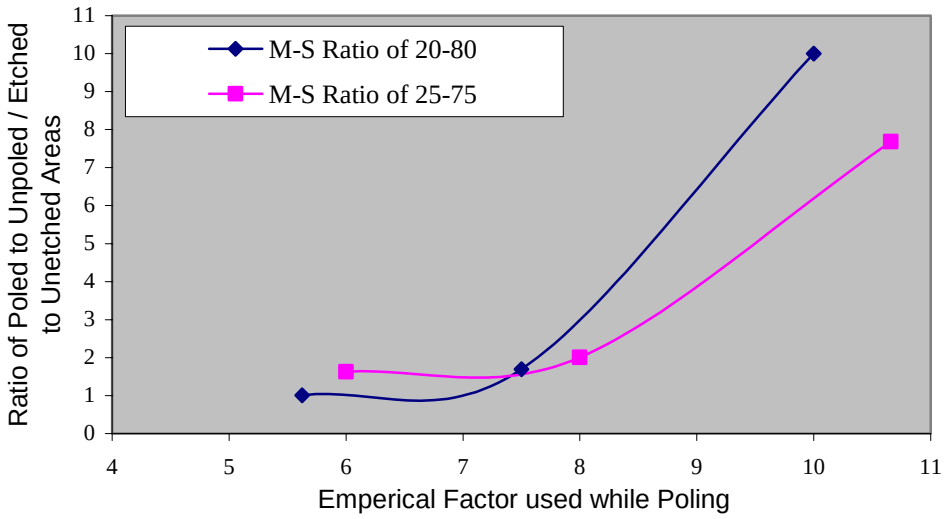

Figure 5.18 Graph showing the variation in the ratio of the etched / unetched regions on the – z faces with a variation in the empirical factor, for two different values of the mark-space ratios of the periodic pattern defined in the photoresist prior to poling.

5.7 Conclusions

A brief theoretical treatment of the concept of quasi-phase-matching for non-linear interactions using periodically domain-inverted structures in lithium niobate was presented. The technique of electric field induced periodic poling was briefly discussed and an innovative technique referred to as, 'surface periodic poling' of congruent lithium niobate crystal, based on the conventional electric-field poling, but involving an intentional over-poling step that inverts the entire crystal apart from the thin surface region below the patterned face, was proposed.

Experimental results achieved using this simple single-step technique to structure one and two-dimensional period structures in lithium niobate were shown. The surface poled structures showed good uniformity with depths extending to values of the order of few μm, thereby removing the high aspect ratio instability problems associated with the conventional bulk poling technique. The technique was implemented to achieve domains periodicities of ~1μm, and its applicability was further verified to pole first-order grating structures in predefined waveguide geometries for quasi-phase-matched waveguide interactions in lithium niobate, without any additional processing steps.

Quasi-phase-matched harmonic generation at the fundamental wavelength of 1.064 μm, by means of the first-order (G_{10}) reciprocal lattice vector, from a surface hexagonally poled planar annealed proton exchanged waveguide, with domain period of 6.7μm, was demonstrated. The initial quasi-phase-matching results from the two-dimensional hexagonal surface-poled waveguide structure shows the potential of this technique.

First-order quasi-phase matched blue light generation with reasonable efficiencies at 413.17nm, with domain periods of 2.47μm; from a surface poled Ti-indiffused channel waveguide was demonstrated.

The associated undesirable effect of lateral spreading of surface domains into the un-patterned area, leading to periodic structures with a non-ideal mark-to-space ratios and reduced non-linear interaction efficiencies was investigated. Attempts to optimise the surface-poling conditions for achieving periodic structures with ideal mark-to-space ratios of unity, were examined by varying the corresponding mark-to-space ratios on the mask used to pattern the periodic structure, and the empirical factor used for surface-poling. The initial parametric studies aimed at understanding the

mechanism showed conclusive trends for achieving periodic structures with an ideal mark-to-space ratio.

The suggested further work involves use of the acquired information for achieving surface poled first-order Ti-indiffused waveguide structures, with the ideal 50:50 mark-to-space ratio to demonstrate record non-linear interaction efficiencies.

5.8 References

Batchko R.G, Shur V.Y, Fejer M.M, Byer R.L, *Appl.Phys.Lett*, **75(12)**, 1673, 1999

Batchko R.G, Shur V.Y, Fejer M.M, Byer R.L, *Appl.Phys.Lett*, **75**, 143, 1999b

Berger V, *Phys.Rev.Lett*, **81(19)**, 4136, 1998

Bortz M.L, Fejer M.M, *Opt.Lett*, 23, 1844, 1991

Broderick N.G.R, Ross G.W, Offerhaus H.L, Richardson D.J, Hanna D.C, *Phys.Rev.Lett*, 84, 4345, 2000

Chanvillard L, Aschieri P, Baldi P, Ostrowsky D.B, Micheli M.D, Huang L, Bamford D.J, *Appl.Phys.Lett*, **76(9)**, 1089, 2000

Chowdhury A, Hagness S, McCaughan L, *Opt.Lett*, **25(11)**, 832, 2000

Chowdhury A, Staus C, Boland B, Kuech T, McCaughan L, *Opt.Lett*, **26(17)**, 1353, 2001

Fejer M.M, Magel G.A, Jundt D.H, Byer R.L, *IEEE, J. Quant. Electr*, **28**, 2631, 1992

Gunter P, *Nonlinear Optical Effects and Materials, Springer Series in Optical Science*, Volume **72**, 2000

He J, Tang S.H, Qin Y.Q, Dong P, Zhang H.Z, Kang C.H, Sun W.X, Shen Z.X, *J.Appl.Phys*, **93(12)**, 9943, 2003

Kintaka K, Fujimura M, Suhara T, Nishihara H, *Electron.Lett*, **32(24)**, 2237, 1996a

Kintaka K, Fujimura M, Suhara T, Nishihara H, *IEEE J. Lightwave Technol*, **14(3)**, 462, 1996b

Missey M.J, Russell S, Dominic V, Batchko R.G, Schepler K.L, *Opt.Express*, **6(10)**, 186, 2000

Myers L.E, Eckardt R.C, Fejer M.M, Byer R.L, Bosenberg W.R, Pierce J.W, *J.Opt.Soc.Am. B*, **12(11)**, 2102, 1995

Pruneri V, Webjorn J, Russell P.St.J, Barr J.R.M, Hanna D.C, *Opt.Commun*, **116(1-3)**, 159, 1995

Miller G.D, *Periodically poled Lithium Niobate: Modelling, fabrication and non-linear optical performance*, Stanford University PhD Dissertation, July 1998.

Saltiel S, Kivshar Y, *Opt.Lett*, **25(16)**, 1204, 2000

Schreiber G, Suche H, Lee YL, Grundkotter W, Quiring V, Ricken R, Sohler W, *Appl.Phys.B*, **73(5-6)**, 501, 2001

Shur V.Y, Rumyantsev E.L, Batchko R.G, Miller G.D, Fejer M.M, Byer R.L, *Ferroelectrics*, **221**, 157, 1999a

Shur V.Y, Rumyantsev E.L, Nikolaeva E.V, Shishkin E.I, Batchko R.G, Miller G.D, Fejer M.M, Byer R.L, *Ferroelectrics*, **236**, 126, 2000a

Shur V.Y, Rumyantsev E.L, Nikolaeva E.V, Shishkin E.I, Fursov D.V, Batchko R.G, Eyres L.A, Fejer M.M, Byer R.L, *Appl.Phys.Lett*, **76(2)**, 143, 2000b

Stegeman G.I, Seaton C.T, *J. Appl. Phys*, **58**, R57, 1985

Sterke M, Saltiel S, Kivshar Y, *Opt.Lett*, **26(8)**, 539, 2000

Sugita T, Mizuuchi K, Kitaoka Y, Yamamoto K, *Jpn.J.Appl.Phys.Part-1*, **40**, 1751, 2001

Taniuchi T, Yamamoto K, *Optoelectron. Devices Technol*, **2**, 53, 1987

Yamada M, Nada N, Saitoh M, Watanabe K, *Appl.Phys.Lett*, **62(5)**, 435, 1993

Yamada M, Saitoh M, *J.Appl.Phys*, **84(4)**, 2199, 1998

Yariv A, *IEEE J. Quantum Electron*, **9**, 919, 1973

Chapter 6

Domain Engineering and MEMS/MOEMS application

6.1 Introduction and chapter layout

This chapter begins by introducing the idea of MEMS and MOEMS, acronyms for microelectromechanical systems and micro-opto-electromechanical systems. It then continues with an explanation of the fabrication details of microstructured free-standing structures such as cantilevers in lithium niobate, with an end application in a micro-optoelectromechanical system. The final section of the chapter then explains some basic mathematical treatment to deduce the frequency of vibration of the fabricated micro-cantilevers in lithium niobate.

This field of MEMS/MOEMS is an interdisciplinary field that incorporates the areas of integrated circuit fabrication technology, mechanical and materials science and also engineering of microscopic mechanics to create micro-systems and devices that can improve the performance of systems in for example the optical communications field. MEMS is generally used to refer to the electronic and mechanical aspects of a micro-system, but it can also include magnetic, thermal, fluidic and electromagnetic mechanisms within the broad overall principle of operation. By extension, optical MEMS (MOEMS) refers to systems which couple optics with electronics or mechanics for producing moving structures and systems on the micron scale. With the aid of technology developed within the manufacture of electronic integrated circuits such as bulk micromachining, surface micromachining, LIGA and microstereolithography the promising field of MEMS/MOEMS and smart systems has made great advances, generating considerable enthusiasm in chemical, mechanical, electrical engineering, medical, materials science and food science communities.

This field of MEMS was originally conceived by the Richard Feymann in 1959, via his now famous remark, “There’s plenty of room at the bottom’’. He predicted the fact that there was a vast virtually boundless field of system miniaturisation. His assumption was based on the fact that as none of the laws of physics posed any intrinsic limitations to miniaturisation, it was only our ability to make physically small things, which imposed any constraints.

Most of the present day MEMS devices are based on well advanced and established silicon technologies, due to the inherently low cost and extensive range of fabrication processes found within the modern semiconductor foundries. A range of micron sized functional structures such as gears, springs, suspensions, pumps, orifices, grooves, diaphragms and cantilever beams have been realised using single crystal silicon combined with structural polysilicon and sacrificial silicon dioxide overlayers, processed using the range of well-established techniques. Cantilever (micro-cantilever) beams are one of the mostly widely sculpted microstructures that has allowed the fabrication of a range of micro-systems, and due to its ease of implementation as both a switch and a resonator it remains one of the basic MEMS building blocks (Petersen'79). In addition to their use in imaging (Walter'91, Lee'00, Eckert'00, Akamino'96, Heisig'00, Sasaki'00) and nanolithography (Snow'94, Minne'95, Majumdar'92), cantilevers have also attracted great attention as sensors (Chen'95, Manalis'97, Lutwyche'95) and actuators (Zhang'99, Quandt'95, Pelrine'98, Lee'99, Kulevitch'96). Systems using single cantilevers have been employed as sensors to measure quantities that are beyond the limits of equivalent classical techniques, and applications as diverse as measurement of phase transition (Berger'96), remote infrared detection (Wachter'96), vapour detection (Thundat'95), surface-stress detection, modulation of light/liquid (Motamedi'97, Kock'97 and IC-testing (Qi'00), have been successfully demonstrated.

Several actuation mechanisms including piezoelectric, thermomechanical, electrostrictive, and magnetostrictive effects have been employed for micromechanical systems, however electrostatic actuation because of its ease of implementation continues to remain a firm favourite for silicon based MEMS. The electrostatic actuation mechanism, though simple, suffers from the inherent limitation of the $1/r^2$ dependence between force and distance, r, contained within Coulomb's law. Catastrophic damage to the cantilever either due to inelastic bending or extension or actual physical contact (stiction) between the cantilever and the substrate leading to permanent adhesion, can occur as the Coulomb force scales quadratically with a decrease in distance. The converse piezoelectric effect, however, for which an applied electric field produces a resultant strain, is an intrinsically linear effect, with the produced tensile or shear strains produced depending on the product of the corresponding piezoelectric tensor coefficient and component of the applied electric field. The apparent advantages of this actuation mechanism prompted the

investigation described in this chapter of the utility of fabricating micro-cantilevers in single crystal lithium niobate, which has an inherent piezoelectric property. The available piezoelectric coefficients of lithium niobate although are not as large however as those for other materials such as lead zirconate titanate (PZT), for example. There are several reasons however for our wanting to use single crystal lithium niobate for construction of micro-cantilevers. The precise values of the piezoelectric tensor coefficients for ceramic or polycrystalline PZT are known to depend on the thin film deposition methods used, and as an example the estimated d_{31} coefficient (Lee'99) of sol-gel derived PZT (Lee'96) is only 60% of the value reported for bulk PZT. For reproducibility of device performances the small but accurately known values of the piezoelectric coefficients of single crystal lithium niobate thus offer a distinct advantage over ceramic and polycrystalline PZT films. Additionally the hysteresis effects associated with the latter are absent in their single crystal counterparts, and should be avoided if possible in practical device construction.

6.2 Fabrication Technique

The route employed to achieve the aim has the following steps: multiple solvent cleaning, photolithography, poling, polishing, etching, electrode deposition and finally actuation of the structured cantilever. The separate stages of the fabrication procedure employed are shown in the schematic or flow diagram, in figures 6.1 and 6.2.

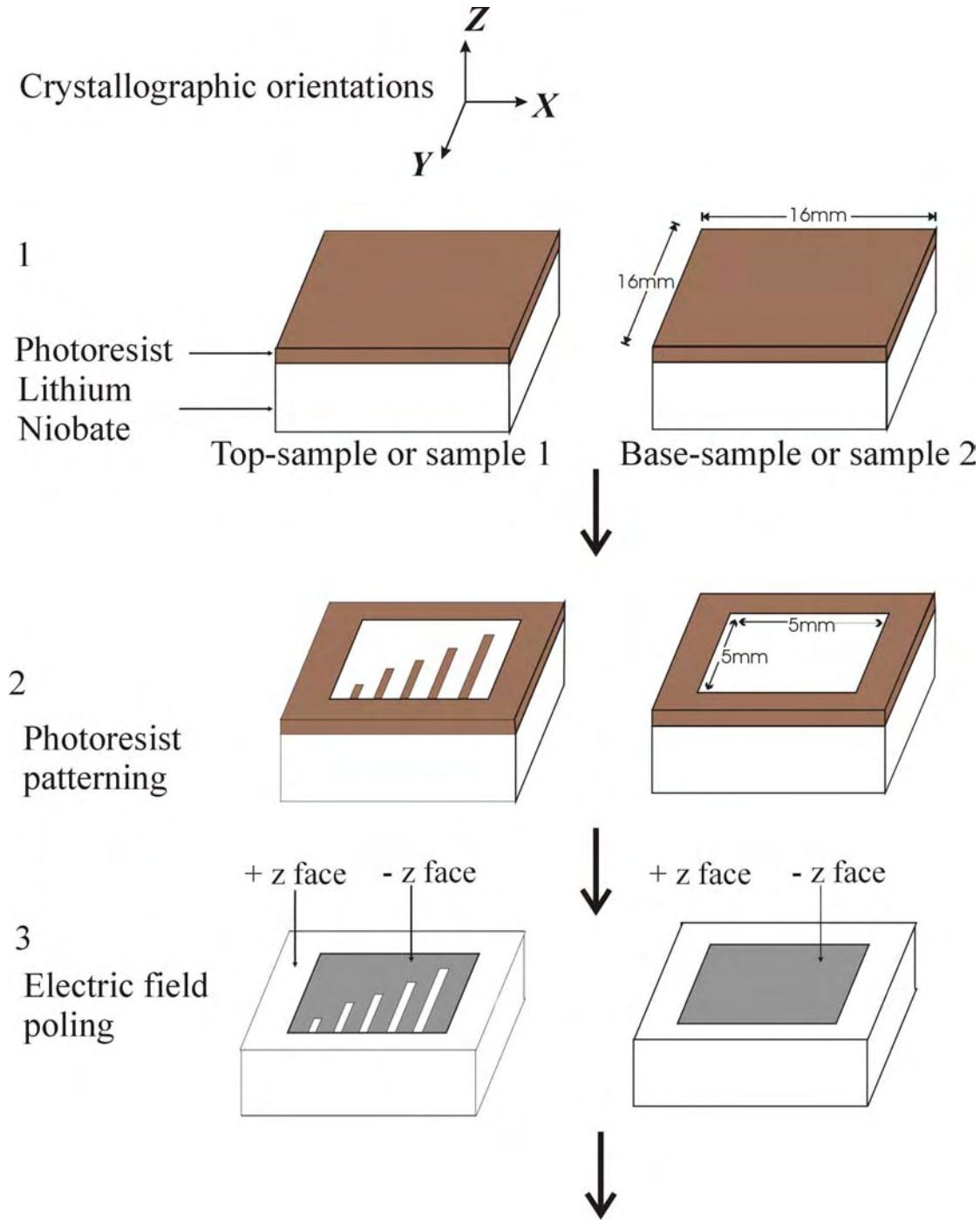

Figure 6.1 Schematic 1, showing the different steps involved in the fabrication of free-standing micro-cantilevers in single-crystal lithium niobate.

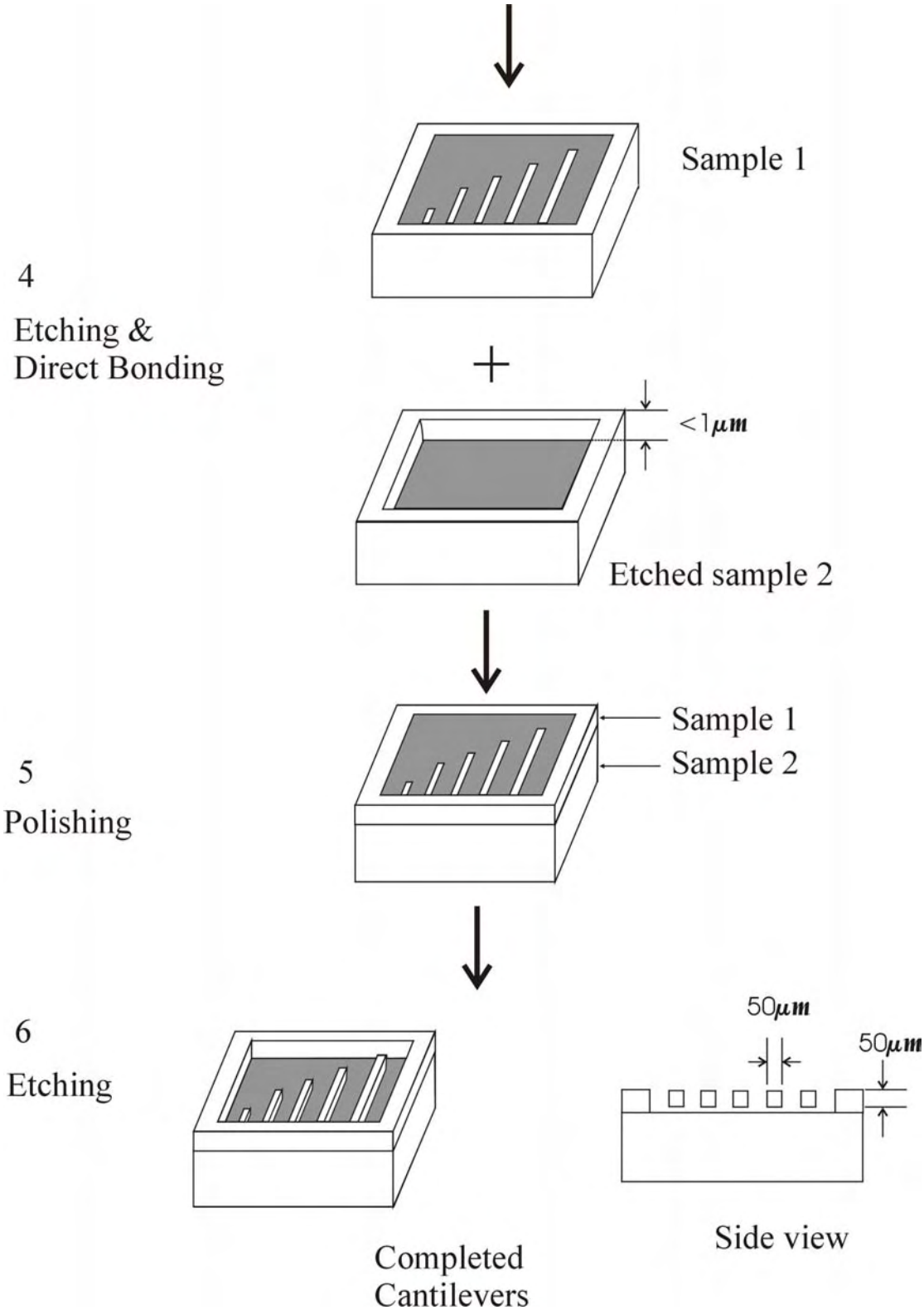

Figure 6.2 Schematic 2, showing the different steps involved in the fabrication of free-standing micro-cantilevers in single-crystal lithium niobate

Before each fabrication step is explained at length, the specifics of the lithium niobate samples used have been detailed in the following section.

6.2.1 Materials

The lithium niobate samples used were purchased from Crystal Technology, USA / Yamaju Ceramics, Japan, and were optically polished, z-cut single crystal wafers having a diameter of 76.2 mm and a thickness of 500 or 300 μm. These wafers were then diced in-house into squares of 16 mm x 16mm or other dimensions as required.

6.2.2 Step one: Multiple Solvent Cleaning

All the samples were subjected to a sequential multiple-solvent cleaning process, in an ultrasonic agitator bath at a constant temperature of 50°C. This successive solvent treatment was employed to remove organic and inorganic contaminants from the surface of the samples and also for simultaneous removal of the solvents used in the previous step.

All the temperature-controlled steps had to be taken as lithium niobate is pyroelectric in nature and so a sudden change in temperature could induce unintentional flipping of ferroelectric domains in small regions of the single crystal samples. These small regions with reversed domains, referred to as poling dots, could pose problems to the transmission of light through the samples.

6.2.3 Step Two: Photolithography

The –z faces of the dried and clean samples were then spin coated with a uniform layer of a positive photoresist layer with a thickness of ~1.1μm. The samples were then patterned using pre-designed chrome on silica mask and a Karl Suss MA4 mask aligner, which imprinted the pre-designed pattern on the photoresist on exposure to the UV light and subsequent treatment with a developer. Since the photoresist used was a positive one, areas on the photoresist, which were exposed by the UV light through the designed mask were polymerised and so could be then dissolved off by the developer.

The samples patterned had two different designs on them, one each for the top and base samples, which eventually were to be directly bonded at a later stage.

Mask details:

The mask used was designed using the Sigraph-Optik software, developed by Siemens, and was fabricated by the Microelectronics department of the University.

The layout of the mask with the desired set of cantilever patterns is shown in figure 6.3.

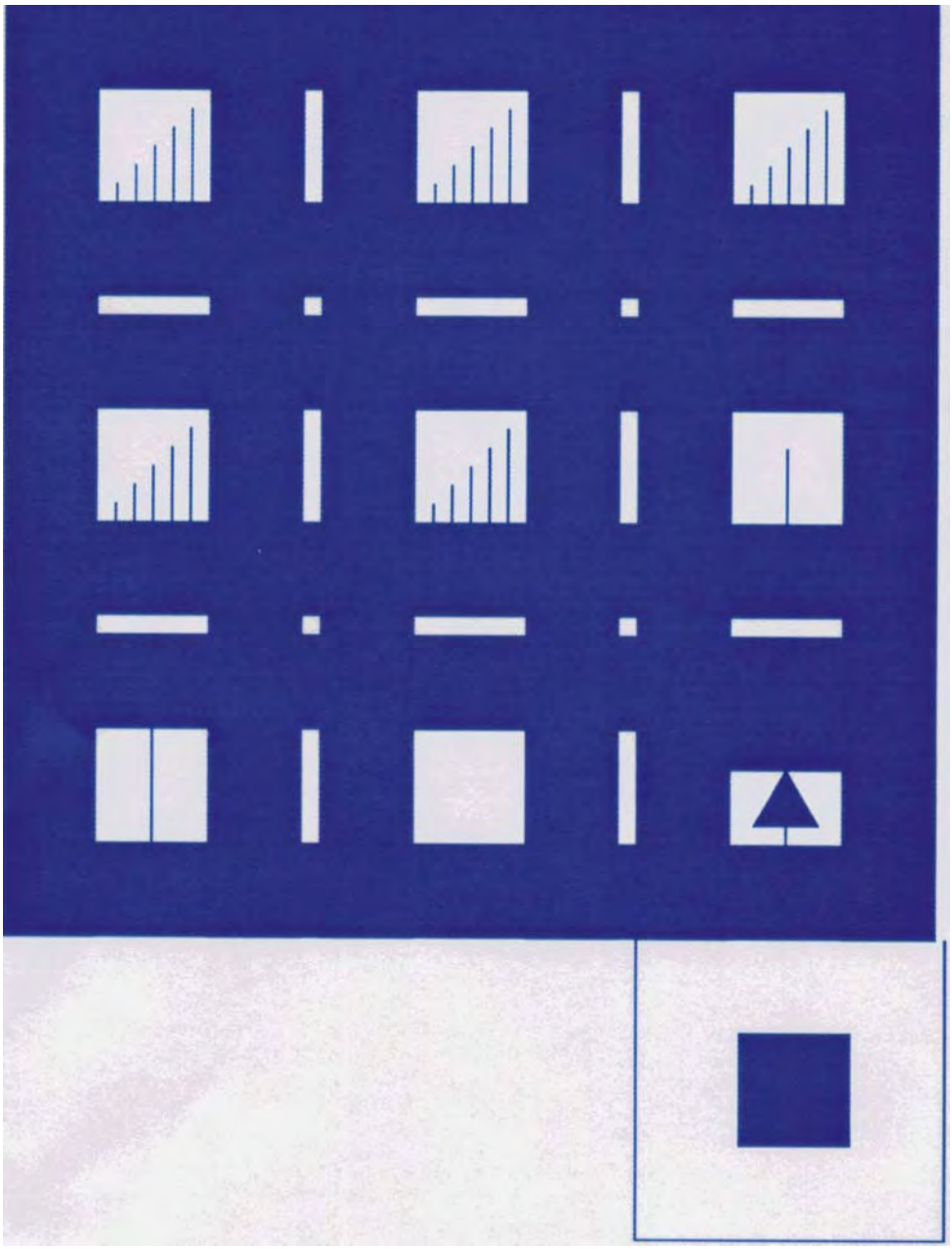

Figure 6.3 Layout of the employed mask, showing five different cantilever patterns, each having five finger-like structures with varying lengths. Each pattern in turn has structures of the same length but differing widths.

Initial efforts and experience to go through these steps led to a rethink and re-design of a new mask, which had patterns of chromed cantilevers having lengths of 1-5 mm

and widths of 10-50 μm with a large chrome deposited frame of 5mm around each of them. This was required for eliminating alignment errors of roughly half a mm or less encountered when direct bonding the top and base samples.

The new mask also had a pattern for the base sample too, one which simply had an un-chromed square of 6mm x 6mm with a chromed frame of 5mm around it. The blue areas within the mask shown in figure 6.3 are the chromed areas whereas the white areas are the (un-chromed and hence) transparent areas. Also each pattern on the mask was deliberately kept to a square of size 16mm x 16mm so as to eliminate any alignment errors as discussed earlier.

The new mask was also designed to have a pattern with two cantilevers facing each other, with their free ends separated by a distance of three μm. The aim was to structure these oppositely faced cantilevers, fabricate waveguides (by the direct single step UV-writing technique) (Mailis'03) on them and actuate them via the piezoelectric effect, eventually realising a switch. The mask also has a pattern for an accelerometer, which also is one of the devices we intend to realize in the future.

6.2.4 Step Three: Poling

Domain inversion in the selectively patterned areas of the top and bottom samples, having the cantilever features and a central square opening respectively was achieved using the conventional e-field poling technique.

The edges of the samples to be poled were taped off using insulating tape, leaving a border of ~5mm around the features to be inverted to prevent surface breakdown on application of high electric fields desired for poling.

6.2.5 Step Four: Direct Bonding

The technique of bonding as its name suggests works without the aid of any glue or fixant material, and has been widely used in the fabrication of Si on insulator structures and also p-n junctions (Mitane'92, Grey'97, Ljungberg'93, Himi'94, and Tong'94). In this process the two materials are usually bonded at a high temperature, which increases the atomic diffusion at the boundary. A residual thermal strain is introduced on cooling if the temperature coefficient of expansion of the two bonded materials differs and can result in fracture at the interface. Bonding characteristics

such as mechanical strength, toughness, ductility and electrical conductivity depend on the boundary structure.

It is a known fact that when two macroscopic bodies are brought close to each other, at distances less than a few hundred nanometres a collective Van der Waals force results in an attraction between them. If the surfaces of the two macroscopic bodies are absolutely flat and clean such that they can approach each other to within a few nanometres then this leads to an interfacial bonding between them. This process is however a complex one. Over and above the Van de Waals force of attraction (Haisma'94), which is one of the contributors to the bonding phenomenon, other forces like the attraction between static electrical charges on the two surfaces as well as an interaction between adsorbed layers on the two surfaces also contribute to the bonding.

Stringent requirements are therefore desired to effect this ambient bonding. The complementarity of the curvatures of the two surfaces has to be of a very high degree with shape deviations of less than fifty nanometres to be precise. The mechanical states of the surfaces have to be good too i.e. a high surface finish and no subsurface damages are required. Direct bonding being an ambient technique the surfaces have to be chemically clean and also chemically activated for bonding. The strength of the bond formed increases over a period of time, and the process is irreversible if the bonded interface is annealed for some hours at higher temperatures.

The first step of the process was the cleaning of the faces to be bonded using the previously described technique of multiple solvent cleaning, followed by a treatment in a mixture of H_2O_2+NH_4OH+H_2O, in the ratio of 1:1:6, to render hydrophilic the surfaces to be bonded. This was followed by a thorough rinse in deionised water for a few minutes. The samples were then blown dry and the faces to be bonded were brought into contact. Slight finger pressure was applied to them for removal of air trapped in between the faces thereby bonding them. The samples were then heat treated at 120°C for fifteen to twenty minutes to induce the pyroelectric effect (Missey'98). This effect in turn would bring the two faces even closer as a result of the electrostatic forces of attraction between the static charges induced on the two surfaces, eventually helping the formation of hydrogen bonds (Spierings'95). This is confirmed by the disappearance of most of the interference fringes previously visible at the interface. The samples were then annealed at a temperature of 320°C for six

hours for maximum bond strength, which would then allow further machining. The samples were left for a few days before the final annealing step.

Initial bonding experiments were conducted to bond the negative face of the cantilevers to the negative face of the square pattern in the base sample, banking on the fact that a negative face would not bond as effectively to another negative face and so would eventually carve out a cavity under the cantilever when the sample was etched. Figure 6.4 shows a schematic of the two faces that were bonded. The areas shaded dark are the negative z faces whereas the lighter areas are the positive z faces of the two samples.

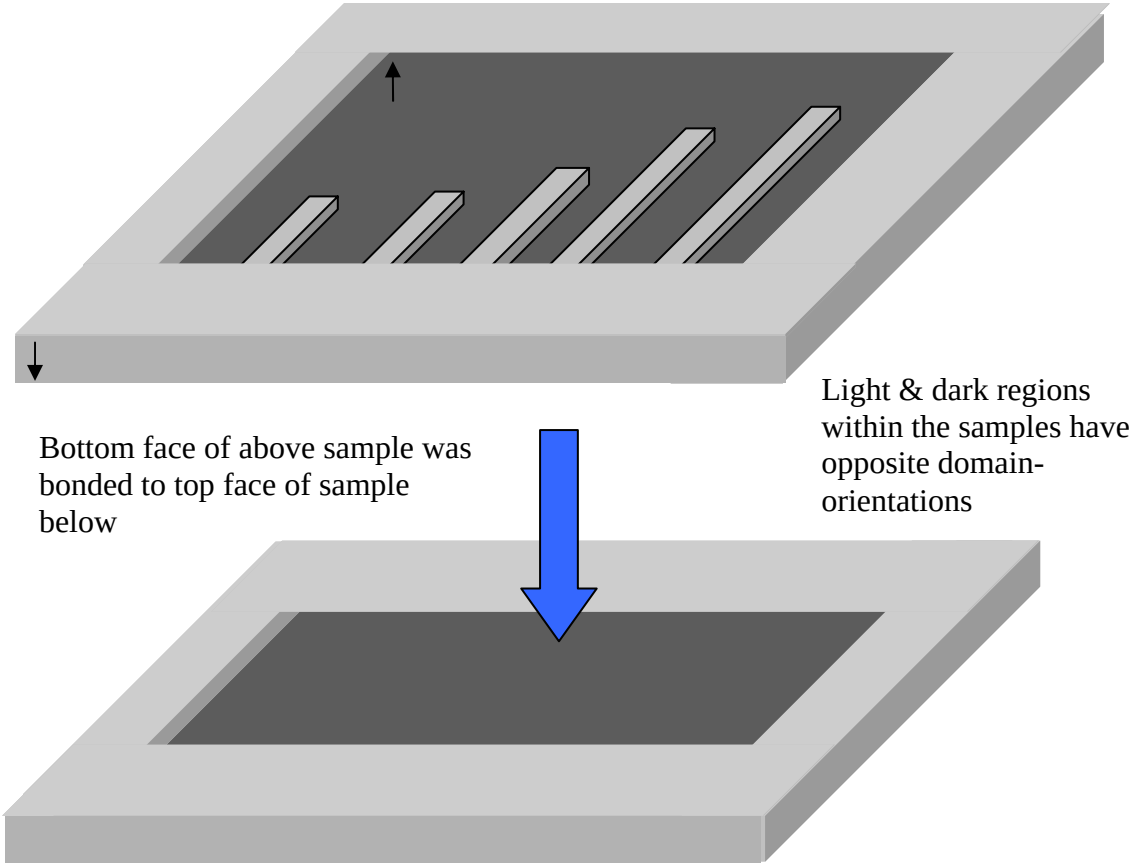

Figure 6.4 Schematic showing the faces of the two samples that were to be bonded.

However the bonding of the similar faces was as good as that of dissimilar faces, which meant that the micro-structured cantilevers couldn't be freed from the base samples. Figure 6.5 shows one of the cantilevers, which remained stuck to the base sample. A part of this cantilever however was not well bonded and so was free from the substrate effectively forming a bridge structure.

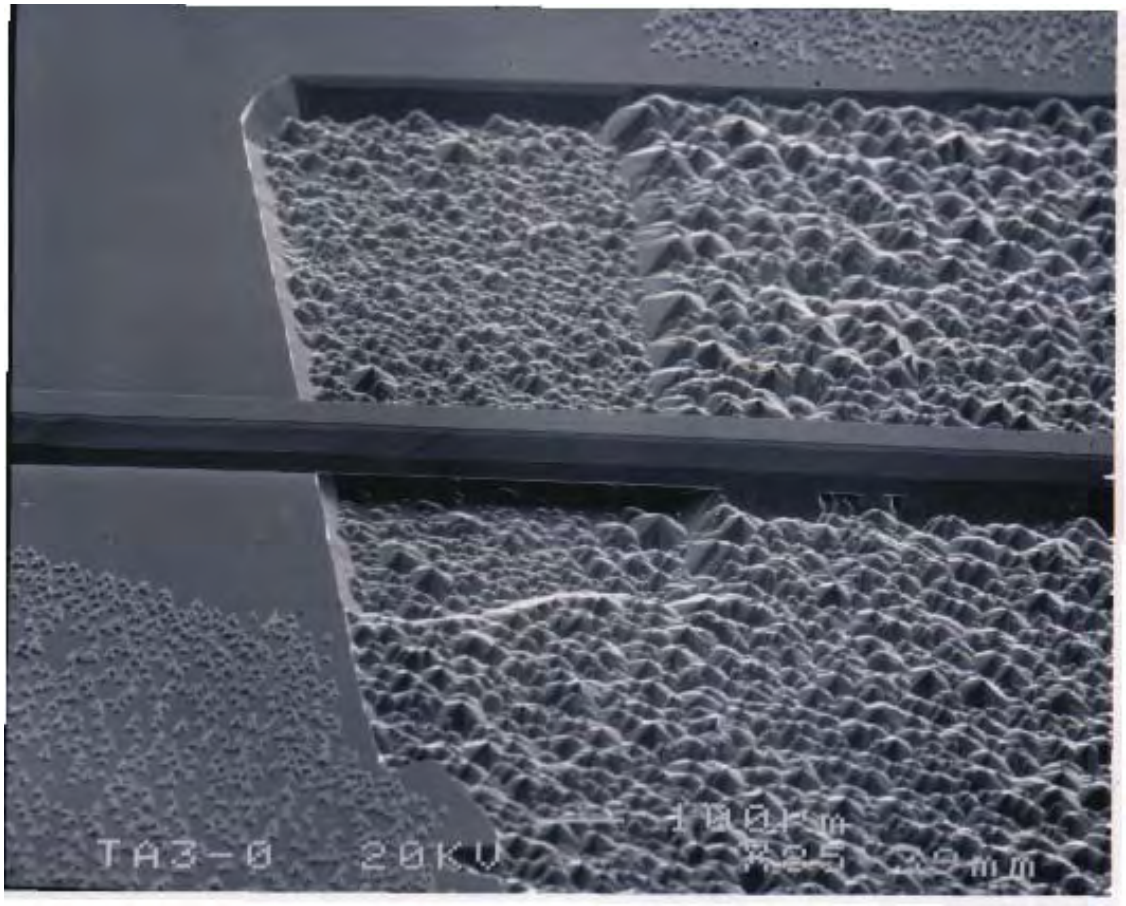

Figure 6.5 SEM image showing a cantilever partly freed (etched out from beneath), and partly perfectly bonded (not released by the etching step) to the base sample.

The fabrication route hence had to be re-thought, and it was decided to etch the base sample with a mixture of $HF+HNO_3$ to carve out a cavity in the base sample, before bonding it to the sample with the cantilever feature. The idea was that the pit, of order of a few hundred nanometres in depth, etched out in the base sample would serve as a deterrent during the bonding process between the bottom of the cantilevers and the base sample. This modified bonding approach proved entirely suitable for fabrication of the free cantilevers. The schematic shown by the figures 6.1 and 6.2 is of this improvised fabrication process.

In order to bypass this relatively difficult procedure of direct bonding, which cannot be successfully implemented regularly, many different adhesives were initially tried instead to glue the faces together. Some of the adhesives used were two compound epoxy based ones like Araldite rapid, Araldite heavy duty, RS Quickset and cynoacrylate based ones such as Loctite super glue and Perma bond.

Glued samples were immersed in the mixture of the etchants, $HF+HNO_3$, for over a period of two days, to see if they were affected by the etchants. It was vital to confirm

whether the adhesives would survive the etchant for over the required long time periods. All the adhesives tried failed to survive immersion in the HF/HNO_3 etchant mixture, which attacks the adhesive along the edges of the samples and subsequently seeps its way through between the samples further reacting with the adhesive in-between leading to separation of the glued samples. Another two-epoxy-based adhesive with a high chemical inertness namely EP21AR manufactured by Master Bond, USA, was also tried out to overcome the problem. Samples were also glued together with a 100μm borosilicate glass cover slip between them. The aim behind this was to effectively etch out the glass cover-slip form beneath the cantilevers and the cantilevers itself during the etching stage. A UV cured adhesive and black wax were also tried to glue the samples together. All these samples namely those glued together with EP21AR, UV cured adhesive and black wax were polished down to the desired thickness and then etched as above. All of these adhesives survived the polishing stage but were unable to hold the samples together during the final etching stage. The UV cured adhesive was tried, as it can be spin coated on the faces, which were to be bonded, allowing the formation of a uniformly thin layer of the adhesive on the faces of the samples. This was thought to be an ideal choice, as the thinner the adhesive layer in between the bonded samples, the lesser the chances the etchant would have to seep in between the samples leading to their separation.

As HNO_3 was itself thought to affect the adhesives, a rerun of the etching procedure, but this time with just hydrofluoric acid was also conducted.

Samples bonded with black wax, UV cured adhesive and EP21AR were immersed in hydrofluoric acid for over a period of two days to see the effect. However these tests were also unsuccessful.

6.2.6 Step Five: Polishing

A standard lapping and polishing technique was used to effectively reduce the bonded sample to the desired thickness. An autocollimator was used to mount the samples on the specially designed ceramic lapping mount to ensure that the face to be lapped was absolutely parallel to the lapping plate It is vital to keep track of the exact amount of the material that had been lapped off the sample face, as knowledge of the right thickness of the polished samples was essential, it being the guiding parameter for the next step of wet-etching. Samples were first lapped off using a 9μm Al_2O_3 slurry

down to the desired thickness, followed by a lapping off, using the 3μm Al_2O_3 slurry again to the required thickness. (It is essential to at least lap off 27μm using the 3μm grit as the 9μm particles can produce scratches which are three times their size). This is then followed by the final polishing step on a polyurethane polishing pad, using Syton, a colloidal solution of 0.125μm silica. This essentially removes the scratches left behind as a result of the lapping step with the 3μm grit, (which can leave scratches as deep as 9μm on the face of the sample. So as in the previous case it becomes essential to at least polish the face of the sample by an amount of 9μm to achieve the desired optical finish). This was confirmed by viewing the polished face under a microscope. The samples were lapped and polished down to a final thickness of 50μm.

6.2.7 Step Six: Etching

The directly bonded samples were then etched in a mixture of (48%) HF and (78%) HNO_3 in the ratio of 1:2, at a temperature of 60 ^{0}C for the required time, to etch out the cantilevers. Figure 6.6a and 6.6b show optical microscope images of an etched out cantilever, where in the microscope has been focussed on the top-face of the cantilever and the etched floor respectively. The fact that the etched floor can be viewed through the cantilever proves the good optical quality of the cantilever shown in figure 6.6b.

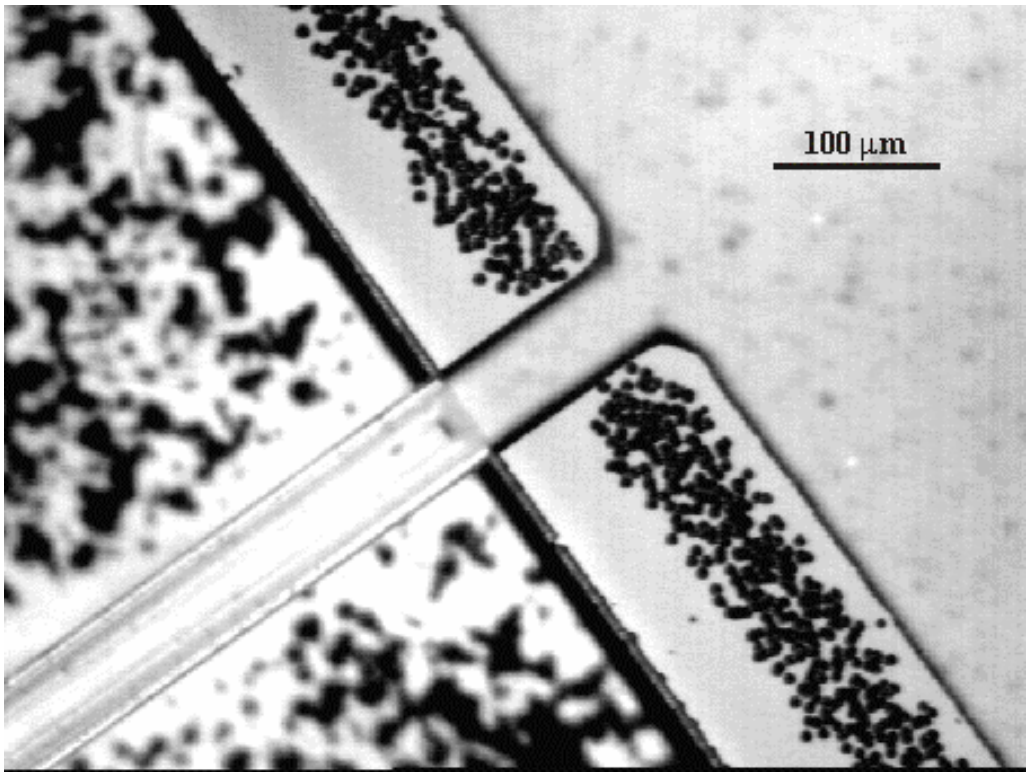

Figure 6.6a Optical microscope image of an etched cantilever, with the microscope focussed on the top face of the cantilever

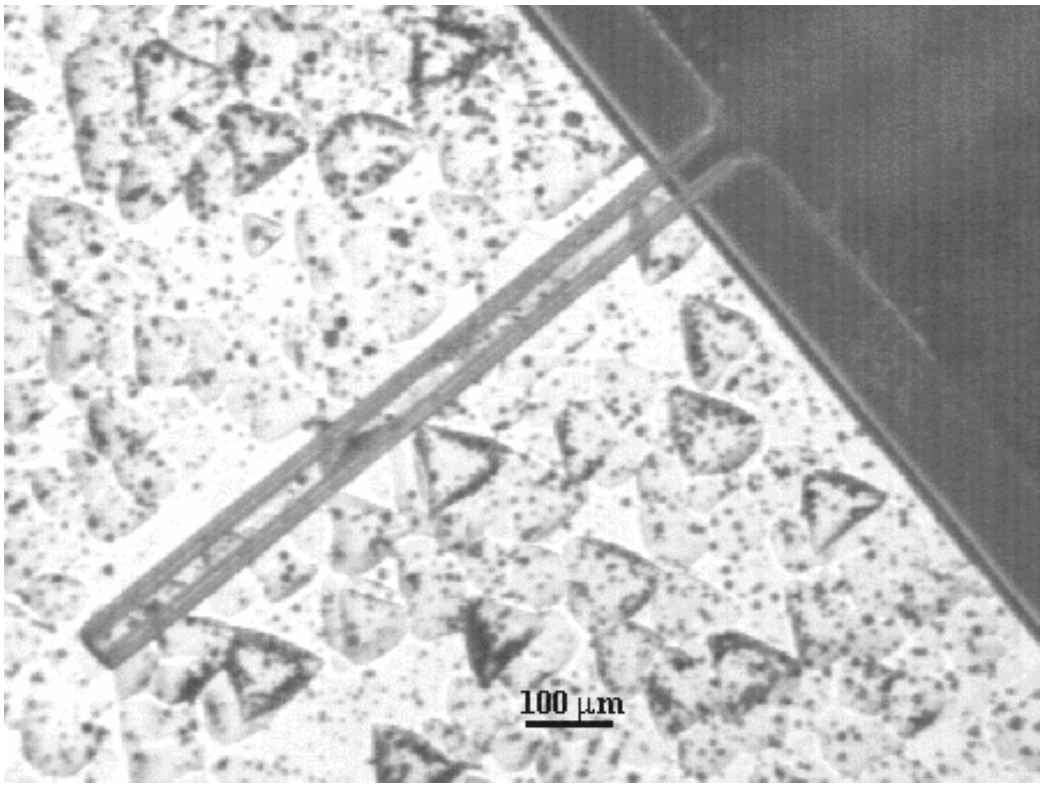

Figure 6.6b Optical microscope image of an etched cantilever with the microscope focussed on the etched floor below.

6.2.8 Step Seven: Electrode Deposition

This final step of the fabrication process was to define electrodes on the fabricated micro-structures, and was accomplished by use of a focussed ion beam system (FIB). FIB systems are used in the semiconductor industry for the repair of integrated circuits and photomasks, for failure analysis and for process control (Melngailis'87, Young'93 and Prewett'93). FIB milling has also been used for precise modifications at the micrometer and sub-micrometer scale. The ability to selectively remove and deposit material without the need of a patterned mask has been successfully exploited for applications in microelectronics (Melngailis'87, Young'93a and Prewett'93). When used as a milling tool, the milling rate of the FIB, can be altered by variation of the beam current. The milling rate can also be enhanced in a reactive-gas-environment (Young'93b). A stream of a reactive gas supplied by an injection needle close to the milled region can increase the milling rate as the gas forms a volatile product with the target material. Iodine gas is known to double the etch rate whereas XeF_2 is known to increase the etch rate a hundred times. However in some cases addition of a gas is used to deposit metals or insulators. For example, decomposition of an organo-metallic gas of platinum by an ion beam, leads to a deposition of the metal layer. The main use of FIB is in the physical sputtering of materials by ion impact, but it also serves as a scanning ion microscope, using the generated secondary electrons or ions for imaging.

The electrode fabrication on the lithium niobate micro-structures, using the Focussed Ion Beam deposition technique was done by a company in Bristol. A few lines of the order of a fraction of micron in width, deposited by this source are shown in figure 6.7.

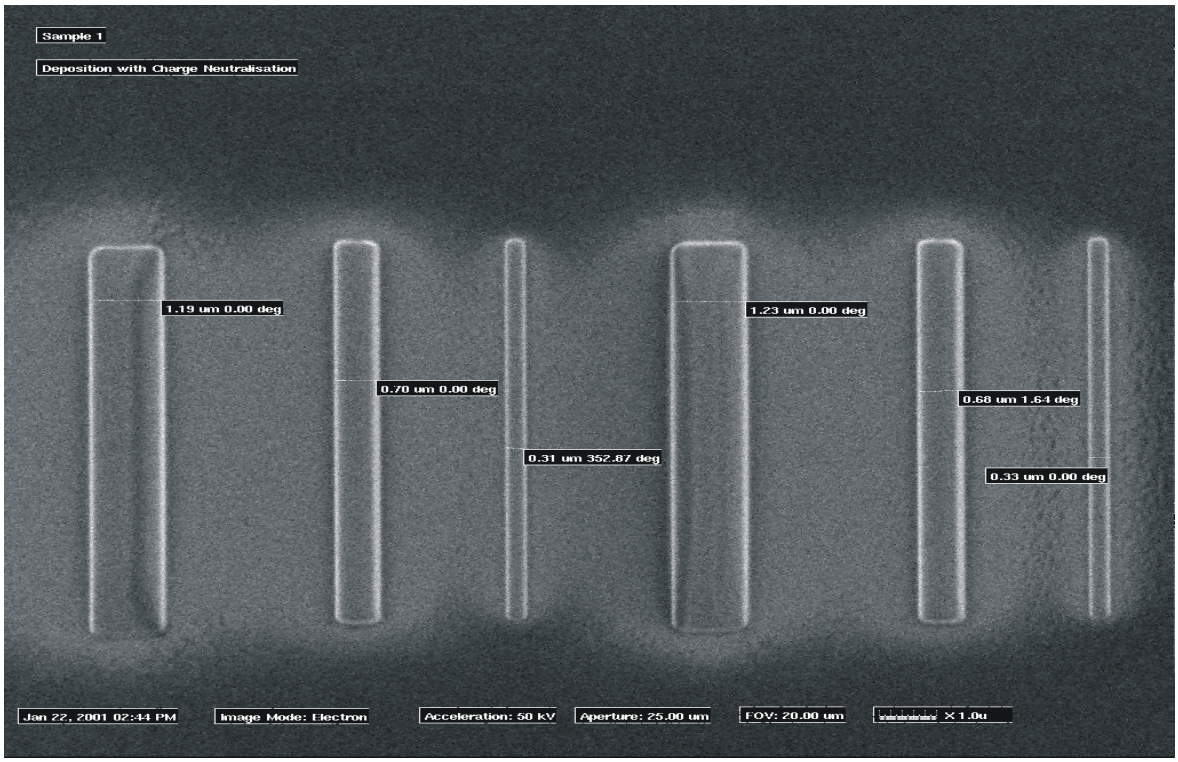

Figure 6.7 FIB micrograph showing several tungsten-metal lines of varying widths deposited during a test-run

As the deposition using an FIB can be over edges too, the electrodes deposited over the edges could then be connected to connecting pads for external electrical contact. This advantageous aspect was the reason behind the use of the FIB system by us. The picture of some of the tungsten deposition done by the same company over an etched edge is as shown in the figure 6.8.

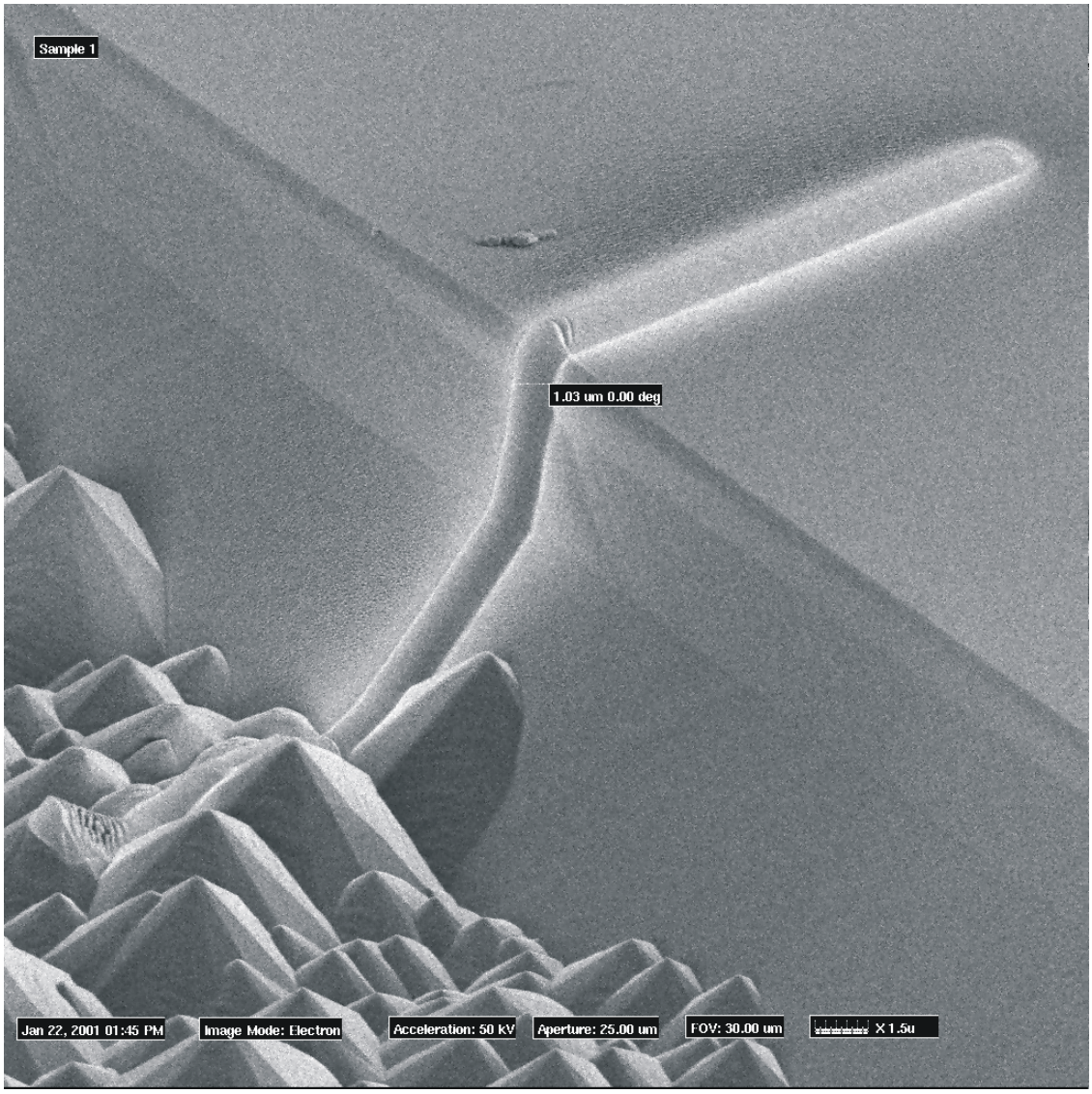

Figure 6.8 FIB micrograph showing a test-deposition of tungsten metal-track along an edge in an etched lithium niobate sample.

As lithium niobate is an insulator, the build up of charge on the surface on which the deposition was done has to be neutralised. This was achieved by the simultaneous use of a beam of electrons from an electron-flood-gun, which compensated the charge.
Electrode deposition was required along the length of the cantilever beams i.e. along the y-axis of the crystal, such that the deposited electrode covered exactly half the width of the cantilever. Figure 6.9 depicts the actual shape of the electrode to be deposited. An electric field applied along the x-axis, would then produce a strain through the converse piezoelectric effect, in that region, leading to a compression or

extension of the electroded top portion of the cantilever, depending on the direction of the applied field. This effect of extension or contraction would produce a bending moment as in a bimorph structure, and result in a deflection of the cantilever in the *z* direction.

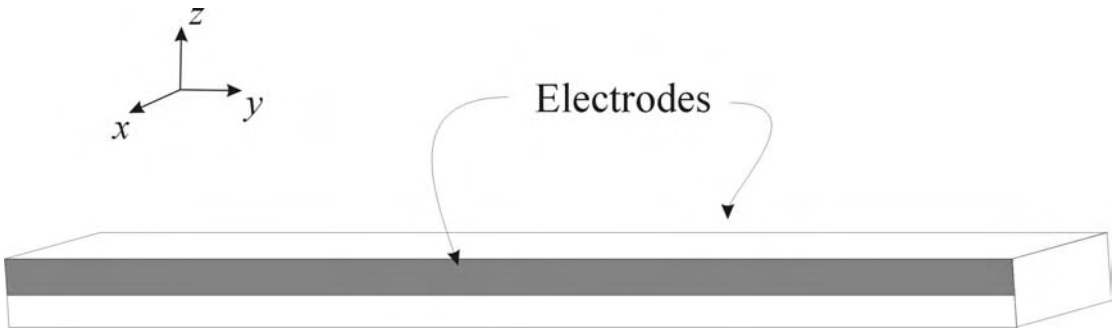

Figure 6.9 Schematic explaining the areas on the structured cantilever where the metal-electrodes were to be deposited.

A scanning ion micrograph of a free cantilever fabricated by the described route is shown in figure 6.10.

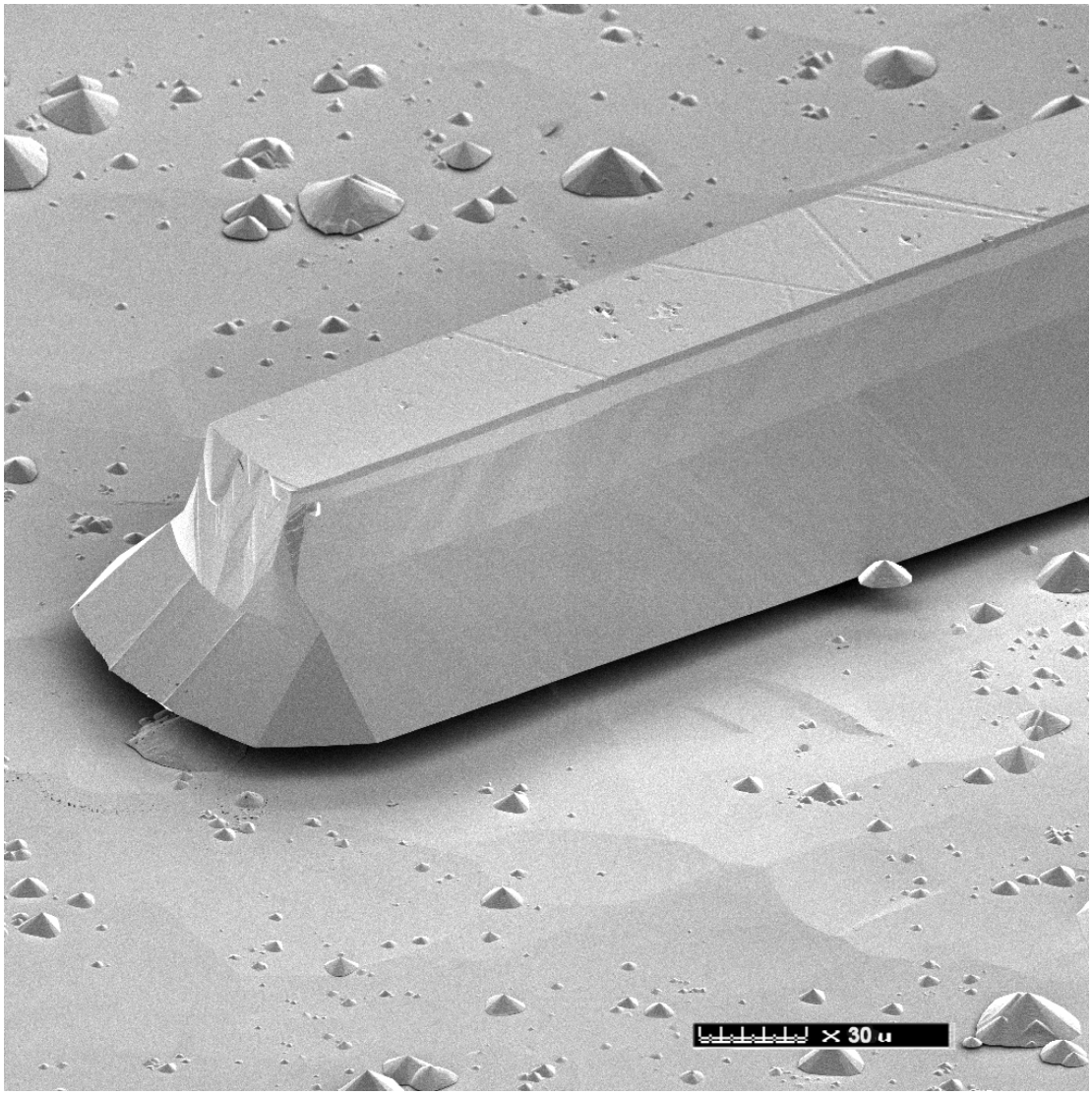

Figure 6.10 Scanning ion micrograph of a free-standing micro-cantilever sculpted in single crystal lithium niobate, by the described novel fabrication route**.**

The scanning ion micrograph showing electrodes formed by depositing tungsten along the top of the two side-faces of the fabricated cantilever is as shown in figure 6.11. Figure 6.12 is the scanning ion micrograph showing the same electrodes extended over on to the adjacent face for further contact with a contact pad.

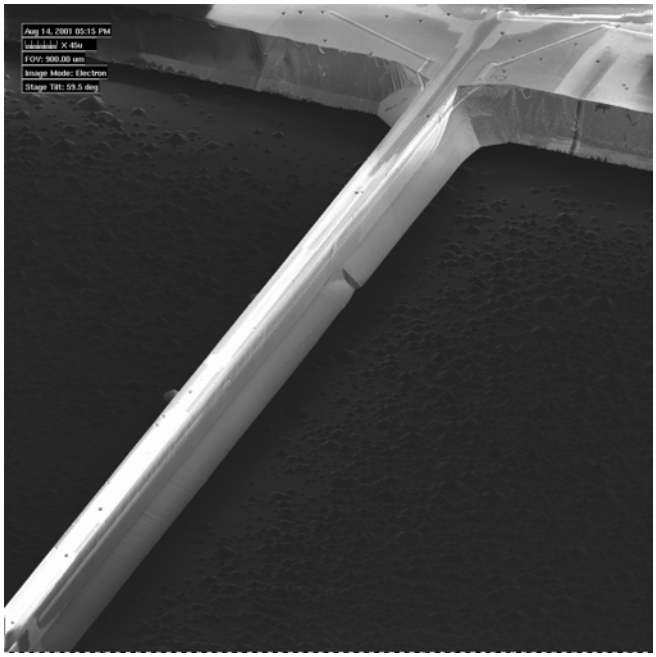

Figure 6.11 SEM image of a micro-cantilever with metal electrodes deposited on either side along the top half of the structure.

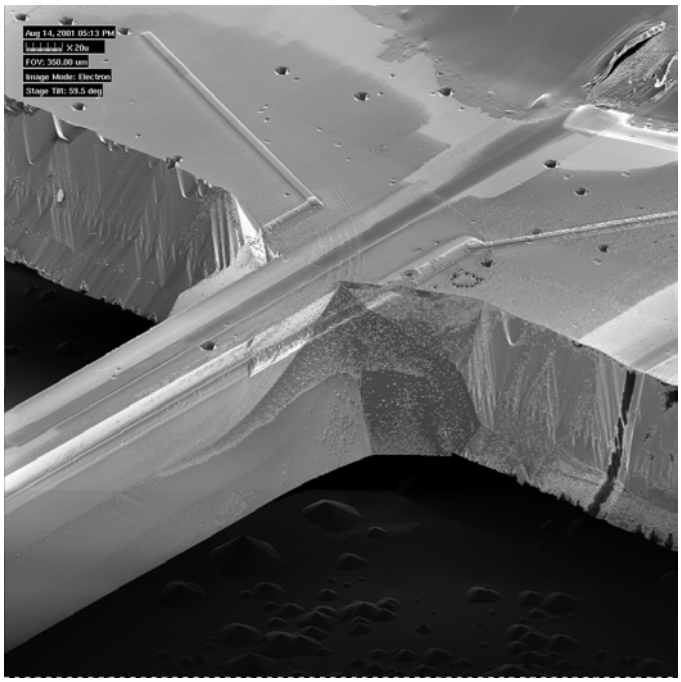

Figure 6.12 SEM image showing a micro-cantilever with tungsten electrodes deposited on either side, along the top half of the structure, further extended over the top face for contacts with deposited metal pads.

The unavoidable splash of tungsten metal into adjacent areas, during deposition of the two strip-electrodes along the top half of the cantilever structures, resulted in the undesired electrical contact between the deposited electrodes. This problem was circumvented by subsequent deposition of the metal electrodes along the bottom half of the cantilevers as shown in figure 6.13.

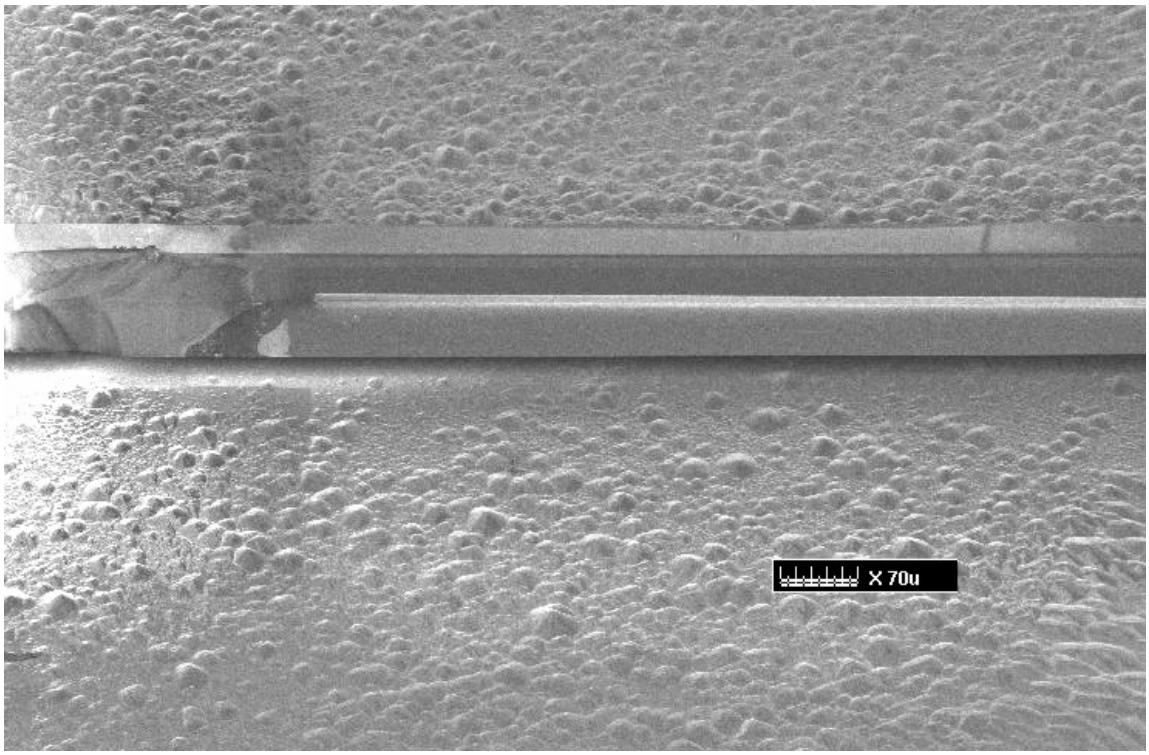

Figure 6.13 Scanning ion micrograph, showing a micro-cantilever with tungsten electrodes deposited along its bottom half on either side

Actuation of the fabricated micro-cantilever through the converse piezoelectric effect, was attempted by application of a range of different oscillatory electric fields across the width of the cantilever (along the *x*-crystallographic direction), using the deposited electrodes. The extremely small displacement (along the crystallographic *z*-direction) resulting from the piezoelectric activation mechanism could be detected by measuring the relative fringe shifts in a Michelson interferometer, having the cantilever structure in one of its arms. A collimated beam from a HeNe laser split into two using a 50/50 beam splitter, and then reflected off a plane mirror and the top of the actuated cantilever within the two arms of the interferometer, would form an interference pattern on a screen.

However the suggested converse piezoelectric actuation approach, with electrodes deposited along the bottom half of the cantilevers to facilitate electric field induced expansion or contraction, consequently simulating a bimorph, was unsuccessful because of the supposedly opposite domain polarities of regions with and without electrodes of the micro-cantilevers. The scanning electron micrograph in figure 6.14, showing an image of a back-etched cantilever, with wing-like profile resulting from different etch-rates (and hence different polarity domains) for the wing-like sides and the central region of the cantilever, conclusively explains this presumption. The central region as seen in the figure that seems to etch at a much faster rate as compared to the sides suggests the existence of different ferroelectric domain polarities between within the structure. The electric field applied using metal electrodes, defined along the bottom of the cantilevers, to these regions with oppositely orientated domains is effectively nullified consequently producing no net deflection of the cantilever structure.

Future work involves exploring feasible electrode geometries and electrode positions on the cantilever structure for producing the bending effect through the suggested piezoelectric actuation mechanism. Fabricating cantilevers with their longest dimension aligned along the crystallographic *x*-direction, may possibly avoid the formation of the wing-shaped structure that results from the wet-etching step. However electric field poling for fabricating such structures with required uniformity would be an added challenge to the fabrication route.

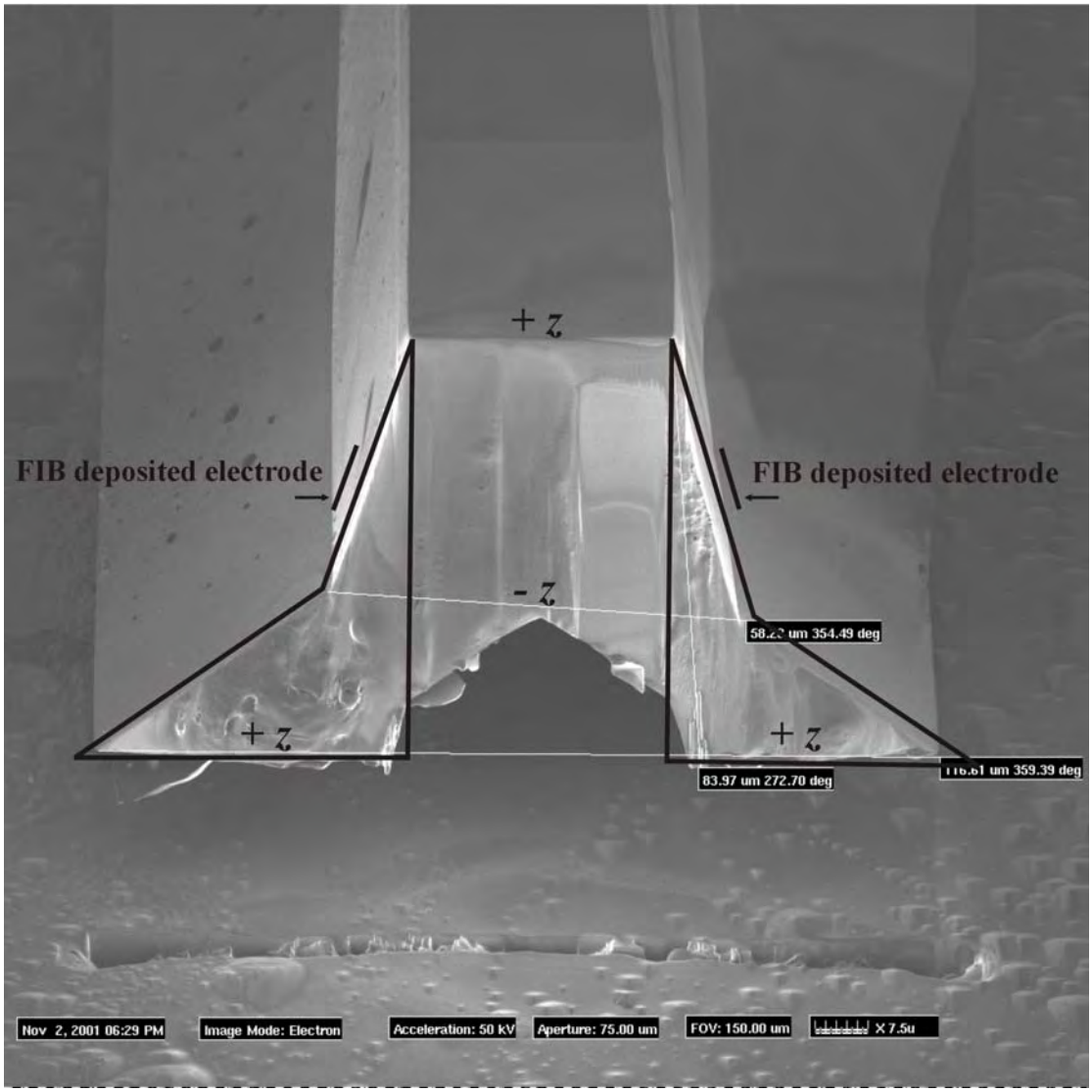

Figure 6.14 Scanning ion micrograph showing a back-etched cantilever, with wing-like profile resulting from different etch-rates (and hence different polarity domains) for the wing-like sides and the central region of the cantilever.

6.3 Calculation of the strain tensor coefficients

As discussed in chapter 2, lithium niobate is piezoelectric and like other piezoelectric solids exhibits an induced polarisation '**P**', with an applied stress 'σ '; with the relationship between them and the third-rank piezoelectric tensor '*d*' mathematically expressed in tensorial form by equation 2.3.

The application of Neumann's principle, which is more convenient to apply to the original piezoelectric tensor rather than the reduced subscript notation, followed by the use of the reduced subscript notation yields the following form.

$$d_{ijk} = \begin{bmatrix} 0 & 0 & 0 & 0 & d_{15} & -2d_{22} \\ -d_{22} & d_{22} & 0 & d_{15} & 0 & 0 \\ d_{31} & d_{31} & d_{33} & 0 & 0 & 0 \end{bmatrix}$$

where $d_{15} = d_{24}$, $d_{22} = -d_{21} = -d_{16}/2$ and $d_{31} = d_{32}$

Hence the piezoelectric effect in lithium niobate can be described by four independent coefficients only, d_{15}, d_{22}, d_{31} and d_{33}.

Measured values of these quantities, acquired from different references, and reported by (Weis'85), are presented in the table 1 given below:

Table 1

d_{15} C/N	d_{22} C/N	d_{31} C/N	d_{33} C/N
6.92×10^{-11}	2.08×10^{-11}	$- 0.085 \times 10^{-11}$	0.6×10^{-11}
6.8×10^{-11}	2.1×10^{-11}	$- 0.1 \times 10^{-11}$	0.6×10^{-11}
7.4×10^{-11}	2.1×10^{-11}	$- 0.087 \times 10^{-11}$	1.6×10^{-11}

We however are interested in the converse piezoelectric effect, wherein a solid exhibits a change in shape with an applied electric field, expressed by equation 2.5; relating the second-rank strain tensor *S*, third-rank piezoelectric tensor *d* and the applied electric field ***E***.

We shall now try to deduce the different strain coefficients S_{jk} by substituting different values of *ijk* in equation 2.5 relating the second rank strain tensor to the applied electric field and the third rank piezoelectric tensor.

For *j* = 1, *k* = 1 and *i* = 1-3, we get

$$S_{11} = d_{111}E_1 + d_{211}E_2 + d_{311}E_3 = d_{11}E_1 + d_{21}E_2 + d_{31}E_3 \qquad \textbf{6.1}$$

For *j* = 1, *k* = 2 and *i* = 1-3, we get

$$S_{12} = d_{112}E_1 + d_{212}E_2 + d_{312}E_3 = 1/2 \times \left(d_{16}E_1 + d_{26}E_2 + d_{36}E_3\right) \qquad \textbf{6.2}$$

For *j* = 1, *k* = 3 and *i* = 1-3, we get

$$S_{13} = d_{113}E_1 + d_{213}E_2 + d_{313}E_3 = 1/2 \times \left(d_{15}E_1 + d_{25}E_2 + d_{35}E_3\right) \qquad \textbf{6.3}$$

For j = 2, k = 1 and i = 1-3, i = 1-3 we get

$$S_{21} = d_{121}E_1 + d_{221}E_2 + d_{321}E_3 = 1/2 \times \left(d_{16}E_1 + d_{26}E_2 + d_{36}E_3\right) \quad \textbf{6.4}$$

For j = 2, k = 2 and i = 1-3, we get

$$S_{22} = d_{122}E_1 + d_{222}E_2 + d_{322}E_3 = d_{12}E_1 + d_{22}E_2 + d_{32}E_3 \quad \textbf{6.5}$$

For j = 2, k = 3 and i = 1-3, we get

$$S_{23} = d_{123}E_1 + d_{223}E_2 + d_{323}E_3 = 1/2 \times \left(d_{14}E_1 + d_{24}E_2 + d_{34}E_3\right) \quad \textbf{6.6}$$

For j = 3, k = 1 and i = 1-3, we get

$$S_{31} = d_{131}E_1 + d_{231}E_2 + d_{331}E_1 = 1/2 \times \left(d_{15}E_1 + d_{25}E_2 + d_{35}E_3\right) \quad \textbf{6.7}$$

For j = 3, k = 2 and i = 1-3, we get

$$S_{32} = d_{132}E_1 + d_{232}E_2 + d_{332}E_3 = 1/2 \times \left(d_{14}E_1 + d_{24}E_2 + d_{34}E_3\right) \quad \textbf{6.8}$$

For j = 3, k = 3 and i = 1-3, we get

$$S_{33} = d_{133}E_1 + d_{233}E_2 + d_{333}E_3 = d_{13}E_1 + d_{23}E_2 + d_{33}E_3 \quad \textbf{6.9}$$

Using the above calculated values, we can rewrite the second rank strain tensor $S_{jk} = \begin{pmatrix} S_{11} & S_{12} & S_{13} \\ S_{21} & S_{22} & S_{23} \\ S_{31} & S_{32} & S_{33} \end{pmatrix}$ as follows

$$\begin{pmatrix} d_{11}E_1 + d_{21}E_2 + d_{31}E_3 & 1/2 \times \left(d_{16}E_1 + d_{26}E_2 + d_{36}E_3\right) & 1/2 \times \left(d_{15}E_1 + d_{25}E_2 + d_{35}E_3\right) \\ 1/2 \times \left(d_{16}E_1 + d_{26}E_2 + d_{36}E_3\right) & d_{12}E_1 + d_{22}E_2 + d_{32}E_3 & 1/2 \times \left(d_{14}E_1 + d_{24}E_2 + d_{34}E_3\right) \\ 1/2 \times \left(d_{15}E_1 + d_{25}E_2 + d_{35}E_3\right) & 1/2 \times \left(d_{14}E_1 + d_{24}E_2 + d_{34}E_3\right) & d_{13}E_1 + d_{23}E_2 + d_{33}E_3 \end{pmatrix}$$

It should be taken into account that as a large number of components of the piezoelectric tensor, except for $d_{15} = d_{24}$, $d_{22} = -d_{21} = -d_{16}/2$, $d_{31} = d_{32}$ and d_{33} are zero, the strain tensor can be rewritten as:

$$\begin{pmatrix} -d_{22}E_2 + d_{31}E_3 & -d_{22}E_1 & d_{15}E_1/2 \\ -d_{22}E_1 & d_{22}E_2 + d_{31}E_3 & d_{15}E_2/2 \\ d_{15}E_1/2 & d_{15}E_2/2 & d_{33}E_3 \end{pmatrix}$$

S_{11}, S_{22} and S_{33} are the extensions parallel to x, y and z respectively, and S_{12} is the rotation about z of a line element parallel to y.

On substituting the values of the different coefficients of the piezoelectric tensor, $\tilde{d}$, from the table stated earlier, together with the appropriate component of the electric field vector E, into the above strain tensor, we can obtain the relative strain coefficients.

Using the below mentioned tensor equation:

$$\Delta l_k = S_{jk} l_k \qquad \textbf{6.10}$$

or its equivalent matrix relation stated below:

$$\begin{bmatrix} \Delta x \\ \Delta y \\ \Delta z \end{bmatrix} = \begin{bmatrix} -d_{22}E_2 + d_{31}E_3 & -d_{22}E_1 & d_{15}E_1/2 \\ -d_{22}E_1 & d_{22}E_2 + d_{31}E_3 & d_{15}E_2/2 \\ d_{15}E_1/2 & d_{15}E_2/2 & d_{33}E_3 \end{bmatrix} \begin{bmatrix} x \\ y \\ z \end{bmatrix} \qquad \textbf{6.11}$$

we arrive at the following

$$\Delta x = (-d_{22}E_2 + d_{31}E_3)x + (-d_{22}E_1)y + (d_{15}E_1/2)z \qquad \textbf{6.12}$$

$$\Delta y = (-d_{22}E_1)x + (d_{22}E_2 + d_{31}E_3)y + (d_{15}E_2/2)z \qquad \textbf{6.13}$$

$$\Delta z = (d_{15}E_1/2)x + (d_{15}E_2/2)y + (d_{33}E_3)z \qquad \textbf{6.14}$$

from which we can deduce the strains along any particular directions.

In the above stated equation, $\Delta x, \Delta y$ and Δz are the changes in the x, y, z directions respectively. A positive value of Δ indicates an increase along that direction as a result of a tensile strain and a negative value of Δ indicates a decrease in that direction because of a compressive strain along that direction.

Using the above derived equations for the $\Delta's$, we can calculate the changes along the different dimensions of a cantilever, which we have structured and intend to actuate. We can also calculate the displacement of the free end of the cantilever, when subjected to an electric field.

The cantilevers that we have structured have an almost rectangular cross-section, with their length along the y-direction, breadth along the x-direction and thickness along the z direction within the crystal. To employ the derived formulae, let us consider an illustrative example of a cantilever shown in figure 6.15, having a length of 1mm/2mm/3mm and a width and thickness of 20μm, subjected to an applied voltage of 26 volts, across its width, i.e. along the x direction (which incidentally is also the only accessible direction as far as applying an electric field to the structured

cantilevers is concerned). As one end of the fabricated cantilevers, having their lengths along the y-direction is bound to a rigid support, the electrodes and hence the applied electric field cannot be applied along the y-direction. Moreover as the bottom of the structured cantilevers is not accessible also, the electrodes and hence the necessary electric field cannot be applied along the z-direction too.

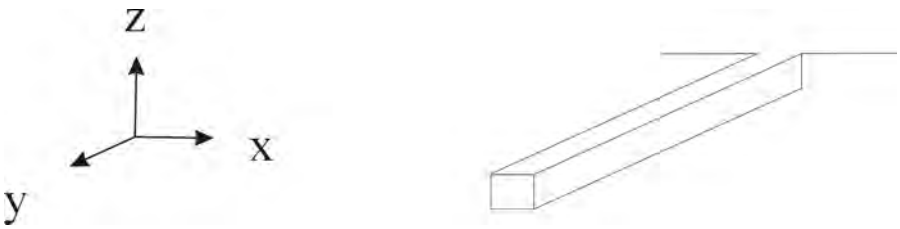

Figure 6.15 Schematic of a cantilever with its longest dimension along the crystallographic y-direction.

Table 2, shows the change in different dimensions of the cantilevers of lengths 1,2 and 3mm, subjected to a constant electric field of 26V over 20μm (=1.3 x 10^6 V/m)

Table 2

For cantilever of length	Δx / m	Δy / m	Δz / m
1 mm	$- 27.00 \times 10^{-9}$	$- 0.54 \times 10^{-9}$	0.89×10^{-9}
2 mm	$- 54.04 \times 10^{-9}$	$- 0.54 \times 10^{-9}$	0.89×10^{-9}
3 mm	$- 81.08 \times 10^{-9}$	$- 0.54 \times 10^{-9}$	0.89×10^{-9}

As shown in figure 6.16, for the other alternative structuring option with cantilevers, having their lengths along the x-direction, breadths along the y-direction and thickness, as in the previous case along the z-direction, application of an electric of similar magnitude along the y-direction, the strain equations yield the set of results summarised in table 3.

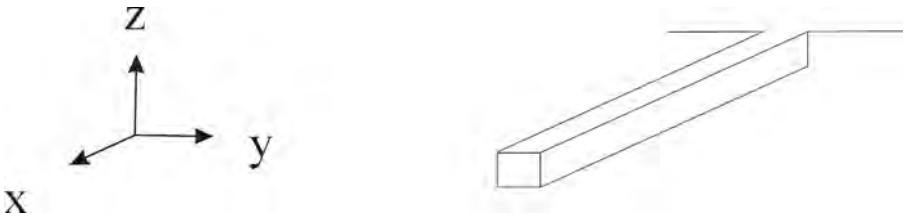

Figure 6.16 Schematic of a cantilever with its longest dimension along the crystallographic *x*-direction.

Table 3

For cantilever of length	Δx / m	Δy / m	Δz / m
1 mm	-27.04×10^{-9}	1.44×10^{-9}	0.89×10^{-9}
2 mm	-54.08×10^{-9}	1.44×10^{-9}	0.89×10^{-9}
3 mm	-81.12×10^{-9}	1.44×10^{-9}	0.89×10^{-9}

Using the above-obtained results, we can evaluate the deflection of the cantilever in the vertical direction, which is the z-direction for both the cases we have considered. We intend to deflect the cantilevers by applying an electric field only along the top (or bottom half) of its thickness, so as to induce a compressive or tensile strain in the corresponding region; in effect simulating the behaviour of a bimetallic strip.

Let us consider the case of a cantilever having a length of 2mm and a breadth and thickness of 20μm, with its length along the x-direction, subjected to an electric field of 26 volts across its breadth, with the help of electrodes along the top half of its thickness. As calculated earlier, the applied field will induce a compressive strain in that top region, thereby reducing its length by 54nm. Using figure 6.17 showing a deflected cantilever, and some geometric principles, the deflection in the vertical direction can be calculated as follows.

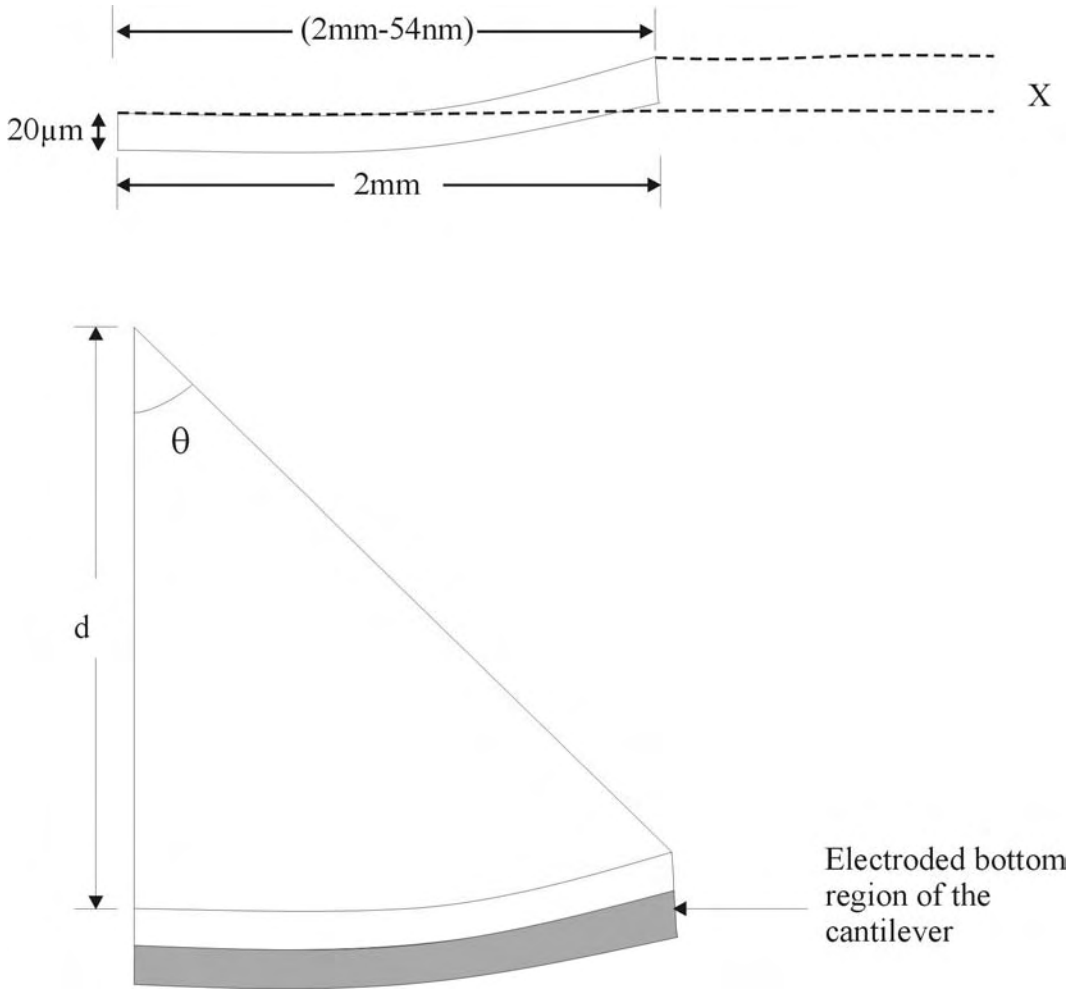

Figure 6.17 Schematic of a deflected cantilever of length 2mm, width 20µm and thickness of 20µm on application of an electric field.

From the above figure θ can be expressed as:

$$\theta = \frac{\left(2\times10^{-3} - 54\times10^{-9}\right)}{d} = \frac{\left(2\times10^{-3}\right)}{\left(d + 20\times10^{-6}\right)} \qquad \textbf{6.15}$$

$$d\left(2\times10^{-3}\right) = d\left(2\times10^{-3} - 54\times10^{-9}\right) + \left(2\times10^{-3} - 54\times10^{-9}\right)\left(20\times10^{-6}\right)$$

on solving the above equality we get

$d = 0.74m$

Using the above obtained value of d, we can obtain θ and hence x as follows:

$$\theta = \tan^{-1}\left(\frac{2\times10^{-3}}{0.74}\right) = 0.15^{\circ} \Rightarrow x = 2.7\mu m \qquad \textbf{6.16}$$

The above derived deflection calculation however is a rough first-order estimate which ignores the mechanical stiffness of the cantilever and also the counter-acting converse-piezoelectric field, resulting from the strain induced in the un-electroded region on actual bending of the cantilever beam.

6.4 Calculations for the frequency of vibration of the structured cantilevers

Using the Rayleigh-Ritz method, which usually yields the frequency of vibration of the fundamental mode with a high accuracy (Bao'01), the frequency of vibration of the structured cantilevers, can be evaluated as follows.

The angular frequency of vibration, 'ω' of a cantilever beam can be deduced by the following equation:

$$\omega = 3.53\sqrt{EI/ML^3} \qquad \textbf{6.17}$$

where E is the Young's modulus or the stiffness of the material, I is the second moment of the cantilever beam, M is the mass of the beam and L is its length. If b is the width and d the thickness of the cantilever beam, the second moment for a cantilever beam with a rectangular cross-section can be expressed as:

$$I = \frac{bd^3}{12} \qquad \textbf{6.18}$$

If ρ is the density of the material from which the structure is made then the mass of the cantilever can be expressed as:

$$M = bdL\rho \qquad \textbf{6.19}$$

On substituting this value together with that of I, the equation for the vibrational angular frequency can be rewritten as:

$$\omega = 1.019\frac{d}{L^2}\sqrt{\frac{E}{\rho}} \qquad \textbf{6.20}$$

Frequencies of vibration of the fundamental mode, calculated using the above relation, for cantilevers with dimensions similar to those we have been able to fabricate, are shown in table 4. The source of the stiffness constants used was EMIS'89.

Table 4

The calculated angular frequencies for cantilevers with b = 50μm, d = 50μm and differing lengths

For stiffness $\times 10^{11}$ C/N	Angular frequency for length L = 1mm / Hz	Angular frequency for length L = 2mm / Hz	Angular frequency for length L = 5mm / Hz
At constant polarisation, for CP_{33} = 2.52	3.75 x 10^5	0.93 x 10^5	0.15 x 10^5
At constant polarisation, for CP_{44} = 0.94	2.29 x 10^5	0.57 x 10^5	0.09 x 10^5
At constant field, for CE_{33} = 2.45	3.70 x 10^5	0.92 x 10^5	0.14 x 10^5
At constant field, for CE_{13} = 0.75	2.04x 10^5	0.51 x 10^5	0.08 x 10^5
At constant field, for CE_{14} = 0.09	0.70 x 10^5	0.17 x 10^5	0.02 x 10^5

The calculated angular frequencies for cantilevers with b = 50μm, d = 40μm and differing lengths

For stiffness $\times 10^{11}$C/N	Angular frequency for length L = 1mm / Hz	Angular frequency for length L = 2mm / Hz	Angular frequency for length L = 5mm / Hz
At constant polarisation, for CP_{33} = 2.52	3.00 x 10^5	0.75 x 10^5	0.12 x 10^5
At constant polarisation, for CP_{44} = 0.94	1.83 x 10^5	0.45 x 10^5	0.07 x 10^5
At constant field, for CE_{33} = 2.45	2.96 x 10^5	0.74 x 10^5	0.11 x 10^5
At constant field, for CE_{13} = 0.75	1.63 x 10^5	0.40 x 10^5	0.06 x 10^5
At constant field, for CE_{14} = 0.09	0.56 x 10^5	0.14 x 10^5	0.02 x 10^5

The calculated angular frequencies however could not be experimentally verified as actuation of the structured micro-cantilevers by the discussed mechanism was not achievable.

6.5 Summary

A novel route, sequentially employing different surface and bulk micro-machining techniques such as photolithographic patterning, electric field poling, direct bonding and domain-sensitive differential wet etching, was demonstrated for the fabrication of freestanding microstructures in ferroelectric single crystal lithium niobate. This technique integrating conventional IC fabrication processes and ferroelectric domain engineering techniques, was employed in the fabrication of the first ever micro-cantilever with lateral dimensions of 10-50μm and lengths > 5mm in the *x*, *y* and *z* crystallographic orientations respectively. The Focussed-ion-beam deposition technique was adopted for directly written tungsten metal-tracks, serving as electrodes for piezoelectric actuation of the micro-cantilevers. Actuation through the converse piezoelectric effect was attempted by application of an electric field. Tensorial calculation to deduce the induced strain or change in different structural dimensions of the micro-cantilevers was presented. Simple mathematical calculations to deduce the displacement and angular frequency of vibration of the fabricated micro-cantilever structure were also presented. The suggested converse piezoelectric actuation approach, using electrodes deposited along the bottom half of the cantilevers to facilitate electric field induced expansion or contraction, consequently producing a bending moment as in a bimorph, was unsuccessful because of the supposedly opposite domain polarities of regions with and without electrodes of the micro-cantilevers, and also because of a counter-acting electric field generated via the converse-piezoelectric effect in the electrode-free region strained by a bending motion of the cantilever. The strain induced electric field together with the mechanical stiffness of the cantilevers could have acted to affect or indeed cancel or reduce the actual displacement of the cantilever effectively making the motion undetectable.

Future work involves exploring feasible electrode geometries and electrode positions on the cantilever structure for producing the bending effect through the suggested piezoelectric actuation mechanism. Fabricating cantilevers with their longest dimension aligned along the crystallographic *x*-direction, may possibly avoid the formation of the wing-shaped structure that results from the wet-etching step. However electric field poling for fabricating such structures with required uniformity would be an added challenge to the fabrication route.

6.6 References

Akamino S, Kuwano H, Yamada H, *Appl.Phys.Lett.* **68(5)**, 579, (1996).

Bao MH, Handbook of Sensors and Actuators, Vol 6, Micro Mechanical Transducers Pressure Sensors, Accelerometers and Gyroscopes, **2nd ed**. (2001)

Barry I.E, Ross G.W, Smith P.G.R, Eason R.W, *Appl.Phys.Lett*, **74(10)**, 1487, (1999).

Barry I.E, Ross G.W, Smith P.G.R, Eason R.W, Cook G, *Mater.Lett*. **37(4-5)**, 246, (1998).

Berger R, Gerber Ch, Gimzewski J.K, Meyer E, Guntherodt H..J, *Appl.Phys.Lett*. **69(1)**, 40, (1996).

Bermudez V, Caccavale F, Sada C et al, *J.Cryst.Growth*, **191**, 589, (1998).

Brown PT, Eason RW, Ross GW, Pogosyan AR, *Opt.Commun*, **163**, 310, (1999).

Burr K.C, Tang C.L, Arbore M.A, Fejer M.M, *Appl.Phys.Lett*. **70(25)**, 3341, (1997).

Byer R.L, *J.NonlinearOpt.Phys.Mater*. **6**, 549, (1997).

Chao S, Davis W, Tuschel DD et al, *Appl.Phys.Lett*, **67**, 1066, (1995).

Chen G.Y, Thundat T, Wachter E.A, Warmack R.J, *J.Appl.Phys*. **77(8)**, 3618, (1995).

Cheng R.S, Chen W.L, Wang W.S, *IEEE Photon.Technol.Lett*. **7(11)**, 1282, (1995).

Cotton FA and Wilkinson G, *Advanced Inorganic Chemistry*, Wiley, New York, **5th ed**. p.104, (1988).

Eason R.W, Barry I.E, Ross G.W, Smith P.G.R, *Electron.Lett*. **35(4)**, 328, (1999)

Eckert R, Freyland J.M, Gersen H, Heinzelmann H, Schurmann G, Noell W, Staufer U, de Rooij NF, *Appl.Phys.Lett.* **77(23)**, 3695, (2000).

EMIS Data Review Series **5**, *Properties of Lithium Niobate, INSPEC*, London *1989.*

Feisst A, Koidl P, *Appl.Phys.Lett*. **47(11)**, 1125, (1985).

Feng D, Ming N.B, Hong J.F, *Appl.Phys.Lett*. **37**, 607, (1980).

Glass A.M, Von der Linde D, Negran TJ, *Appl.Phys.Lett*. **25**, 233, (1974).

Grey F, Hermansson K, *Appl.Phys.Lett*. **71(23)**, 3400, (1997).

Haisma J, Spierings G.A.C.M et al, *Appl.Opt*, **33(7)**, 1154, (1994).

Heisig S, Rudow O, Oesterschulze G, *Appl.Phys.Lett.* **77(8)**, 1071, (2000).

Himi H, Matsui H et al, *Jpn.J.Appl.Phys.Part-I*, **33**, 6, (1994).

Holstein WL, *J.Cryst.Growth*, **171**,477, (1997).

Ichikawa T, Kagami M, Ito H, *Opt.Lett*, **23(14)**. 1138, (1998).

Knotter DM, *J.Am.Chem.Soc*, **122**, 4345, (2000).

Kock M, Evans A.G.R, Brunschweiler A, *J.Micromech.Microeng*. **7**, 221, (1997).

Kulevitch P, Lee AP, Ramsey P.B, Trevino J.C, Hamilton J, Northrup M.A, *J.Microelectromech.Syst*. **5(4)**, 270, (1996)

Lawrence M, Integrated Optics

Lee C, Itoh T, Suga T, *Sensors Actuators A*, **72**, 179, (1999).

Lee DN, Ono DN, Gsashi M, *Sensors Actuators A*, **83**, 11, (2000).

Lefort L, Puech K, Butterworth S.D, Ross G.W, Smith P.G.R, Hanna D.C, Jundt D.H, *Opt.Commun*.**152(1-3)**, 55, (1998).

Ljungberg K, Soderbarg A, Backlund Y, *Appl.Phys.Lett*. **62(12)**, 1362, (1993).

Lu Y.Q, Xiao M, Salamo G.J, *Appl.Phys.Lett*. **78(6),** 1035, (2001).

Lutwyche M.I, Wada Y, *Sensors Actuators A*, **48**, 127, (1995).

Mailis S, Riziotis C, Wellington I.T, Smith P.G.R, Gawith C.B.E, Eason R.W, Accepted for publication in *Opt.Lett*'03.

Mailis S, Ross G.W, Reekie L, Abernethy J.A, Eason R.W, *Electron.Lett*. **36(21)**, 1801, (2000).

Majumdar A, OdemP.I, CarrejoT.P, Nagahara L.A, Graham J.J, Alexander J, *Appl.Phys.Lett*. **61(19)**, 2293, (1992).

Manalis S.R, Minne S.C, Quate C.F, Yaralioglu G.G, Atalar A, *Appl.Phys.Lett*. **70(24)**, 3311, (1997).

Melngailis J, *J.Vac.Sci.Technol B*, **5**, 469,1987

Ming N.B, Hong J.F, Feng D, *J.Mater.Sci*. **17**, 1663, (1982).

Minne S.C, Soh H.T, Flueckiger P, Quate C.F, *Appl.Phys.Lett*. **66(6)**, 703, (1995).

Missey M.J, Dominic V, Myers L.E, Eckardt R.C, *Opt.Lett*, **23(9)**, 664, (1998).

Mitane K, Gosele U, *J.Electron.Mater*. **21**, 669, (1992).

Motamedi M.E, Park S, Wang A.H, Dadkhah M.S, Andrews A.P, Marcy H.O, Khoshnevisan M, Chiou A.E, Huhn R.J, Sell C.F, Smits J.G, *Opt.Eng*, **36(5)**, 1346, (1997).

Nassau K, Levenstein H.J, Loiacono G.M, *Appl.Phys.Lett*, **6(11)**, 228, (1965).

Nassau K, Levenstein HJ, Loiacono GM, *J.Phy.Chem.Solids*, **27**, 983, (1966).

Nizeki N, Yamada T, Toyoda H, *Jpn.J.Appl.Phys*, **6**,318, (1967).

Oliver A.A, *Acoustic Surface Waves, Topics in Applied Physics*, Springer, NY, 1978.

Pelrine R, Kornbluh R.D, Joseph J, *Sensors Actuators A*, **64**, 77, (1998).

Petersen K.E, *IBM J.Res.Dev*, **23**, 376, 1979.

Prewett P.D, *Vacuum*, **44**, 345, 1993

Prokhorov A.M, Kuzminov Yu.S, *Physics and Chemistry of Crystalline Lithium Niobate*, Adam Hilger, Bristol, 1990.

Qi R, Thomson D.J, Bridge G.E, *Microelectron.Relia*. **40(6)**, 997, (2000).

Quandt E, Seeman K, *Sensors Actuators A*, **50**, 105, (1995).

Ross G.W, Pollnau M, Smith P.G.R, Clarkson W.A, Britton P.E, Hanna D.C, *Opt.Lett*. **23(3)**, 171, (1998).

Sasaki M, Tanka K, Hane K, *Jpn.J.Appl.Phys*. **39(12B)**, 7150, (2000).

Snow E.S, Campbell M.P, *Appl.Phys.Lett*. **64(15)**, 1932, (1994).

Spierings G.A.C.M, Haisma J, Michelsen T.M, *Phillips.J.Res*, **49**, 47, (1995).

Tong Q.Y, Cha G, Gafiteanu R, Gosele U, *J.Microelectromech.Syst*. **3**, 29, (1994)

Thundat T, Chen G.Y, Warmack R.J, *Anal.Chem*, **67**, 519, 1995

Wachter E.A, Thundat T, Oden P.I, Warmack R.J, Datskos P.G, Sharp S.L, *Rev.Sci.Instrum*, **67**, 3434, 1996

Weis R.S, Gaylord T.K, *Appl.Phys.A*, **37**, 191, (1985).

Wolter O, Bayer T, Greschner J, *J.Vac.Sci.Technol B*, **9(2)**, 1353, (1991).

Yamada M, Nada N, Saitoh M, Watanabe K, *Appl.Phys.Lett*. **62(5)**, 435, (1993).

Yamada M, Saitoh M, Ooki H, *Appl.Phys.Lett*. **69(24)**, 3659, (1996).

Young R.J, *Vacuum*, **44**, 353, 1993

Young R.J, Cleaver J.R, Ahmed H, *J.Vac.Sci.Technol. B*, **11**, 234, 1993.

Zhang Y.W, Zhang Y.X, Marcus R.B, *J.Microelectromech.Syst* **8(1)**, 43, (1999).

Zhou S, Sun X.Q, Carr W.N, *J.Micromech.Microeng*. **9**, 45, (1999).

Chapter 7
Conclusions and Further work

7.1 Conclusions and future work for chapter 4

Domain visualisation techniques used to assess the quality of domain inversion were discussed in brief followed by a discussion at length of the frequently used visualisation approach of wet or chemical etching in context of the potential application of this technique for micro-structuring lithium niobate.

A parametric study was presented of the etch rates and the etch quality as a function of the traditionally used etchant mixture of 'HF:HNO_3' in the specific ratio of 1:2' to ascertain if indeed it was the ideal choice for achieving the optimal differential etch rates and etch quality, and also investigate a recently observed possible second differential etch behaviour was presented. It was immediately apparent from the experimental investigations that the widely used ratio was optimum neither in the etch depths achieved nor in the smoothness achieved for the etched –z faces, moreover it can be conclusively seen that the etch rate achieved with that ratio is approximately half of that with the pure HF solution. The best results for the depth and the smoothness were observed for the pure HF solution at the temperature of 60^0C. The hugely improved degree of smoothness associated with the pure HF solution could be exploited for realising deep three-dimensional structures on lithium niobate.

The set of data collected from the etching studies with different HF/HNO_3 and HF/H_2O ratios are suggestive of a second differential etch rate between the newly poled material and the virgin material. The behaviour is well quantified by the contrast ratio parameter and could be of potential use in structuring application where precise control of the etch rates and back etching is desirable.

A proposed reaction formulation explaining the observed differential etching mechanism between opposing crystallographic z-faces was also discussed. The suggested mechanism for the etch rate in aqueous HF involves an initial dehydroxylation of the negatively charged surface by proton attack followed by an electrostatically enhanced reaction of the subsequent positively charged surface with H_2^- anions, with the rapid increase in the rate near the 48% composition attributed to the reduction in free water concentration. However the linear dependence in the etch rate with the HF concentration for the aqueous HF/HNO_3 solutions is a result of the

attack of the nitrate covered positive surface by the abundant neutral species H_2F_2, with an initial protonation considered essential in both cases, and much slower on the positively charged face.

Systematic experimental trials were conducted to gather information about the effect of a time delayed internal field relaxation, on the mechanism of differential etching; the etch rates and the etch quality, as this could prove be an essential tool in aiding the undertaken micro-structuring experiments. The experimental data for the HF/HNO_3 ratio at an elevated temperature and that for the pure HF solution at room temperature revealed a latent etch mechanism in lithium niobate, also evidenced by Raman studies conducted within the research group.

The set of obtained data do not indicate any conclusive trend in the etch rates with time, which was thought to relax the internal field within the poled crystal.

Preliminary experiments with the light-induced-frustrated-etching technique were presented demonstrating its applicability for structuring un-doped congruent z-cut lithium niobate, resulting in the formation of μm scale surface relief structures. A modification in the chemical etching behaviour of undoped congruent z-cut lithium niobate single crystals was observed on pre-illumination of the –z face of the crystal with sub-picosecond UV laser radiation at 248nm from an excimer laser for energy fluences slightly below the ablation threshold of lithium niobate. A systematic study of the effect of the incident energy fluence and total exposure on the etch frustration phenomenon revealed with 20%-80% slower etch rates for the illuminated areas varying with the illuminating energy fluence and exposure were observed. Different saturation levels and hence different suppression levels were also observed for different illuminating energy fluences. The phenomenological explanation of the effect involves laser induced mobile charge carriers which interfere with the electrochemistry of lithium niobate surface effectively reducing the chemical etch rate.

The proposed reaction formulation explaining the observed differential etching mechanism, systematic experimental trial conducted to gather information about the effect of a time delayed internal field relaxation on the mechanism of differential etching and preliminary experiments with the light-induced-frustrated-etching technique could prove be an essential tool in aiding future attempts at micro-structuring lithium niobate.

7.2 Conclusions and future work for chapter 5

A brief theoretical treatment of the concept of quasi-phase-matching for non-linear interactions using periodically domain-inverted structures in lithium niobate was presented. The technique of electric field induced periodic poling was briefly discussed and an innovative technique referred to as, 'surface periodic poling' of congruent lithium niobate crystal, based on the conventional electric-field poling, but involving an intentional over-poling step that inverts the entire crystal apart from the thin surface region below the patterned face, was proposed.

Some experimental results achieved using this simple single-step technique to structure one and two-dimensional periodic structures in lithium niobate were shown. The surface poled structures showed good uniformity with depths extending to values of the order of few μm, thereby removing the high aspect ratio instability problems associated with the conventional bulk poling technique. The technique was implemented to achieve domains periodicities of ~1μm, and its applicability was further verified to pole first-order grating structures in predefined waveguide geometries for quasi-phase-matched waveguide interactions in lithium niobate, without any unnecessary additional processing steps.

Quasi-phase-matched harmonic generation at the fundamental wavelength of 1.064 μm, by means of the first-order (G_{10}) reciprocal lattice vector, from a surface hexagonally poled planar annealed proton exchanged waveguide, with domain period of 6.7μm, was demonstrated. The initial quasi-phase matching results from the two-dimensional hexagonal surface-poled waveguide structure shows the potential of this technique.

First-order quasi-phase-matched blue light generation with reasonable efficiencies at 413.17nm, with domain periods of 2.47μm; from a surface poled Ti-indiffused channel waveguide was demonstrated.

The associated undesirable effect of lateral spreading of surface domains into the un-patterned area, leading to periodic structures with a non-ideal mark-to-space ratios and reduced non-linear interaction efficiencies was investigated. Attempts to optimise the surface-poling conditions for achieving periodic structures with ideal mark-to-space ratios of unity, were examined by varying the corresponding mark-to-space ratios on the mask used to pattern the periodic structure, and the empirical factor used for surface-poling. The initial parametric studies aimed at understanding the

mechanism showed conclusive trends for achieving the periodic structures with ideal mark-to-space ratios.

The suggested further work involves use of the acquired information for achieving surface poled first-order Ti-indiffused waveguide structures, with the ideal 50:50 mark-to-space ratio to demonstrate record non-linear interaction efficiencies.

7.3 Conclusion and future work for chapter 6

An ingenious route, sequentially employing different surface and bulk micro-machining techniques such as photolithographic patterning, electric field poling, direct bonding and domain-sensitive differential wet etching, was demonstrated for the fabrication of freestanding microstructures in ferroelectric single crystal lithium niobate. This technique integrating conventional IC fabrication processes and ferroelectric domain engineering techniques, was employed in the fabrication of the first ever micro-cantilever with lateral dimensions of 10-50μm and lengths > 5mm in the *x*, *y* and *z* crystallographic orientations respectively. Focussed-ion-beam deposition technique was experimented with for directly written tungsten metal-tracks, serving as electrodes for piezoelectric actuation of the micro-cantilevers. Tensorial calculation to deduce the induced strain or change in different structural dimensions of the micro-cantilevers was presented. Simple mathematical calculations to deduce the displacement and frequency of vibration of the fabricated micro-cantilever structure were also presented. The suggested converse piezoelectric actuation approach, using electrodes deposited along the bottom half of the cantilevers to facilitate electric field induced expansion or contraction, consequently producing a bending moment as in a bimorph, was unsuccessful because of the supposedly opposite domain polarities of regions with and without electrodes of the micro-cantilevers.

Future work involves exploring feasible electrode geometries and electrode positions on the cantilever structure for producing the bending effect through the suggested piezoelectric actuation mechanism. Fabricating cantilevers with their longest dimension aligned along the crystallographic *x*-direction, may possibly avoid the formation of the wing-shaped structure that results from the wet-etching step. However electric field poling for fabricating such structures with required uniformity would be an added challenge to the fabrication route.

The actuation and detection of atomic scale deflections with an AFM of the sub-micron sized lithium niobate tips fabricated by us, and shown in figure 7.1 & 7.2, having focussed ion beam defined metal electrodes along opposite crystallographic faces, is to be further examined. The fabrication technique of such sub-microscopic tips by a prolonged wet etching step, has not been focussed on, and needs further investigation.

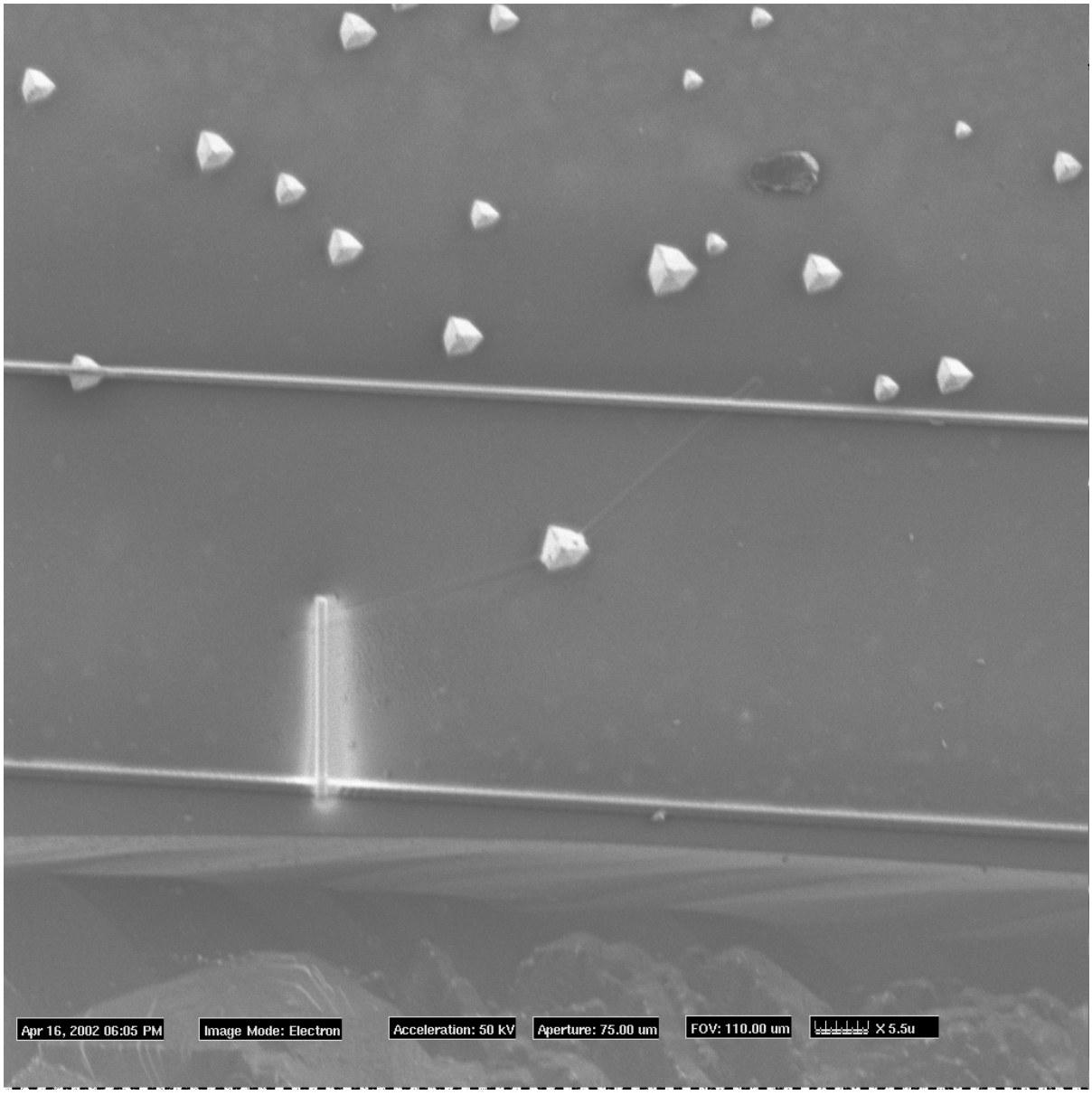

Figure 7.1 SEM image showing two lithium niobate tips interconnected by a tungsten metallic track deposited by the focussed ion beam direct deposition technique.

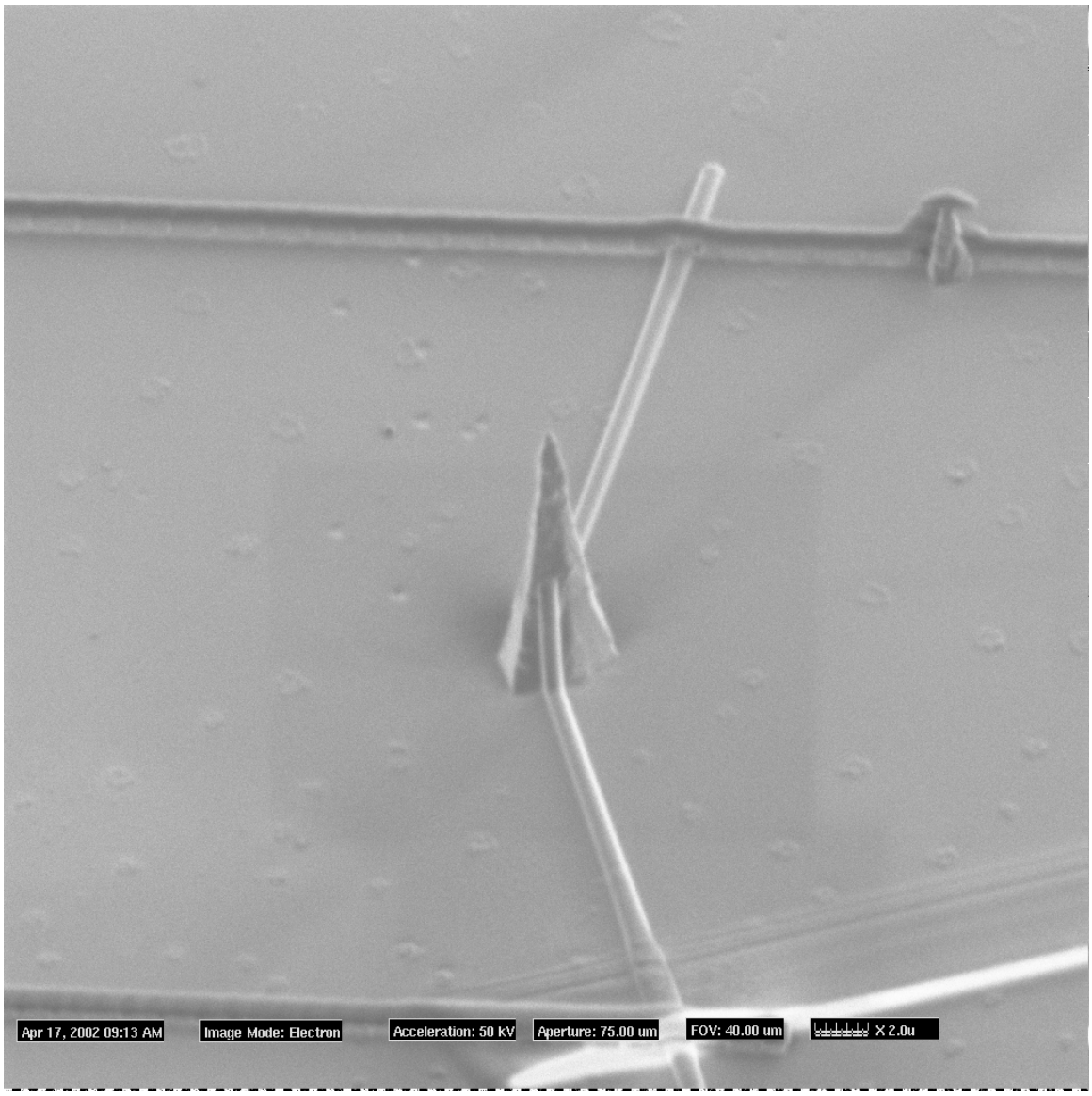

Figure 7.2 SEM image of a single wet-etched lithium niobate tip with metal electrodes deposited on opposite crystallographic faces by the focussed ion beam technique.

Appendix: A

Multiple Solvent Cleaning Procedure

Multiple solvent cleaning, involving the use of an ultrasonic agitator is essentially a prerequisite for the subsequent photolithography stage, and is a preparatory procedure performed in a clean room environment. This sequential solvent treatment is employed to remove organic and inorganic contaminants from the surface of the samples and also for simultaneous removal of the solvents used in the previous step. The samples to be cleaned are placed in a beaker containing the first solvent, which is then placed in the ultrasonic bath and allowed to heat up to the desired temperature of 50^0C while simultaneously agitating the solvent. The beaker with the next solvent to be used is also placed in the bath at the same time warming it up to the same temperature. After a set time the samples are quickly transferred in to the second solvent beaker, and another beaker containing the third solvent to be used is placed in the bath. A second transfer into the third solvent is similarly done after the set period of time.

The detailed treatment in different solvents, with the necessary times, is as stated below:

1. 20 minute immersion in Eco-clear for removal of organic contaminants.
2. 20 minute immersion in acetone for removal of organic residue and Eco-clear.
3. 20 minute immersion in iso-propanol for removal of organic residue and acetone
4. 20 minute immersion in de-ionised water for removal of iso-propanol and remaining contaminants.

The samples are finally blown dry with filtered nitrogen.

Appendix: B

List of Publications

This list includes the publications resulting from the work reported in this thesis.

In Journals

1. A.C.Busacca, C.L.Sones, V.Apostolopoulos, R.W.Eason, S.Mailis
   Surface domain engineering in congruent lithium niobate single crystals: a route to sub-micron periodic poling.
   Applied Physics Letters, 81(26), 4946, 2002
2. C.L.Sones, S.Mailis, W.S.Brocklesby, R.W.Eason, J.R.Owen
   Differential etch rates in z-cut $LiNbO_3$ for variable HF/HNO_3 concentrations
   Journal of Materials Chemistry, **12(2)**, 295, 2002
3. C.Sones, S.Mailis, V.Apostolopoulos, I.E.Barry, C.B.E.Gawith, P.G.R.Smith, R.W.Eason
   Fabrication of piezoelectric micro-cantilevers in domain engineered $LiNbO_3$ single crystals
   Journal of Micromechanics and Microengineering, **12(1)**, 53, 2002
4. S.Mailis, P.T.Brown, C.L.Sones, I.Zergioti, R.W.Eason
   Etch frustration in congruent lithium niobate single crystals induced by femtosecond ultra-violet laser irradiation
   *Applied Physics-A,***74(2)**,135, 2002
5. A.C.Busacca, C.L.Sones, R.W.Eason, S.Mailis
   Surface domain inversion in ferroelectric lithium niobate
   Accepted for publication in *Ferroelectrics.*
6. A.C.Busacca, C.L.Sones, R.W.Eason, S.Mailis, K.Gallo, R.T.Bratfalean, N.G.Broderick
   Surface hexagonally poled lithium niobate waveguides
   Accepted for publication in *Ferroelectrics*
7. J.G.Scott, S.Mailis, C.L.Sones, R.W.Eason
   A Raman study of single crystal congruent lithium niobate following electric field repoling
   Accepted for publication in *Applied Physics-A*

In Conferences

1. C.L.Sones, A.C.Busacca, R.W.Eason, S.Mailis
   Efficient blue light generation from surface periodically poled Ti-in diffused channel waveguides
   CLEO/QELS, 2003, Baltimore 3-5 Jun 2003
2. C.L.Sones, A.C.Busacca, V.Apostolopoulos, R.W.Eason, S.Mailis
   Surface periodic poling of lithium niobate for efficient non-linear optical waveguide applications
   Photonics 2002, Mumbai, 16-18 Dec 2002
3. A.C.Busacca, C.L.Sones, R.W.Eason, S.Mailis
   First order quasi-phase matched blue light generation in surface poled Ti-in diffused lithium niobate waveguide
   Nonlinear Guided Waves and Their Applications, Stresa, Italy, 1-6 Sept 2002 (**Post-deadline Paper**)
4. A.C.Busacca, C.L.Sones, R.W.Eason, S.Mailis, K.Gallo, R.T.Bratfalean, N.G.Broderick
   Surface HeXLN in lithium niobate waveguides
   6th European Conference on Polar Dielectrics (ECAPD6), Aveiro, Portugal, 2-5 Sept 2002
5. A.C.Busacca, C.Sones, R.W.Eason, S.Mailis
   Surface domain inversion in ferroelectric lithium niobate
   6th European Conference on Polar Dielectrics (ECAPD6) Aveiro, Portugal 2-5 Sep 2002